

REGIONAL ATMOSPHERIC DYNAMICS OF WATER ON MARS

by

Cecilia W.S. Leung

---

Copyright © Cecilia W.S. Leung 2020

A Dissertation Submitted to the Faculty of the

DEPARTMENT OF PLANETARY SCIENCES

In Partial Fulfillment of the Requirements

For the Degree of

DOCTOR OF PHILOSOPHY

In the Graduate College

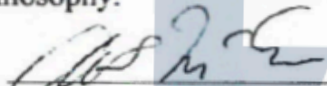
THE UNIVERSITY OF ARIZONA

2020

THE UNIVERSITY OF ARIZONA  
GRADUATE COLLEGE

As members of the Dissertation Committee, we certify that we have read the dissertation prepared by: Cecilia W.S. Leung, titled: The Regional Atmospheric Dynamics of Water on Mars

and recommend that it be accepted as fulfilling the dissertation requirement for the Degree of Doctor of Philosophy.

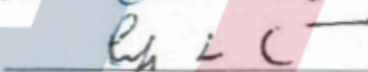
  
\_\_\_\_\_  
[Committee Co-Chair 1 Alfred McEwen] Date: 1/7/20

  
\_\_\_\_\_  
[Committee Co-Chair 2 Scot Rafkin] Date: 1/7/20

  
\_\_\_\_\_  
[Committee Member Melinda Kahre] Date: 1/7/20

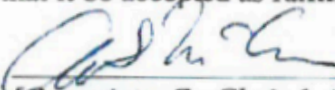
  
\_\_\_\_\_  
[Committee Member Shane Byrne] Date: 1/7/20

  
\_\_\_\_\_  
[Committee Member Roger Yelle] Date: 1/7/20

  
\_\_\_\_\_  
[Committee Member Christopher Castro] Date: 1-7-2020

Final approval and acceptance of this dissertation is contingent upon the candidate's submission of the final copies of the dissertation to the Graduate College.

We hereby certify that we have read this dissertation prepared under our direction and recommend that it be accepted as fulfilling the dissertation requirement.

  
\_\_\_\_\_  
[Committee Co-Chair 1 Alfred McEwen] Date: 1/7/20

Dissertation Committee Co-Chair  
[Department of Planetary Sciences]

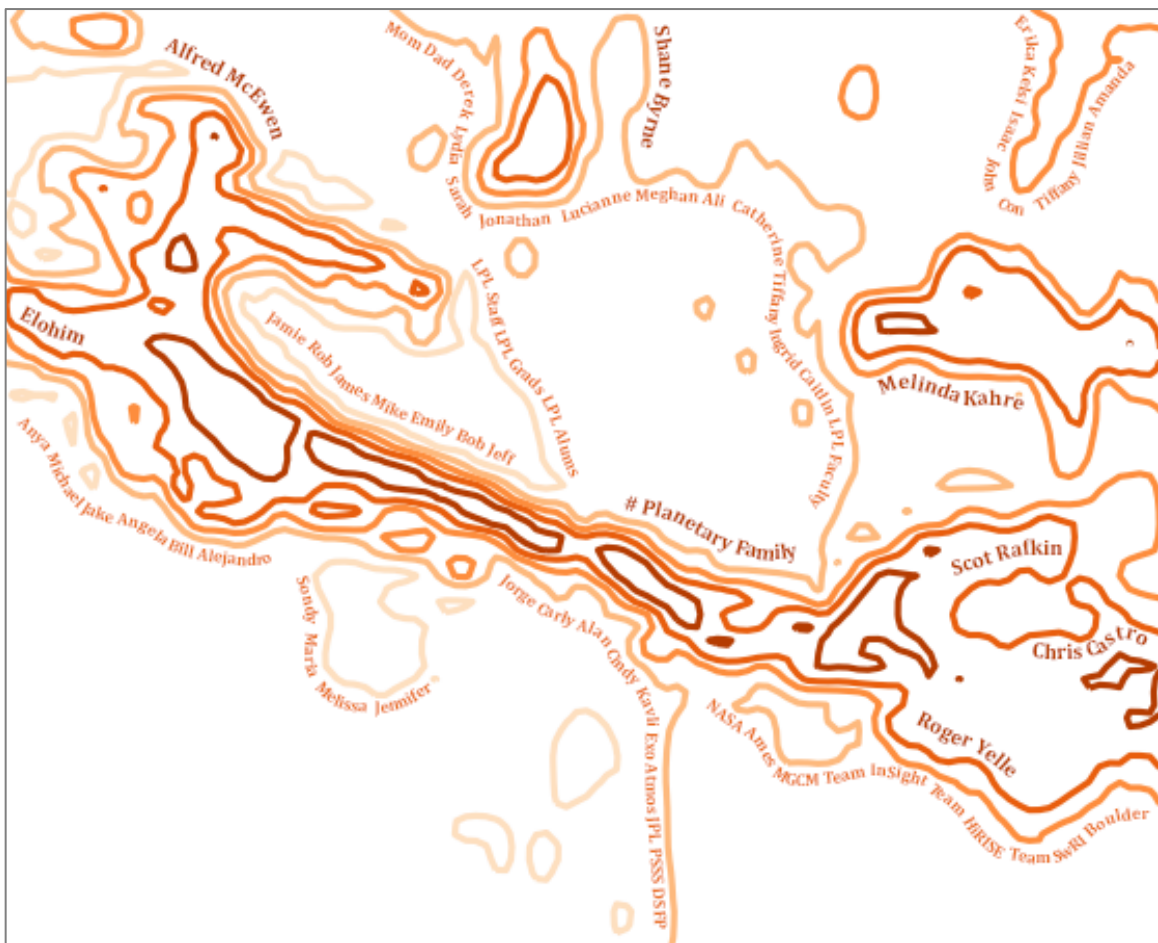
  
\_\_\_\_\_  
[Committee Co-Chair 2 Scot Rafkin] Date: 1/7/20

Dissertation Committee Co-Chair  
[Southwest Research Institute Boulder]



## ACKNOWLEDGEMENTS

I would like to express my deepest gratitude to my biological and my academic family, those who have given much of themselves to support me on this journey. My heart is forever grateful for the guidance of my dissertation committee, and for the mentors who have trained me to collapse the wave function, and not to feed the llamas any quinoa.



## **DEDICATION**

To the immigrants, the under-represented, and the dreamers.

In order to win, you have to play.

Should the stars align, change the rules along the way.

## TABLE OF CONTENTS

<b>ABSTRACT</b> .....	<b>10</b>
<b>CHAPTER 1 INTRODUCTION: THE PRESENT-DAY WATER CYCLE ON MARS</b> .....	<b>11</b>
1.1 THE MARTIAN WATER CYCLE.....	11
1.1.1 Why do we care about water on Mars?.....	11
1.1.2 Major H <sub>2</sub> O Reservoirs.....	12
1.2 GLOBAL ATMOSPHERIC CIRCULATION OF WATER.....	17
1.2.1 Interannual Variability .....	18
1.2.2 Seasonal Variability.....	19
1.3 REGIONAL ATMOSPHERIC CIRCULATION OF WATER.....	31
1.3.1 Vertical Distribution of Water.....	33
1.4 OVERVIEW OF THESIS INVESTIGATIONS .....	40
1.4.1 Significance of this Study.....	40
1.4.2 Science Objectives .....	42
1.4.3 Relevance to Planetary Exploration Goals .....	43
<b>CHAPTER 2 NUMERICAL MODELING OF THE MARTIAN ATMOSPHERE</b> .....	<b>45</b>
2.1 NUMERICAL MODELING OF THE MARTIAN ATMOSPHERE.....	45
2.1.1 Numerical Atmospheric Models.....	45
2.1.2 Structure of 3D Circulation Models .....	47
2.2 NASA AMES GENERAL CIRCULATION MODEL.....	49
2.2.1 NASA Ames Mars General Circulation Model (MGCM).....	49
2.3 THE MRAMS MESOSCALE MODEL .....	53
2.3.1 MRAMS Heritage.....	53
2.3.2 MRAMS Model Specifics .....	54
2.3.3 MRAMS Validation .....	61
<b>CHAPTER 3 IMPLICATIONS OF FOG IN VALLES MARINERIS</b> .....	<b>62</b>
3.1 INTRODUCTION .....	62
3.2 METHOD .....	66
3.2.1 Grid Configuration .....	66
3.2.2 Initialization & Boundary Conditions.....	69
3.2.3 Global Water Cycle at L <sub>s</sub> =38° .....	71
3.2.4 Regional Water Cycle at L <sub>s</sub> =38 .....	75
3.3 RESULTS.....	79
3.3.1 Simulation Results .....	79
3.3.2 Thermal Structure.....	81
3.3.3 Water Concentrations .....	86
3.4 DISCUSSION .....	92

3.4.1 Nature and Structure of the ‘fog’ .....	92
3.4.2 Effect of Thermal Inertia.....	92
3.4.3 Bias in Modeled Water Concentration .....	94
3.4.4 Potential Water Source?.....	94
3.5 CONCLUSION.....	96
<b>CHAPTER 4 ATMOSPHERIC INFLUENCES ON RECURRING SLOPE LINEAE ACTIVITY..</b>	<b>99</b>
4.1 INTRODUCTION .....	99
4.2 METHODS.....	105
4.2.1 Model Description and Set-Up .....	105
4.2.2 Chlorine-Bearing Salts .....	115
4.2.3 Seasonal Temperatures and Water Vapor Abundances .....	116
4.3 RESULTS.....	124
4.3.1 Regional Results at Four RSL Sites.....	124
4.4 DISCUSSION .....	142
4.4.1 Comparison of Expected Deliquescence with Observed RSL Activity .....	142
4.4.2 Effects of Dust .....	145
4.4.3 Kinetics of Deliquescence.....	148
4.4.4 Implications for RSL Formation Mechanisms .....	149
4.5 CONCLUSIONS.....	150
<b>CHAPTER 5 CONCLUSIONS.....</b>	<b>151</b>
5.1 CONCLUSIONS.....	151
5.2 FUTURE INVESTIGATIONS.....	154
<b>REFERENCES.....</b>	<b>163</b>

## LIST OF FIGURES

Figure 1.1 Present-day Mars seasonal water cycle .....	14
Figure 1.2 Global zonally-averaged (a) column water vapor, and (b) ice optical depth .....	18
Figure 1.3 Mars' Elliptical Orbit and Seasons .....	22
Figure 1.4 Northern summer advection of water from the north polar cap.....	26
Figure 1.5 Key Mechanisms affecting the Martian water cycle over an annual cycle.....	28
Figure 1.6 Spatial and Temporal Scales in the Atmosphere.....	32
Figure 1.7 Vertical profiles of water vapor mixing ratio .....	35
Figure 1.8 MCS profiles of temperature, and H <sub>2</sub> O ice extinction.....	36
Figure 2.1 Topographic map of Mars with Mars missions landing sites (NASA/JPL) .....	46
Figure 3.1 Image of potential morning ice fog in Valles Marineris. ....	64
Figure 3.2 MRAMS Model Configuration.....	68
Figure 3.3 Time series of the total column water in the canyon and above the plateau .....	70
Figure 3.4 Column vapor abundances in TES and the Ames MGCM. ....	72
Figure 3.5 Simulation results of water from the Ames Mars GCM at L <sub>s</sub> = 40°. ....	74
Figure 3.6 MOC cloud observation versus water ice clouds in MRAMS.....	76
Figure 3.7 Low-level circulation of water vapor on the grid-2 domain. ....	77
Figure 3.8 Diurnal variations of H <sub>2</sub> O ice mixing ratio .....	78
Figure 3.9 Baseline Column H <sub>2</sub> O ice optical depth .....	80
Figure 3.10 Diurnal cycle of temperature, total H <sub>2</sub> O, H <sub>2</sub> O vapor, and H <sub>2</sub> O ice mixing ratios .....	82
Figure 3.11 Baseline (a & b) vs. Flat (c & d) Thermal Inertia and albedo on grid-4.....	84
Figure 3.12 (a) Baseline vs. (b) constant thermal inertia and albedo simulation results .....	85
Figure 3.13 Total column H <sub>2</sub> O, column H <sub>2</sub> O vapor, and column H <sub>2</sub> O-ice.....	87
Figure 3.14 Near-surface winds and water vapor mixing ratio on grid-4 .....	88
Figure 3.15 Cross-sectional view of vertical and meridional winds.....	89
Figure 3.16 Vertical profiles of temperature, total water, water vapor and water ice.....	91
Figure 3.17 Fog event observed at the Grand Canyon, Earth.....	96
Figure 4.1 The location of the four RSL sites in this study .....	107
Figure 4.2 RSL site at Rauna Crater (35.260°N, 327.928°E) .....	110
Figure 4.3 RSL site at Krupac Crater (7.803°S, 86.059°E).....	112
Figure 4.4 RSL site at Garni Crater (11.516°S, 290.308°E) .....	113
Figure 4.5 RSL Site at Hale Crater (35.682°S, 323.484°E).....	114
Figure 4.6 Phase diagrams of four Cl-bearing salts .....	116
Figure 4.7 . TES versus model comparison for surface temperature and column water ....	120
Figure 4.8 Medium resolution (grid 5) versus high resolution (grid-8) MRAMS results ....	126
Figure 4.9 Diurnal cycle of surface temperature, relative humidity, and water vapor .....	127
Figure 4.10 Diurnal H <sub>2</sub> O flux (kg m <sup>-2</sup> s <sup>-1</sup> ) used in the model .....	129
Figure 4.11 Stability diagram for the CaClO <sub>4</sub> -H <sub>2</sub> O system at Krupac Crater during L <sub>s</sub> =20°.133	133
Figure 4.12 Seasonal temperature-relative humidity phase diagram at Krupac Crater .....	136
Figure 4.13 Simulated range of water extracted from the atmosphere.....	140
Figure 4.14 Likelihood of deliquescence vs observed RSL seasonality .....	143
Figure 5.1 Fit between an observed TES spectrum versus the best-fit synthetic spectrum	157



Figure 5.2 TES Geometric Weighting functions for the radiative transfer code..... 159  
Figure 5.3 Sample modeled water vapor vertical profile from the pilot study ..... 159

## LIST OF TABLES

Table 1.1 Chemical Composition of the Martian Atmosphere .....	16
Table 1.2 Select Planetary Parameters for Earth and Mars .....	21
Table 1.3 Spacecraft Observations of Water Vapor and Water Ice.....	37
Table 4.1 Characteristics of the four RSL study locations .....	106
Table 4.2 Baseline volumes of water vapor deliquesced at RSL study sites .....	141

## ABSTRACT

The investigation of water on Mars continues to be a quintessential objective in planetary exploration since water represents a critical link to Mars' past and present climate, geology, and its potential for habitability. Direct observations of water at the regional scale is limited, and the distribution and behavior of water in the planetary boundary layer remains an outstanding question. The research in this dissertation investigates the radiative and dynamical processes governing the regional water cycle on Mars. Using global and mesoscale atmospheric models, simulations of the regional water circulation revealed a highly non-homogeneous local distribution of water that is strongly modulated by diurnal transport. Terrain-following air parcels forced along the slopes of the Tharsis volcanoes and the steep canyon walls of Valles Marineris significantly impact the local water concentration and the associated conditions for cloud formation in these regions. An investigation of water ice fogs inside Valles Marineris showed significant variability between the local atmospheric environment inside versus outside the canyon. Formation of water ice clouds is possible in Valles Marineris, but their formation is highly influenced by radiative feedbacks forced by the thermal properties of the underlying surface. An evaluation of the potential influences of the atmosphere on recurring slope lineae (RSL) activity revealed an upper limit of  $\sim 1 \mu\text{m}$  per sol for the quantity of water that can be extracted from the atmosphere through deliquescence. Ongoing efforts to understand how regional atmospheric dynamics govern the distribution of water in the planetary boundary layer represent a significant step towards a comprehensive understanding of the water cycle on Mars.

## CHAPTER 1

### INTRODUCTION: THE PRESENT-DAY WATER CYCLE ON MARS

#### 1.1 The Martian Water Cycle

##### **1.1.1 Why do we care about water on Mars?**

The study of water on Mars continues to be a quintessential target in Mars exploration, as water has been emphasized as the critical link between the four overarching themes of geology, climate, habitability, and human exploration. Characterizing the processes controlling the abundances and behavior of water in the past and present climate is particularly important for untangling the evolutionary history of Mars. (1) The geological landscape on Mars shows strong evidence for the existence of water in the past, and contemporary flow features suggest that water continues to play a major role in shaping its surface morphology. (2) In addition, water is a key parameter in constraining the climatic state of the planet through radiative feedbacks, as well as the composition of the atmosphere via its role in the photochemical cycle. (3) The search for potentially habitable environments on Mars requires a thorough characterization of the temporal and geographical distribution of liquid water. (4) And finally, water serves as a critical asset for future human exploration of Mars as local reservoirs can be utilized as an in-situ resource. The characterization of the distribution and behavior of water is critical to NASA's exploration strategy of "Follow the Water", which begins with a solid understanding of the present-day water cycle on Mars.

### 1.1.2 Major H<sub>2</sub>O Reservoirs

In the present climate on Mars, the three major reservoirs of water are held in the polar ice caps, in the subsurface, and in the atmosphere. Current estimates suggest all these reservoirs combined would produce a global equivalent layer of liquid water of 20 to 30 meters. The largest reservoirs of water on Mars are found as icy layers particularly at the north and south polar caps, where an estimated total volume of  $(3.2 - 4.7) \times 10^6 \text{ km}^3$  of water ice resides (Seu et al., 2007). This volume contributes an upper limit of approximately two-thirds to the global inventory of water (Mouginot et al., 2010). Subsurface water on Mars exist as water vapor and ice within the regolith's interstitial pore space, adsorbed thin films on the surfaces of individual soil grains, chemically-bound hydrated and hydroxylated minerals, or as brines under suitable temperatures and vapor pressures where stability conditions are met (Montmessin et al., 2017). Of these forms of subsurface water, ground ice represents the largest identified reservoir. While the depth distribution of ground ice is still largely unknown, the upper meter of high-latitude regolith alone, assuming a nominal regolith porosity of 40%, contains an estimated global equivalent layer of at least 12 centimeters of water. Lastly, atmospheric sources of water present as both vapor and water ice make up the remainder of the global inventory of water on Mars.

Although the amount of atmospheric water accounts for only a small fraction of the global inventory, it nonetheless plays a critical role in governing the transport of water around the planet by acting as the primary conduit linking the various transient reservoirs of near surface water (Fig. 1.1). This is especially true for the northern polar ice cap,



representing the most extensive reservoir accessible to the atmosphere where the sublimation of seasonal H<sub>2</sub>O frost releases account for the majority of water vapor released into the atmosphere. In the present climate on Mars, the abundance of water in the atmosphere can vary seasonally by up to a factor of two due to the dynamic exchange of water forced by sublimation and deposition between the major reservoirs of water (Montmessin et al., 2017).

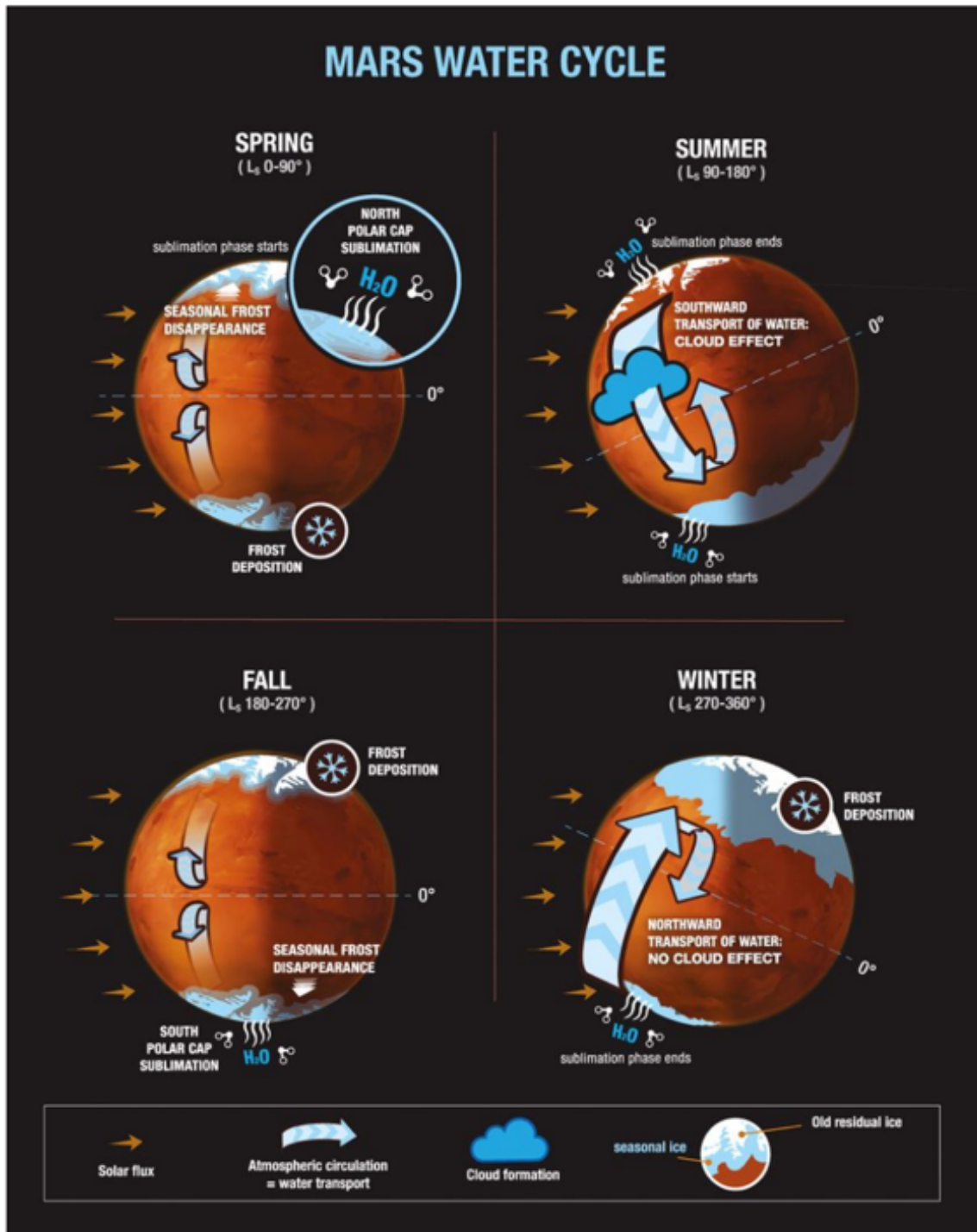


Figure 1.1 Present-day Mars seasonal water cycle illustrating the exchange of water between surface and atmospheric reservoirs. (Figure 11.1 in Montmessin et al., 2017)

The near-surface atmospheric composition on Mars consist of 95.32% Carbon dioxide (CO<sub>2</sub>), 2.7% Nitrogen (N<sub>2</sub>), 1.6% Argon (Ar), and 0.38 % trace gases of which includes 0.016% water (H<sub>2</sub>O) (Table 1.1). While water is a minor constituent in the primarily CO<sub>2</sub> dominated atmosphere, it is a critical component in the current Martian climate. In turn, climatic feedbacks heavily influence the behavior of water on Mars.

On average the surface temperature on present-day Mars ranges between 150 to 300K, and the surface pressure between 2 to 12 mbar. These conditions are cold enough such that CO<sub>2</sub>, the primary constituent of the atmosphere, freezes out in the winter time. With the exception of the deepest canyons, these surface conditions fall below the triple point of water of 6.11 mbar, where water sublimates and condenses between the ice and vapor, bypassing the liquid phase. Furthermore, the freezing point of water lies above the freezing point of CO<sub>2</sub> at Martian surface pressures. An important consequence of this is that water frost will be first to condense out of the Martian atmosphere and accumulate on the surface of the northern polar ice cap as the temperature begins to drop below the freezing point of H<sub>2</sub>O in late northern summer. The reverse process occurs in northern spring as CO<sub>2</sub> vaporizes first leaving behind only water ice in the Martian residual cap. As a result, the exchange of water between reservoirs is especially dynamic in the north polar region as ice seasonally advances and retreats along the edges of the polar cap, providing constant hydrological interaction between the regolith and the atmosphere.

Estimates of up to one third of the mass of atmospheric water exchanges seasonally between the two hemispheres during the summer and winter solstitial seasons (McCleese et

al., 2010; Montmessin et al., 2017). Therefore, atmospheric water is especially important in the water cycle since atmospheric circulation is the primary avenue by which water is transported around the planet, enabling global redistribution of water and exchanges between the reservoirs.

<b>Major constituents:</b>	<b>Minor constituents:</b>
<i>Carbon dioxide (CO<sub>2</sub>) - 95.32%</i>	<i>Oxygen (O<sub>2</sub>) - 0.13%</i>
<i>Nitrogen (N<sub>2</sub>) - 2.7%</i>	<i>Carbon Monoxide - (CO) - 0.08%</i>
<i>Argon (Ar) - 1.6%</i>	<i>Water vapor (H<sub>2</sub>O) - 210ppm</i>
	<i>Nitric oxide (NO) - 100 ppm</i>
	<i>Neon (Ne) - 2.5 ppm</i>
	<i>Hydrogen-deuterium-oxygen (HDO)- 0.85 ppm</i>
	<i>Krypton (Kr) - 0.3 ppm</i>
	<i>Xenon (Xe) 0.08 ppm</i>

Table 1.1 Chemical composition of the Martian atmosphere

In addition to the critical role that the atmosphere plays in the global circulation of H<sub>2</sub>O around Mars, the atmosphere governs chemical stability as well as the rate of water loss to space. Water is a key chemical species in the Martian atmosphere. Tiny amounts of reactive water vapor appear to control the bulk composition of the Martian atmosphere. Carbon dioxide typically has a short lifetime due to photo dissociate to CO + O. However, the photolysis of H<sub>2</sub>O into H and OH, allows for the oxidization of OH with CO forming CO<sub>2</sub> and H. In this way, carbon dioxide, the primary chemical constituent in the Martian atmosphere, remains stabilized.

## **1.2 Global Atmospheric Circulation of Water**

This chapter introduces the fundamental processes and components of the present-day water cycle, and provides an overview of our understanding of the key mechanisms driving the behavior of water in the Martian atmosphere. The first detection of water vapor on Mars was observed in the near-infrared by (Spinrad & Richardson, 1963) on the Mount Wilson 100-inch refractor telescope. Subsequent ground-based observations revealed that the disk-averaged seasonal water vapor column abundances varied by a factor of two with seasonal maxima shortly after the solstices (Montmessin et al., 2017). Interplanetary spacecraft orbiting around Mars over the past few decades have significantly augmented to this picture by returning a rich set of data to help establish our current understanding of the Martian hydrological cycle. The Mars Atmospheric Water Detector (MAWD) onboard the Viking 1 & 2 orbiters provided the first systematic multi-annual maps of water vapor on Mars with both spatial & seasonal coverage (Jakosky & Farmer, 1982). Later, the Thermal Emission Spectrometer (TES) aboard the Mars Global Surveyor (MGS) retrieved water vapor column abundances from thermal infrared spectra over three Mars years (1997 to 2004) that established the reference climatology of atmospheric water (Smith, 2004). The Mars Reconnaissance Orbiter (MRO) Compact Reconnaissance Imaging Spectrometer for Mars (CRISM) instrument observes water vapor at 2.56  $\mu\text{m}$  (Smith et al., 2009), and the Mars Express Orbiter (MEX) monitors water with three separate instruments: the Visible and Infrared Mineralogical Mapping Spectrometer (OMEGA) at 2.56  $\mu\text{m}$ , the Planetary Fourier Spectrometer (PFS) 2.56  $\mu\text{m}$  and 30  $\mu\text{m}$ , and the Ultraviolet and Infrared Atmospheric



Spectrometer (SPICAM) at 1.38  $\mu\text{m}$ . SPICAM in particular uses solar occultations to observe the vertical distribution of water vapor (Fedorova et al., 2009; Maltagliati et al., 2011).

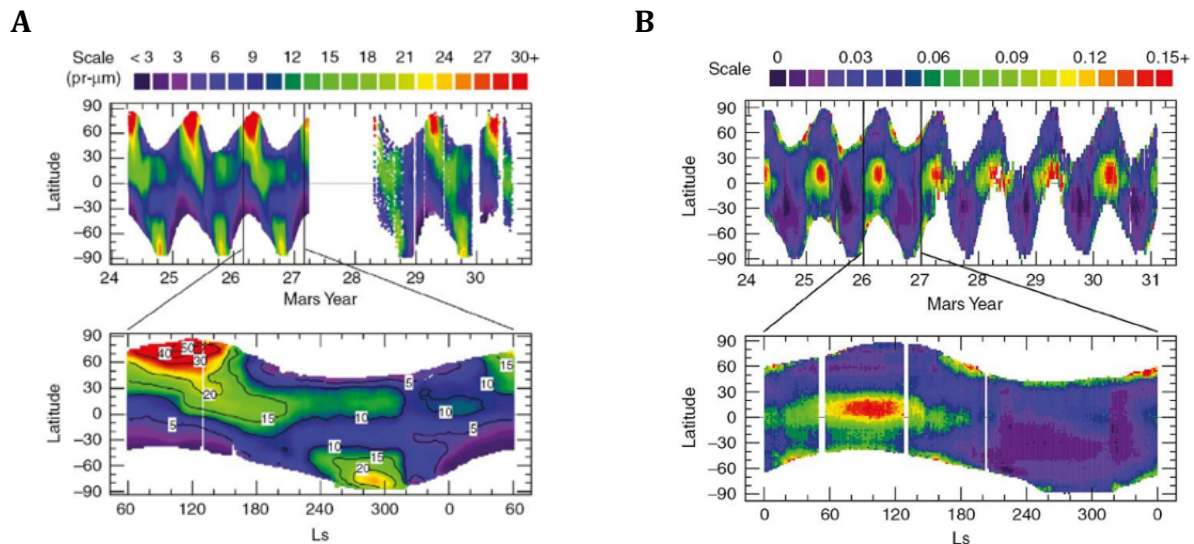


Figure 1.2 Global zonally-averaged (a) column water vapor, and (b) ice optical depth at 12  $\mu\text{m}$ . Results from TES (MY 24-27) and CRISM (MY 28-30) are shown. (Smith, 2004; 2009).

### 1.2.1 Interannual Variability

The essence of the Martian water cycle can be understood in terms of vast, exposed reservoirs of surface ice interacting with the atmosphere whose circulation is vigorous enough to transport water from one pole to the other and back, thereby closing the water budget on an annual basis. Apart from some evidence of modest interannual variability, results from the orbital instruments have shown that the behavior of water in the Martian atmosphere reproduces nearly the same global and seasonal trends year after year, evolving

in a quasi- steady state. Interannual differences in water distribution primarily arises during global dust storms, and appears in the slight year-to-year variation of the annular structure of water vapor near the north polar region especially around northern summer (Pankine et al., 2010). But overall, the repeatability of general patterns in the water cycle suggests that the mechanisms shaping the seasonal and spatial distribution of water operate in a similar way on Mars each year (Fig. 1.2).

### **1.2.2 Seasonal Variability**

While the interannual water cycle maintains a near stationary state, the seasonal water abundances on Mars undergo pronounced variability reflecting the seasonal changes in planetary insolation, atmospheric dynamics, aerosol distributions, and exchanges between various water reservoirs. In particular, the seasonal water cycle is predominantly controlled by the climatic variations at the north pole, due to the distinct asymmetry between the north and south polar ice caps on Mars.

Mars' orbital eccentricity is higher than that of the Earth's leading to an elliptical orbit where the subsolar heat flux received at aphelion is only ~70% that received during perihelion. Table 1.2 provides a brief comparison of selected planetary parameters between Earth and Mars. Seasons on Mars are defined by the solar longitude ( $L_s$ ), or the Mars-Sun angle, as measured from the northern hemisphere vernal equinox.  $L_s=0^\circ$  corresponds to the beginning of northern spring,  $L_s=90^\circ$  the northern summer solstice,  $L_s=180^\circ$  marks the northern autumnal equinox, and  $L_s =270^\circ$  the northern winter solstice. Aphelion occurs at  $L_s = 71^\circ$  close to the time of northern summer solstice, while perihelion occurs at  $L_s = 251^\circ$  near

southern summer solstice (Fig. 1.3). As such, northern summers are generally cooler and longer while southern summers are warmer but shorter, resulting in an annual mean temperature that is actually higher in the north than in the south. Seasonal H<sub>2</sub>O and CO<sub>2</sub> ice deposits in the north polar region occupy the greatest spatial extent during the cold winter season. In the spring, this seasonal cap sublimates uncovering a 3 kilometer-thick perennial dome of water ice poleward of 80°N during the summer months (Farmer, 1976; Kieffer et al., 1976). In contrast, the cooler annual mean temperature in the southern hemisphere results in the south polar ice cap being perpetually covered by a thin, meters-thick veneer of CO<sub>2</sub> ice sequestering the underlying bulk water ice and preventing H<sub>2</sub>O from regularly interacting with the atmosphere on a seasonal basis (Bibring et al., 2005; Paige et al., 1990). Thus, the seasonally exposed water ice deposits at the north pole accounts for the most extensive reservoir of water accessible to the atmosphere, and plays a major role in governing the seasonal dependence of water in the Martian atmosphere by establishing the driving boundary conditions upon which most of the seasonal activity of water depends.

	<b>Earth</b>	<b>Mars</b>
<i>semi-major axis (AU)</i>	1.0	1.52
<i>eccentricity</i>	0.017	0.0934
<i>obliquity</i>	23.5°	25.19°
<i>rotation rate, <math>\Omega</math> (<math>10^{-5} s^{-1}</math>)</i>	7.294	7.088
<i>solar day</i>	24hr	24hr 39m 35s
<i>year length (sol)</i>	365.24	668.6
<i>planetary radius, a (km)</i>	6380	3390
<i>deformation radius, <math>L=NH/\Omega</math> (km)</i>	1100	920
<i>mean albedo</i>	0.3	0.15
<i>surface gravity, g (<math>m s^{-2}</math>)</i>	9.81	3.72
<i>surface pressure, p (Pa)</i>	101300	610
<i>equilibrium temperature, <math>T_e</math> (K)</i>	256	210
<i>scale height, <math>H=RT/g</math> (km)</i>	7.5(7.6)	10.8 (10.3)
<i>specific gas constant, R (<math>m^2 s^{-2} K^{-1}</math>)</i>	287	192
<i>specific heat at constant pressure, <math>C_p</math> (<math>m^2 s^{-2} K^{-1}</math>)</i>	1000	860
<i>dry adiabatic lapse rate, <math>\Gamma_a = -g/C_p</math> (<math>K m^{-1}</math>)</i>	9.8	4.3
<i>average lapse rate lowest scale height, <math>\Gamma</math> (<math>K m^{-1}</math>)</i>	6.5	2.5
<i>bulk radiative timescale, <math>\langle \tau_r \rangle</math> (<math>10^5 s</math>)</i>	40	2
<i>typical zonal wind at jet level, U (<math>m s^{-1}</math>)</i>	30	80
<i>planetary rossby number, <math>Ro=U/\Omega a</math></i>	0.05	0.2
<i>buoyancy frequency, N (<math>10^{-2} s^{-1}</math>)</i>	1.1	0.6

Table 1.2 Select planetary parameters for Earth and Mars

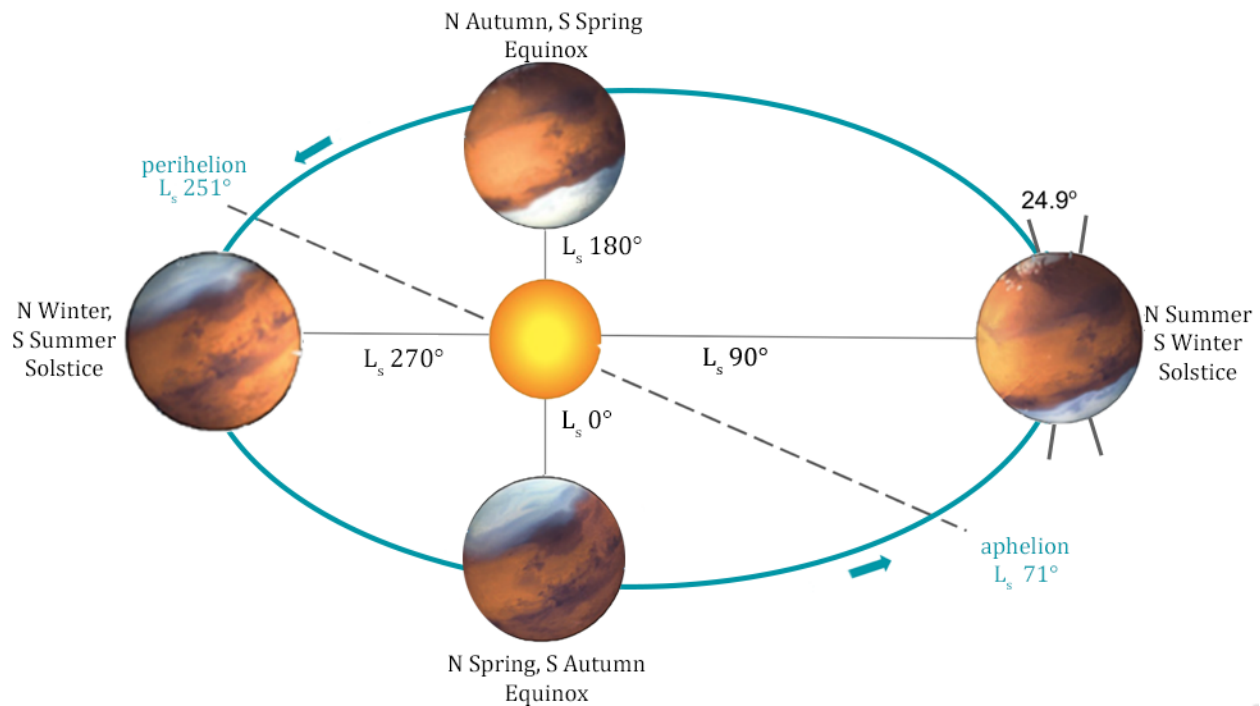


Figure 1.3 Mars' Elliptical Orbit and Seasons

The circulation of water on Mars is regulated by atmospheric waves, whose effect is to relax latitudinal gradients of heat and tracers such as water. Once a water molecule sublimates from the northern seasonal polar cap during northern spring, it can be carried by winds towards the equator and incorporated into the overturning circulation which distributes air masses and moisture to other regions of the planet. The Hadley circulation, stationary waves, and transient waves serve as the main mechanisms governing the global transport of water on Mars. The Hadley circulation is primarily responsible for the cross-equatorial transport of water from the northern hemisphere to the southern hemisphere and back. Most of the cross-equatorial transport of water takes place during the solstitial seasons ( $L_s = 90^\circ$  and  $270^\circ$ ) when the Hadley circulation is dominated by a single overturning cell



(Haberle, Leovy, & Pollack, 1982; Haberle et al., 1993). Rising motion in the summer tropics lifts water in the ascending branch of the Hadley cell enabling water in the atmospheric column to mix vertically over great depths, while downwelling in the descending branch deposits water in the mid-latitudes of the winter hemisphere (Forget et al., 1999; Read & Lewis, 2004). Approximately  $10^{12}$  kg of water vapor, or around 50% of the mass of water sublimating from the north polar, participate in the annual exchange of water from the north to the southern hemisphere and back through the solstitial Hadley circulation (Houben et al., 1997; Montmessin et al., 2004). During the equinoxes ( $L_s=0^\circ$  and  $180^\circ$ ), the Hadley circulation is divided into two uneven sub-cells, rendering the circulation of water to become much weaker and more sluggish during this time compared to the solstices.

While the cross-equatorial exchange of water is primarily achieved through the overturning circulation, the asymmetry of the structure of the Hadley cells during the two solstices lead to significant differences in the regimes by which water is distributed in the two hemispheres. Mars' absence of an ozone layer allows the depth of the Hadley cell to extend well above the height of the tropopause. Additionally, due to the more intense rate of solar insolation near perihelion, the vertical column can achieve much deeper mixing during southern summers compared to northern summer. Near aphelion, the average atmospheric temperature is at a minimum during northern spring. The altitude of water saturation is low and water vapor has been observed to remain below an altitude of 10km (ie. the Aphelion Cloud Belt). Meanwhile, southern spring occurs near perihelion. The average atmospheric temperature is higher, and the saturation altitude in the tropics can reach up to 40 to 60 km (Clancy et al., 1996; Jakosky, 1985). Cooler temperatures during the

northern summer solstice means the saturation altitude falls below the height of the upper cross-equatorial branch of the Hadley cell. The conversion of water vapor to water ice clouds in the northern tropics is manifested as the Aphelion Cloud Belt. Due to cloud formation, the cross-equatorial transport of water from the north to the south is restricted primarily to water in the condensed phase, which is heavier and less efficient than the conveyance of water vapor. Conversely, the shorter but more intense heating during southern summers brings the saturation height above the top of ascending branch, allowing water in the vapor phase to participate in the south to north cross-equatorial transport. Evidence for deep mixing during southern spring and summer is supported by the existence of significant quantities of aerosols and water vapor up to 70 km. The consequences of the seasonal variation of the cross-equatorial Hadley circulation result in a corresponding asymmetry in the height at which tropical water ice clouds form, creating a non-linear pump favoring water transport to the north at the expense of the south. At the same time, more intense solar insolation during southern summer causes more vigorous mixing in the atmosphere, so water vapor becomes more easily transported elsewhere and less likely to linger in the southern hemisphere. During northern summer, roughly 85% of all water resides in the northern hemisphere, while only 60% of all water dwells in the southern hemisphere during southern summer.

In addition to the Hadley circulation, higher-order planetary waves further control the poleward and equatorward fluxes of water especially in the mid- and high latitudes as they propagate latitudinally and vertically in the atmosphere (Haberle et al., 2017; Zurek et

al., 1992). Surface properties on Mars induces a number of stationary & transient waves which in turn influences how water is transported in the atmosphere. The lack of oceans on present-day Mars generally limits the planet's capacity to store heat which results in the surface's quick response to changes in insolation as well as significant diurnal and seasonal variations in the atmospheric temperature structure. Thermal inertial, which typically reflects the differing particle sizes and underlying properties of the soil, varies significantly on Mars, exhibiting an especially distinct wave-3 zonal structure in the 45-70°N latitudinal band (Putzig & Mellon, 2007). These patterns impose significant longitudinal surface temperature contrasts, which in turn induces stationary patterns of forcing on the atmosphere resulting in large scale 'thermal continents' that somewhat parallels ocean-continent thermal contrasts, or land-sea breeze, on Earth. Topography also strongly influences the local and global scale transport of water by forcing the presence of planetary waves as large-scale winds conform to the rise and fall of topographic contours associated with large obstacles such as volcanic regions or landmasses. The Martian landscape is dominated by a 4 km on average planetary dichotomy separating the plateaus in the southern highlands from the basins in the northern lowlands. But at high northern latitudes near the edge of the seasonal north polar cap, a prominent topographic zonal wavenumber 3 advection pattern emerges. Retraction of the seasonal polar ice cap occurs during the northern summer from  $L_s \sim 90^\circ$  to  $120^\circ$ , where water vapor sublimating off the north seasonal cap is carried by strong cyclonic flow locked into a zonally asymmetric wave-3 configuration, thereby confining equatorward transport of water primarily within three longitudinal corridors in association with Acidalia, Arcadia & Utopia Planitiae (Fig. 1.4).

While stationary eddies represent only the circulation residuals in the global transport of water, the cap-edge convergence stationary weather pattern along with a small contribution from the summertime sea-breeze circulation play a critical role in the water cycle by carrying sublimated water within reach of the transport mechanisms that convey water towards lower latitudes (Haberle & Jakosky, 1990). In the southern hemisphere, summertime polar extraction of water vapor is accomplished primarily through two wet filaments associated with the eastern rims of Argyre and Hellas Basin. Overall water extraction from the south pole is less effective compared to the north, and water vapor abundances are consistently higher at the northern hemisphere summer pole.

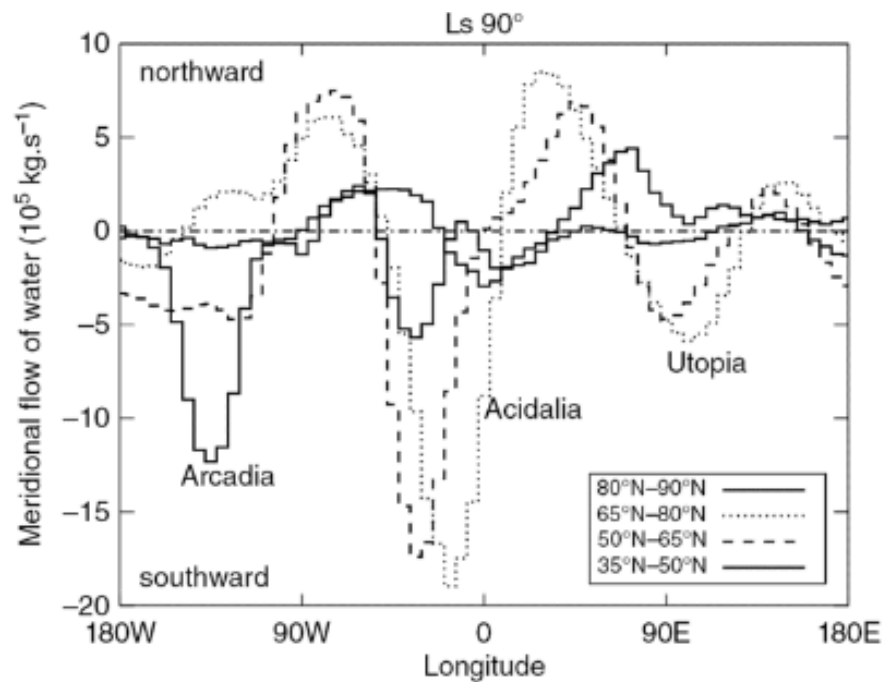


Figure 1.4 Northern summer advection of water from the north polar cap. Meridional flows of water have been obtained from the vertical integration of the simulated water vapor density times the meridional wind and averaged over four latitudinal belts (Figure 11.17 in Montmessin et al., 2017).

Stationary eddies are important for extricating water vapor away from the poles and extending it within reach of the global Hadley circulation, whereas traveling waves are critical for maintaining the stability of the polar ice caps by directing the return of water back to the north and south poles. The seasonal cap edge hosts a variety of propagating disturbances and transient eddy activity generated by baroclinic instabilities across the boundary of the polar vortex, especially during late northern winter and spring as shown in figure 1.5 (Barnes, 1981; Tillman, Henry, & Hess, 1979). Water vapor responds to these regional dynamical perturbations resulting in horizontal transport as well as abrupt water upsurges that influence the vertical distribution of water vapor (Maltagliati et al., 2013). Models indicate that roughly about 50% of the water sublimating off the northern seasonal cap contribute to the increase of vapor in the atmospheric columns overlying sublimation zones and participate in the global circulation, while the other 50% recondenses at the cap by means of the process referred to as the Houben Mechanism (Houben et al., 1997; Bass & Paige, 2000; Montmessin et al., 2004; Pankine et al., 2010; Richardson & Wilson, 2002). Water ice-sublimation is governed by the westward propagating diurnal thermal tide, while baroclinic waves travel eastward with a dominant period of three days. As a result, regions of intense cross-frontal horizontal mixing at the polar vortex boundary create deep poleward intrusion of H<sub>2</sub>O-enriched air masses. Regions of enhanced frost deposition extend up to 15 degrees poleward of the sublimation front and gradually allowing water ice to creep back to the poles in a 'quasi-solid' return motion (Richardson & Wilson, 2002). Frost accumulation at the poles is further forced by the remaining seasonal CO<sub>2</sub> ice poleward of the water ice annulus acting as a cold trap for any residual humidity in the dry polar atmosphere.

Meanwhile, cold polar air in the equatorward phase of the eddies give rise to thick water ice clouds forming the polar hood. Horizontal mixing achieved through travelling wave activity is therefore key to the stability of the water cycle by providing an effective way for polar reservoirs to seasonally recycle water that sublimates during spring and summer.

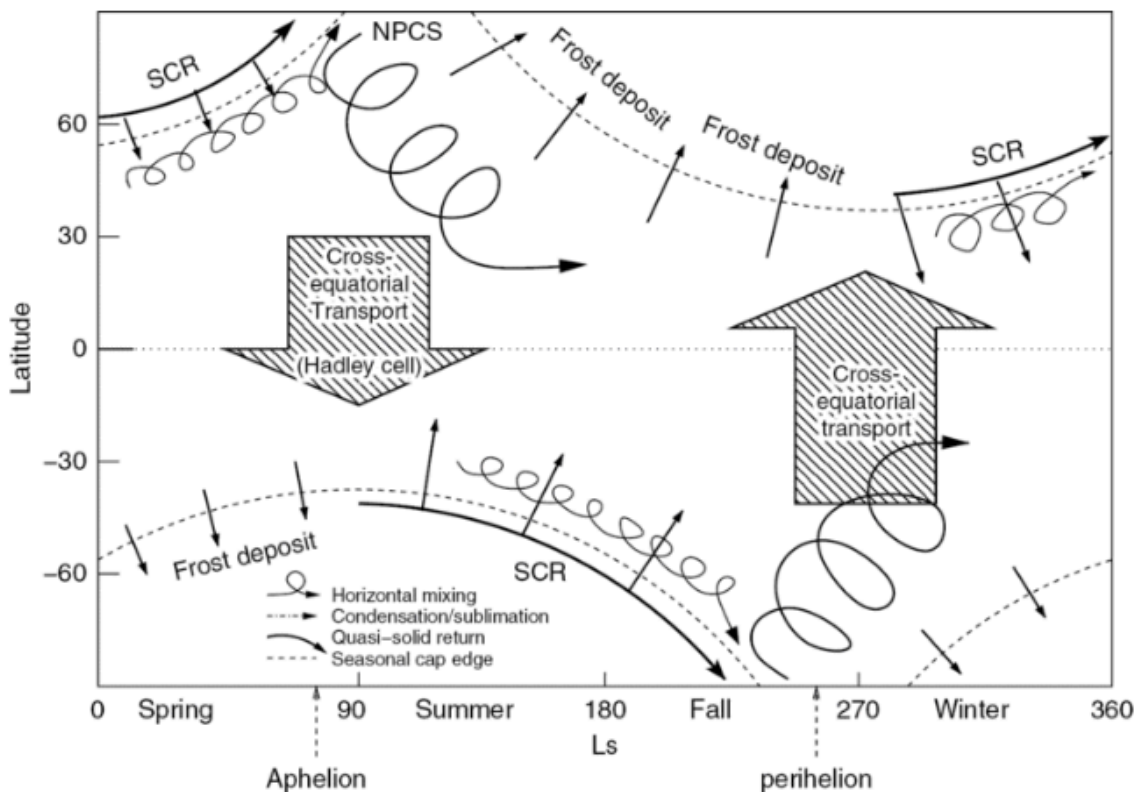


Figure 1.5 Key Mechanisms affecting the Martian water cycle over an annual cycle (Montmessin et al., 2004)

General circulation models of the Martian atmosphere have been instrumental in establishing the theoretical three-dimensional nature of the annual hydrological cycle on Mars, as well as for providing a comprehensive explanation of many major seasonal features observed in the water vapor column abundances climatological maps. Beginning mid-northern spring ( $L_s \sim 40^\circ$ ), the abrupt onset of water ice sublimation from the north polar cap

as it becomes exposed by the retreating seasonal CO<sub>2</sub> frost lead to a significant increase in the water vapor column abundance as well as the formation of a H<sub>2</sub>O annulus round the edge of the receding polar ice cap as massive quantities of water are injected into the atmosphere (Pankine et al., 2010). The annual globally integrated water abundance peaks around  $L_s = 110-120^\circ$  after the bulk of the seasonal polar cap sublimates. During early northern summer ( $L_s = 90-120^\circ$ ), horizontal mixing drives the migration of nearly half of the water vapor towards lower latitudes within three longitudinal corridors as evidenced by the equatorward expansion of water vapor concentrations. The northern summer Hadley circulation achieves its maximum development near the solstice, enabling a net north-to-south cross-equatorial exchange of water between the two hemispheres. After  $L_s = 130^\circ$ , water vapor abundances rapidly decrease in the north polar region falling to less than 10  $\mu\text{m}$ . Meanwhile in the southern hemisphere, a deep minimum in water vapor develops as the cold winter polar nights drive water vapor partial pressures towards nearly undetectable quantities. Contrary to the water vapor behavior in the south, no equivalent deep minimum occurs during northern winter due to the formation of water ice clouds between the equator and  $30^\circ\text{N}$  that leads to the partial sequestration of water vapor at low northern latitudes throughout northern fall and winter. Rather than an abrupt springtime upsurge in water vapor, a gradual seasonal rise in water vapor concentrations in the southern hemisphere occurs over two main pulses of activity. The majority of water vapor increase in the south is accounted for during the earlier pulse in the late southern winter and early spring ( $\sim L_s = 180^\circ$ ) resulting from the cross-equatorial transport of water from the northern hemisphere, while the second smaller H<sub>2</sub>O vapor increase at high southern latitudes from  $L_s$

=220-300° is due to the sublimation of the south seasonal polar cap, analogous to the equivalent  $L_s = 40^\circ$  vapor increase in the north. Maximum water vapor column abundance in the southern hemisphere peaks around  $L_s \sim 290^\circ$ , but corresponds to only  $\sim 50\%$  of the northern hemisphere summer maximum value. Mars' eccentric orbit imposes significantly warmer temperatures ( $\sim 20\text{K}$ ) during southern summers compared to northern summers which in turn imposes a severe imbalance in the stability of ice between the two poles. Powerful sublimation flow off the receding southern  $\text{CO}_2$  ice cap in addition to more intense equatorward advection favors the preferential return of water to the northern hemisphere through the Hadley circulation rather than residing perennially as frost at the south pole. Around mid-southern summer ( $L_s = 300^\circ$ ), the south polar water vapor maxima abruptly decay. The seasonal decay behavior in the south differs drastically from that of the north with no indication of enhanced equatorward, northward transport that would otherwise significantly contribute to the northern (springtime) water vapor maximum. To close the annual water cycle, the summertime extraction of water is compensated by an equivalent winter and springtime return of water to the poles. While the cross-equatorial transport is accomplished through the Hadley circulation, the extratropical climate during the northern autumn and winter season ( $L_s = 180\text{-}270^\circ$ ) is driven by baroclinic eddies and the latitudinal wandering of the polar vortex, both of which participate in the maintenance of the polar ice cap by depositing water ice frost along the growing the seasonal cap. The areal extent of the seasonal cap tracks the seasonal and latitudinal excursion of the polar night vortex boundaries, and frost deposition along the seasonal cap edge contribute to the gradual creep of water back to the north pole before the next summer sublimation event. Strictly speaking,



the hydrological cycle on Mars is not entirely 'closed'. The south polar CO<sub>2</sub> ice cap maintains a year-round surface temperature at the triple point of CO<sub>2</sub> ~145K, which acts as a cold trap causing a net transfer of 10<sup>10</sup> to 10<sup>11</sup> kg of water to be deposited every year at the surface near the south pole. This represents a permanent loss of 1-10% of the seasonal inventory of water vapor (Jakosky, 1983a, 1983b; Richardson & Wilson, 2002) on the residual CO<sub>2</sub> cap.

### **1.3 Regional Atmospheric Circulation of Water**

The atmospheric circulation of water on Mars is relevant over many spatial and temporal scales of interest (Fig. 1.6). The Hadley overturning circulation occurs over planetary scale, while transient weather systems such as baroclinic and barotropic instabilities, as well as topographic storm zones typically appear over timescales of days. Migrating thermal tides and their interaction with topography occur on diurnal timescales that results in morning ice clouds, fogs, frost, nocturnal jets, and other thermal contrast slope winds. The temporal-spatial domain of mesoscale phenomenon typically fall intermediary between microscale & large-scale systems. Atmospheric phenomenon that typically fall within the mesoscale include local katabatic and anabatic circulations, gravity waves, as well as local dust storms. Types of mesoscale circulation include thermal slope flows, gravity waves, bore waves & density currents, dust storms, and circulations producing water ice and CO<sub>2</sub> ice clouds.

$T_s$ $L_s$	1 MONTH	1 DAY	1 HOUR	1 MIN	1 SEC	
10,000 Km	STANDING WAVES	ULTRA-LONG WAVES	TIDAL WAVES			MACRO $\alpha$ SCALE
2,000 Km		BAROCLINIC WAVES				MACRO $\beta$ SCALE
200 Km		FRONTS & HURRICANES				MESO $\alpha$ SCALE
20 Km		NOCTURNAL LOW LEVEL JET SQUALL LINES INERTIAL WAVES CLOUD CLUSTERS MTN. & LAKE DISTURBANCES				MESO $\beta$ SCALE
2 Km			THUNDERSTORMS IGW URBAN EFFECTS			MESO $\gamma$ SCALE
200 m			TORNADOES DEEP CONVECTION SHORT GRAVITY WAVES			MICRO $\alpha$ SCALE
20 m			DUST DEVILS THERMALS WAKES			MICRO $\beta$ SCALE
					PLUMES ROUGHNESS TURBULENCE	MICRO $\gamma$ SCALE
C.A.S	CLIMATOLOGICAL SCALE	SYNOPTIC PLANETARY	MESO	MICRO		PROPOSED DEFINITION

Figure 1.6 Spatial and Temporal Scales in the Atmosphere.

### 1.3.1 Vertical Distribution of Water

The vertical distribution of water vapor is the product of a complex set of interactions involving temperature variations, convective & turbulent mixing, advection by winds, regolith-atmosphere exchange, and cloud microphysical processes such as condensation, evaporation, and sedimentation. While orbital spacecraft have provided a multi-annual climatology of the water vapor column abundances in the Martian atmosphere, how this water varies with height is still largely unconstrained.

A major factor constraining the vertical distribution of water relates to the saturation altitude of water and the formation of water ice clouds, which in turn is governed primarily by the vertical thermal structure of the atmosphere. The saturation vapor pressure (SVP) is determined by the Goff & Gratch (1946) reference formulation (Eq. 1.1). The saturation ratio (S) at a given temperature is defined by the ratio of local water vapor partial pressure to the equilibrium vapor pressure of either ice or liquid.

$$\ln P_{sat}^{ice} = 100 \left[ -9.09718 \left( \frac{T_0}{T} - 1 \right) - 3.56654 \ln \left( \frac{T_0}{T} - 1 \right) + 0.876793 \left( 1 - \frac{T_0}{T} \right) + \ln 6.11 \right]$$

Equation 1.1. *Saturation Vapor Pressure (SVP) equation by Goff and Gratch (1946)*

The first direct observation of water vapor vertical profiles was obtained by Phobos2 Auguste solar occultations, which measured a near-constant water vapor mixing ratio of ~100ppm below 20 km with a sharp decrease above 25 km (Fig. 1.7a). Spatially dispersed profiles of the vertical structure of water vapor and water ice have also been documented by SPICAM & MCS limb observations (Fig.1.7b, Fig. 1.8). As discussed in the previous section,

the saturation altitude presents a major hurdle for the vertical transport of water which contributes significantly to the asymmetric cross-equatorial circulation of water between the two solstitial seasons due to extensive water ice cloud formation at low northern latitudes during northern summers.

Retrievals of water vapor typically assume a uniformly well-mixed vertical distribution from the surface up to the water vapor condensation level (Maltagliati et al., 2011; Smith M.D., 2002; 2009). This assumption was supported by Viking Lander 1 (& MAWD), which measured a uniform water vapor distribution of 150 ppm below 10 km at  $L_s = 102^\circ$  (Davies, 1979). Phobos 2's observation of the vertical water vapor profiles at  $L_s = 1-19^\circ$  in the equatorial region also suggests a near constant mixing ratio at altitudes between 10 to 25 km that is capped by a sharp decrease above 23-25km (Rodin et al., 1997). In contrast, more recent observations and modeling efforts suggest that water vapor is not uniformly mixed in the lower atmosphere, but is preferentially concentrated near the surface. The multispectral stereo Imager for Mars Pathfinder (IMP) provided the first observation of water from the surface of Mars (Titov et al., 1999), and observed a dependence of  $H_2O$  vapor transmittance with sun elevation indicative of water vapor confinement to a layer 1 to 3 km thick near the surface. Global Circulation Models (GCMs) suggest that the water vapor mixing ratio in the lowest scale height can increase substantially with height, especially near the equator during northern summer (Navarro et al., 2014; Richardson, Wilson, & Rodin, 2002). The Phoenix Mars Lander (PHX), which operated in the north polar region, observed seasonal and diurnal variations in the vertical

distribution of H<sub>2</sub>O vapor abundances. The depth of the layer that experiences diurnal exchange of water with the surface is found to be 0.5-1 km indicating a more complicated vertical structure than the well-mixed assumption would suggest (Tamppari et al., 2010). Pankine & Tamppari (2015) further tested a non-uniform model of water vapor vertical distribution in the north polar region by defining a ‘wet’ layer height that is decoupled from the cloud condensation height. Their results show that the cloud condensation height does not cap the water vapor vertical distribution, and water vapor is not solely confined to the planetary boundary layer. These evidences suggest that the traditional uniformly well-mixed boundary layer assumption used in the current column-integrated measurements of retrieved water vapor abundances may carry significantly biases.

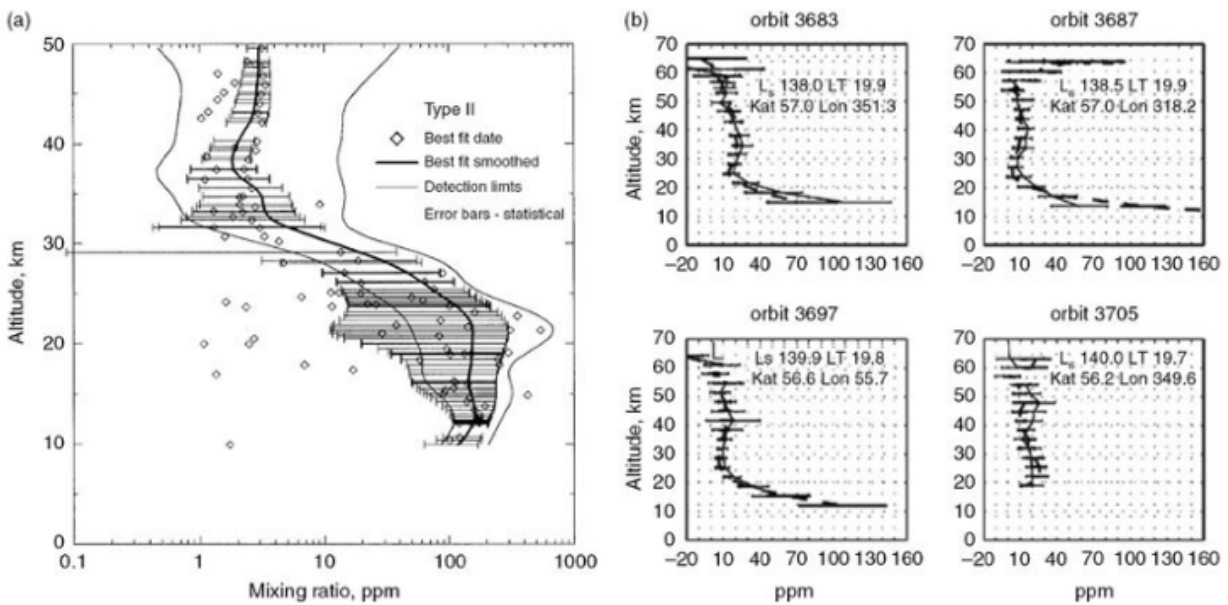


Figure 1.7 Vertical profiles of water vapor mixing ratio  
 Taken by (a) Auguste (Rodin et al., 1997), and (b) SPICAM (Fedorova et al., 2009)

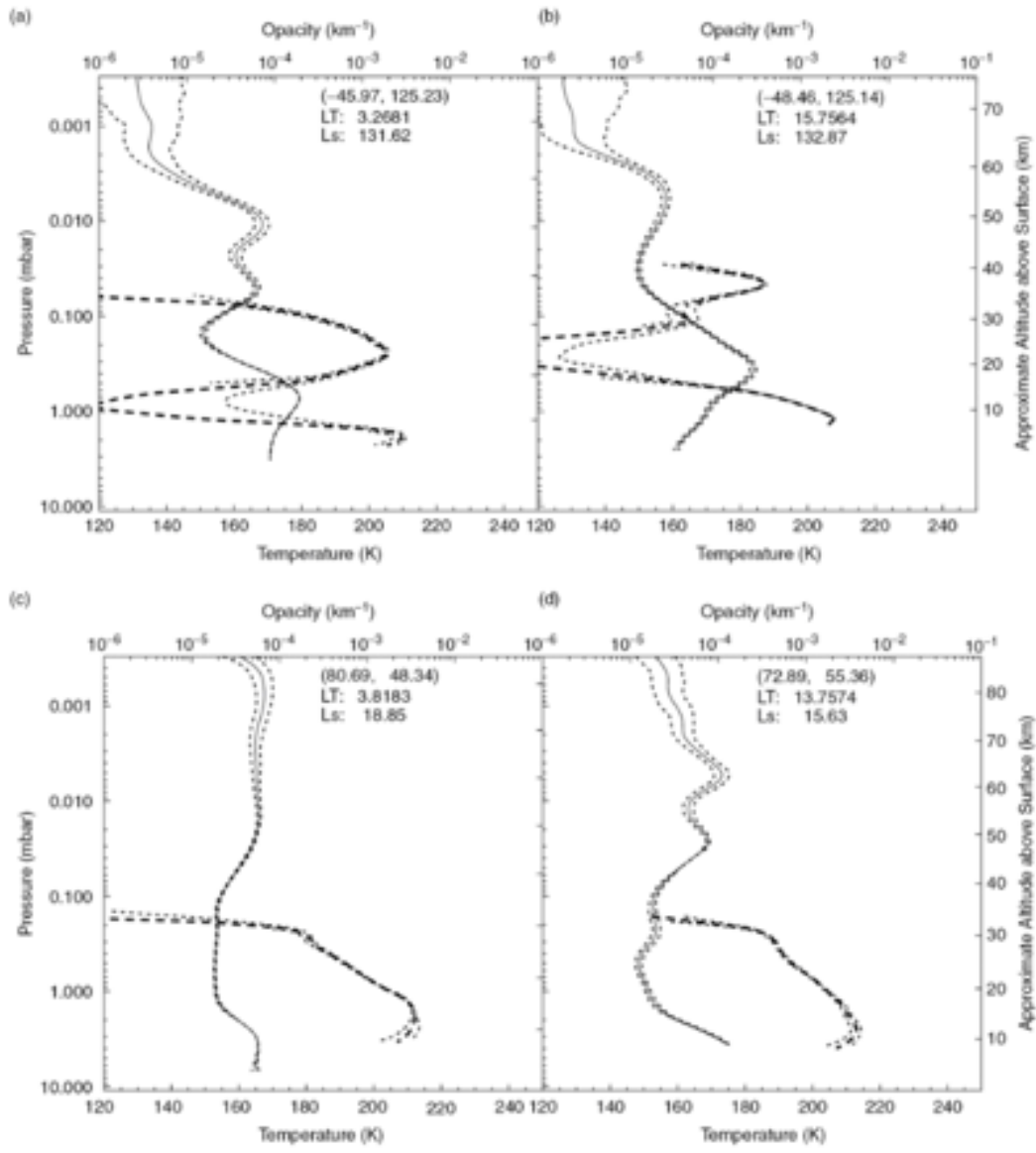


Figure 1.8 MCS profiles of temperature, and H<sub>2</sub>O ice extinction (Benson, Kass, & Kleinböhl, 2011)

<b>Spacecraft</b>	<b>Instrument</b>	<b>H<sub>2</sub>O vapor/ice Spectral Band</b>
<i>Mariner 9</i>	<i>IRIS</i>	<i>30 μm rotational band</i>
<i>Viking 1 &amp;2</i>	<i>MAWD</i>	<i>1.38 μm adsorption band</i>
<i>Phobos 2</i>	<i>Near-IR spectrometer</i>	<i>2.56 μm</i>
<i>MGS</i>	<i>TES</i>	<i>30 μm</i>
<i>Mars Express</i>	<i>PFS</i>	<i>2.56 μm, 30 μm</i>
	<i>OMEGA</i>	<i>2.56 μm</i>
	<i>SPICAM</i>	<i>1.38 μm</i>
<i>MRO</i>	<i>MCS</i>	<i>12 μm</i>
	<i>CRISM</i>	<i>2.56 μm</i>
<i>TGO</i>	<i>NOMAD, ACS</i>	<i>2.56 μm</i>
<i>Pathfinder</i>	<i>IMP</i>	<i>0.94 μm</i>
<i>MER</i>	<i>Mini-TES</i>	<i>30 μm rotation band</i>
<i>PHX</i>	<i>Lidar</i>	<i>0.935 μm (Similar to Pathfinder)</i>
<i>MSL</i>	<i>REMS</i>	<i>Relative humidity</i>

Table 1.3 Spacecraft Observations of Water Vapor and Water Ice on Mars by Orbital & Landed Instruments

Diurnal variability of water vapor and water ice is influenced by local processes such as condensation and sublimation on the surface or in the atmosphere, exchanges with the regolith, or through the passage of air masses of different origins. But the latter requires horizontal advection phased with the diurnal cycle, which is not the dominant periodicity of transport. Observational evidence for variability with local time is sparse and yields some conflicting trends. Maltagliati et al. (2011) did not find any prominent diurnal signature in the OMEGA measurements compared to TES, while Melchiorri et al. (2007) detected minor diurnal variations of a few  $\mu\text{m}$  during the day in OMEGA observations near the south pole. Pathfinder IMP detected evidence for horizontal inhomogeneity in water vapor abundances, but no significant variability from morning to evening. On the other hand, local diurnal

variations of water can reach a factor of 2 to 3, equivalent to an absolute abundance of  $\sim 10$  pr- $\mu\text{m}$ . Using the Thermal and Electrical Conductivity Probe (TECP), Phoenix detected near-surface ( $z \sim 2\text{m}$ ) atmospheric vapor pressure of 2 Pa during the day that rapidly fell to 0.1 Pa, a factor of 20 times smaller, by 20:00 local time (Smith et al., 2009). Coordinated observations by SSI and CRISM at  $L_s = 108.3^\circ$  showed diurnal fluctuations in water vapor of up to 15 pr- $\mu\text{m}$ . At the Phoenix landing site, a 5-10  $\mu\text{m}$  thick early-morning frost layer is observed along with a lack of surface frost activity in the late evening, as well as the formation and disappearance polar ice clouds amounting to a water content of no more than  $\sim 2$  pr- $\mu\text{m}$ . Tamppari et al. (2010) suggests that these observations cannot be solely accounted for by diurnal condensation-sublimation processes, but rather additional sources and sinks must be present to account for the 15 pr- $\mu\text{m}$  daily change in water vapor, including a substantial fraction of water up to 10 pr- $\mu\text{m}$  that may be controlled by exchanges with the regolith and the subsurface.

In addition to the evidence suggested by the Phoenix result, the Mars Express Planetary Fourier Spectrometer (PFS) ( $L_s = 330-60^\circ$  and  $90-220^\circ$ ) found an anti-correlation between water vapor and surface pressure, suggesting that exchange with the regolith could account for up to 3-4 pr- $\mu\text{m}$  of the global atmospheric inventory. Titov et al. (1999) and Tschimmel et al. (2008) also found indirect evidence of water confined within the lowest 3 km of the atmosphere. Experiments using column models show confinement of water vapor below 3 km in general, and especially in the first 100 meters above the surface is controlled by exchanges with regolith (Pathak et al., 2009; Savijärvi, 1995; Zent et al., 1993). In-situ



measurements of relative humidity carried out by the Rover Environmental Monitoring Station (REMS) instrument onboard the Curiosity Rover showed a very dry environment at Gale Crater but diurnal exchange with the regolith is still possible (Harri et al., 2014; Savijärvi, Harri, & Kemppinen, 2016).

The climate of Mars is characterized by complex feedbacks between CO<sub>2</sub>, water, and dust (Jakosky & Haberle, 1992), and the coupling of these three cycles has important implications for the behavior and distribution of water in the Martian atmosphere. First, dust and CO<sub>2</sub> ice grains participate in the formation of water ice clouds by serving as condensation nuclei. In the absence of dust aerosols or CO<sub>2</sub> ice particles, homogeneous nucleation on Mars, where water vapor condenses onto water ice embryos of a critical size, necessitates extreme supersaturation conditions that require saturation ratios exceeding 1000 (Colaprete & Toon, 1999; Määttänen et al., 2005; Michelangeli et al., 1993; Montmessin, Rannou, & Cabane, 2002). In contrast, heterogeneous nucleation on Mars, where water vapor directly deposits onto a dust or CO<sub>2</sub> solid substrates, requires much less energy to establish a mechanically stable interface between the crystal and its environment such that nucleation can commence once saturation ratios reach 1.2 to 2 (Iraci et al., 2010; Määttänen et al., 2005). Second, the formation of water ice clouds onto dust nuclei and the subsequent falling of cloud particles contributes to the scavenging of dust particles following the sublimation of dust-containing ice crystals at lower sub-saturated altitudes. This dust capping effect was confirmed by (Benson et al., 2011) using MCS observations. SPICAM observations in the mid-latitudes from  $L_s = 130-160^\circ$  during MY 28 also detected higher amounts of water vapor above

saturation altitude than expected from SVP (Fedorova et al., 2009). H<sub>2</sub>O vapor well in excess of the SVP by a factor up to 10 above the saturation level at 20 km was detected in the northern summer tropics during MY 29 (Maltagliati et al., 2011, 2013). The removal of dust by scavenging above the saturation level impede on the possibility for the remaining water to nucleate and condense there again. The coupling of the CO<sub>2</sub>, H<sub>2</sub>O, and dust cycles significantly contribute to climatic feedbacks especially in relation to radiative heating and cooling effects of CO<sub>2</sub> clouds, H<sub>2</sub>O clouds, and dust storms.

## **1.4 Overview of Thesis Investigations**

### **1.4.1 Significance of this Study**

How water circulates on the regional scale remains a major outstanding question towards a comprehensive understanding of the Martian water cycle. As an extension of the vertical distribution in three-dimensional space, the regional distribution of water reflects the complex interactions involving temperature variations and advection by winds, in addition to convective & turbulent mixing, regolith-atmosphere exchange, as well as cloud microphysical processes (Montmessin et al., 2017).

While remote sensing observations from orbit have provided a multi-annual climatology of the water vapor column abundances in the Martian atmosphere (Farmer et al., 1977; Pankine et al., 2010; Smith, 2002), no equivalent global climatology exist for the vertical distribution of water vapor. Measurements of the vertical water vapor distribution are very limited, lacking in regular temporal and spatial frequency due to the unique orbital

configuration required to take those measurements. Thus, how water varies with height is still largely unconstrained, and the vertical distribution of total water (vapor and ice) is unknown. Even still, orbital measurements are limited in spatial and temporal resolution, while measurements on landers and rovers are limited to only a handful of locations on the surface making it challenging to study how water is transported at the regional scale.

Processes in the planetary boundary layer mediate the exchanges of heat, momentum, dust, and water between the regolith and the free atmosphere. Limb-viewing atmospheric sounders can retrieve some information on the vertical distribution of aerosols such as dust and water ice (Maltagliati et al., 2013; McCleese et al., 2007). But they typically struggle to observe the bottom-most one to two scale heights due to limited path transmission resulting from increased dust and cloud optical thickness as well as topographic obstruction of limb tangent viewing geometries (Guzewich et al., 2017; Kleinböhl et al., 2009). Instruments on landers and rovers provide diurnal coverage in the lowest few kilometers of the atmosphere, but again lack the regional context which orbiters can acquire.

Apart from the limited observations of winds in the first few meters above the surface taken by meteorological instruments on landed spacecrafts, winds on Mars are almost entirely inferred from geostrophic balance from temperature retrievals. The lack of wind measurements with adequate spatial and temporal frequency make it difficult to determine how water vapor and water ice is advected at regional scales. We rely heavily on regional scale models to reveal mesoscale circulation and the advection of water in the boundary layer. Spacecraft measurements can only offer us snapshots of the Martian environment,

atmospheric models are used to provide context by filling in spatial and temporal gaps in the data, and ultimately generating a physically consistent picture of the underlying processes described by the observations.

#### **1.4.2 Science Objectives**

The primary objective of this dissertation is to investigate the physical and dynamical processes governing the regional water cycle on Mars. Using global and mesoscale atmospheric model simulations, this research assesses regional scale circulation and exchange of H<sub>2</sub>O in the planetary boundary layer, and constrains transport rates governed by the local environment.

**This dissertation seeks to address the following science questions:**

1. How is water distributed regionally on Mars? In particular, how do radiative forcing and dynamical processes moderate that distribution?
2. How do water ice fog form in Valles Marineris?
3. What are the influences of atmospheric water on RSL activity?

The findings of this dissertation help to quantify the seasonal and diurnal variability of water with respect to regional atmospheric circulations and fill in several critical gaps in our fundamental understanding of the water cycle in the Martian atmosphere. The results of these investigations help to characterize the relative significance of local H<sub>2</sub>O reservoirs with respect to the overall seasonal hydrological cycle in the Martian atmosphere, which have

important applications for evaluating local habitable environments and for understanding variability in meteorological systems on other planetary bodies.

### **1.4.3 Relevance to Planetary Exploration Goals**

The research in this dissertation directly addresses the scientific and exploration goals to characterize the state of the present climate of Mars' atmosphere. Specifically, the objectives to characterize the diurnal and seasonal water cycle and assess climatic feedbacks from water ice clouds with respect to regional atmospheric circulations directly constrain the processes controlling the present distributions of water, carbon dioxide, and dust in the lower atmosphere, at diurnal and seasonal timescales. Furthermore, our examination of the coupled surface-atmospheric exchange of water in the Martian planetary boundary layer supports The Robotic Mars Exploration Strategy calls for near-term investigations of the boundary layer, since it controls surface-atmosphere interactions, including water vapor exchange with the surface and subsurface that ultimately controls whether water is stable.

NASA's exploration strategy to "Follow the Water" begins with an understanding of the current state of the hydrological cycle on Mars. The spatial and temporal evolution of water in the Martian atmosphere remains an open question, especially on regional scales. This research directly addresses a fundamental knowledge gap in our understanding of the Martian water cycle by directly correlating subsurface-atmospheric vapor exchange to variations in the water distribution in the rest of the atmospheric column. These results have important future applications for our understanding of the dynamics in the Martian

meteorological system, feedbacks coupling the dust and water cycles, and for determining the relative significance of various local H<sub>2</sub>O reservoirs to the overall long-term Martian water budget.

## CHAPTER 2

### NUMERICAL MODELING OF THE MARTIAN ATMOSPHERE

#### 2.1 Numerical Modeling of the Martian Atmosphere

##### 2.1.1 Numerical Atmospheric Models

While images of clouds and dust can provide indirect information on atmospheric activity at regional scales, most comprehensive mesoscale studies of the Martian atmosphere rely on numerical computational models. Overall observational data that adequately cover the temporal-spatial range traditionally belonging to the mesoscale domain have been very limited. Remote sensing observations from orbit, in both nadir and limb-viewing mode, can retrieve some information on the vertical distribution of aerosols such as dust and water ice (L. Maltagliati et al., 2013; Daniel J. McCleese et al., 2007), but they typically struggle to observe the bottom-most one to two scale heights due to limited path transmission resulting from increased dust and cloud optical thickness as well as topographic obstruction of limb tangent viewing geometries (Guzewich et al., 2017; Kleinböhl et al., 2009). In situ measurements of mesoscale phenomenon are even more limited. Direct measurements of near-surface meteorology have currently only been observed at six locations by the Viking Landers 1 & 2, Mars Pathfinder, the Phoenix Mars Lander, the Curiosity Rover, and the InSight Lander (Fig. 2.1) (Martínez et al., 2017). The Mars Exploration Rovers, Spirit and Opportunity, did not carry a meteorological package on board, but were able to provide some indirect observations of water through clouds images. Furthermore, landed instruments provide diurnal coverage in the lowest few kilometers of the atmosphere, but lack the

regional context which orbiters can acquire. Snapshots of the Martian environment alone cannot uniquely constrain the relationships between atmospheric forcing and response. Due to the limited number of physical observations, much of what is known about the mesoscale on Mars is derived from regional climate model simulations. In conjunction with studies of terrestrial analogs, mesoscale atmospheric models represent one of the best tools to provide regional context for spacecraft observations by filling in spatial and temporal gaps in the data, and ultimately provide a physically consistent picture of the underlying processes described by the observations.

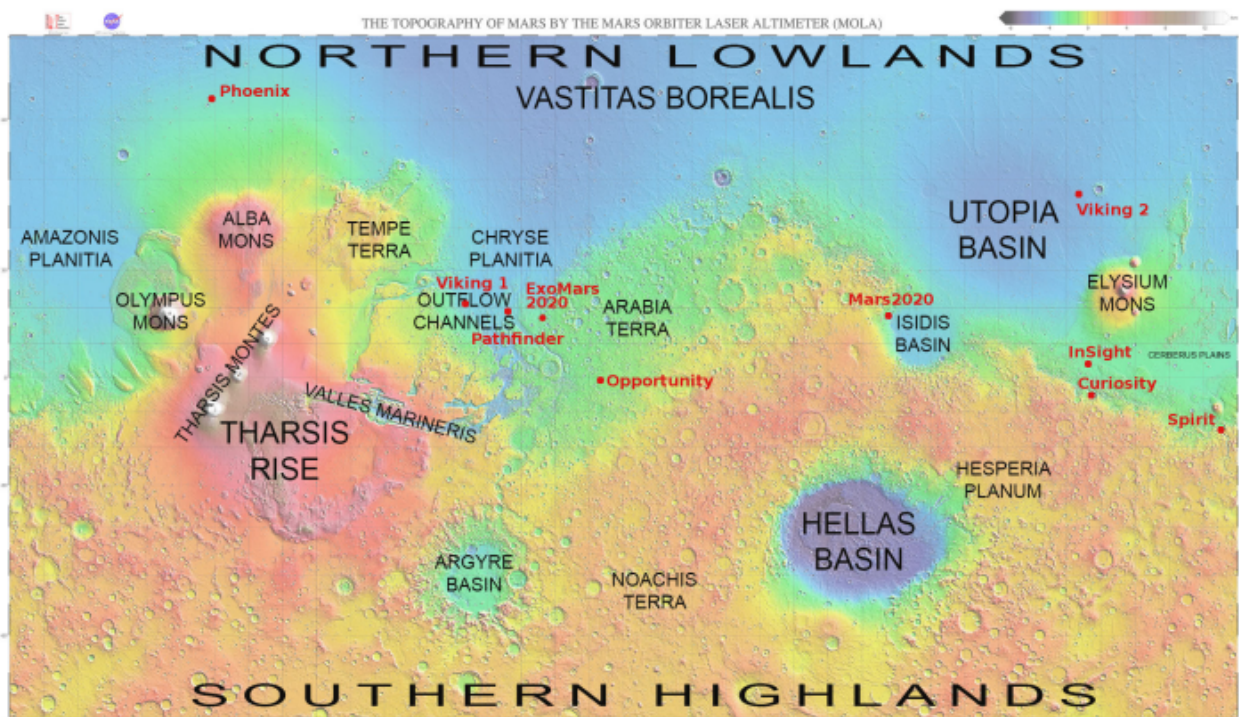


Figure 2.1 Topographic map of Mars with Mars missions landing sites (NASA/JPL)



A variety of computational modeling tools are used to carry out the scientific investigations in this study, ranging from one-dimensional column models to three-dimensional numerical atmospheric models. Depending on the specific application, the choice of which model to use is determined by whether the physics included in the model can sufficiently capture the phenomenon being studied, its ability to resolve scales of interest, the appropriateness of any simplifying assumptions, as well as the computational resources available. General Circulation Models (GCM) are effective at reproducing planetary-scale phenomena & synoptic-scale effects over long timescales of many years. However, covering a large parameter space means they typically lack the temporal and spatial resolution necessary to capture mesoscale phenomenon often associated with regional effects. In comparison to GCMs, mesoscale or limited region atmospheric models are applicable for simulating localized environments at high temporal and spatial resolution over periods of days to a few weeks. Terrestrial mesoscale models have been used to study atmospheric phenomena that have horizontal scales of 1 to 100 kilometers, including thunderstorms, mesoscale convective systems, extratropical cyclones, tropical cyclones, mountain waves, and sea breezes. Their ability to capture slope effects makes this class of models especially appropriate for our studies where topographically influenced wind regimes and tracer transport are important.

### **2.1.2 Structure of 3D Circulation Models**

The general structure of numerical atmospheric models typically consists of two main modules: the dynamical core and column physical models. The purpose of the dynamical

core is to integrate the governing equations of fluid dynamics such that given the present state, the modeled atmosphere steps forward in time using a sequence of small steps to predict a future state. General forms of the primitive equations are shown in Equation (2.1) through (2.4). These represent the primitive equations in their 'raw' form, before any simplifications or scaling arguments have been applied. This coupled set of equations representing the conservation of mass, heat, momentum, as well as any gaseous and aerosol species in the atmosphere forms the foundation of any numerical atmospheric model. Each individual expression includes any sources and sinks, and the set non-linear partial differential equations must be solved simultaneously.

$$\frac{\partial \rho}{\partial t} = -(\nabla \cdot \rho \vec{v}) \quad (2.1)$$

$$\frac{\partial \vec{v}}{\partial t} = -\vec{v} \cdot \nabla \vec{v} - \frac{1}{\rho} \nabla \rho - g \vec{k} - 2\vec{\Omega} \times \vec{v} \quad (2.2)$$

$$\frac{\partial \theta}{\partial t} = -\vec{v} \cdot \nabla \theta + S_{\theta} \quad (2.3)$$

$$\frac{\partial \chi_m}{\partial t} = -\vec{v} \cdot \nabla \chi_m + S_{\chi_m} \quad (2.4)$$

Symbol	Definition
$\vec{v}$	3D wind vector
$p$	pressure
$\rho$	density
$\theta$	potential temperature
$\chi_m$	gaseous & aerosol (tracer) species
$g$	gravitational acceleration on Mars (= 3.72 m/s)
$\vec{k}$	Vertical unit vector
$\vec{\Omega}$	Angular velocity
$S_{\theta}$	Source-sink term for $\theta$
$S_{\chi_m}$	Source-sink term for $\chi_m$

In addition to the dynamical core, three-dimensional numerical models consist of a number of parameterization schemes to represent physical processes that are too small to for the models to directly resolve. The ability to capture small-scale features in the atmosphere is important for the accuracy of model output since small-scale features can influence the larger-scale circulations through upscale growth (Thompson, 1957). However, a finite computational grid necessitates that there will always be structures too small to be resolved by the numerical model. For example, radiation transferred through the atmosphere occurs on the molecular scale, strongly influences the amount of radiation that reaches the ground and the resultant temperature at the surface. Formation of CO<sub>2</sub> and H<sub>2</sub>O ice cloud particles grow on sub-grid scales, yet the radiative impact of cloud development significantly affect temperatures on seasonal and climatic timescales. Thus, parameterization schemes are important not only because they strongly influence model forecasts of the predicted evolution of the atmosphere, but also as they interact with each other indirectly through their changes to the model variables. The details of the parameterization schemes specific to the models used in this dissertation will be discussed in sections 2.2.1 & 2.3.2.

## **2.2 NASA Ames General Circulation Model**

### **2.2.1 NASA Ames Mars General Circulation Model (MGCM)**

The NASA Ames Mars general circulation model, hence forth referred to simply as the Ames MGCM, is a 3-D finite-difference model supported and maintained by the Mars Climate Modeling Center at the NASA Ames Research Center. The model used in this dissertation

derives from the GCM\_2.3 version of the legacy code, which uses the Arakawa C-grid dynamical core based on Suarez & Takacs (1995). The vertical coordinate consists of 24 normalized pressure ( $\sigma$ ) layers. Near the surface, the vertical resolution is on the order of tens of meters, decreasing to approximately half of a scale height above 10 km. Surface properties such as thermal inertias are derived from THEMIS global nighttime mosaic (Putzig & Mellon, 2007), while albedos are based on the Mars Global Surveyor (MGS) Thermal Emission Spectrometer (TES) Mars Year 24 global bolometric albedo map with modifications to the north polar region poleward of  $60^\circ$  N by the Oregon State University modeling group (Tyler & Barnes, 2005). Topography is based on the  $1/16^{\text{th}}$  degree Mars Observer Laser Altimeter (MOLA) data (Smith et al., 1999) averaged to the model horizontal resolution of  $5^\circ$  (36 latitude bands) by  $6^\circ$  (60 longitude bands) using a 9-point weighted smoother.

For the water cycle, the model assumes that the surficial water ice deposits in the North Polar Residual Cap (NPRC) are the only source of atmospheric water. The distribution of ice is determined somewhat arbitrarily whenever the value of the grid-box averaged thermal inertia in the OSU maps exceed 550 SI units (Robert M. Haberle et al., 2019). Adsorption of water through the regolith and the cold trapping effect of the permanent  $\text{CO}_2$  ice South Polar Residual Cap (SPRC) have been ignored. As such, the SPRC does not act as a permanent sink like the real Martian atmosphere, and water vapor brought into contact with the SPRC does not become permanently removed from the system in the model. Even so, with virtually no tuning of the water cycle, the model shows reasonably good agreement with the present seasonal water cycle (Robert M. Haberle et al., 2019). Notably, simulations with

an equilibrated water cycle show no persistent clouds forming over the residual cap, seasonal variations in column vapor abundances are similar to those observed, the aphelion cloud belt has about the right opacity, and surface and air temperatures are in reasonably good agreement with observations (Robert M. Haberle et al., 2019). However, as will be discussed in chapter 3, the output of the specific Ames MGCM simulation used in this dissertation appears to be slightly too wet at certain seasons compared to observations, whereas later iterations of the Ames MGCM simulations referenced in Haberle et al. (2019) appear to be slightly too dry. For this dissertation, the NASA Ames MGCM simulations are used both as stand-alone studies of the Martian annual global water cycle, as well as input into the MRAMS mesoscale simulations as initial state and boundary conditions in the regional model.

Modeling the water cycle in the NASA Ames MGCM requires a number of physical packages to simulate the transport of water around the planet, the exchange of water between the surface and atmosphere, the microphysics of cloud formation and dissipation, as well as the radiative effects of clouds on diabatic heating rates. The radiation parameterization in the NASA Ames MGCM accounts for absorption and scattering from gaseous CO<sub>2</sub>, suspended dust, as well as trace amounts of H<sub>2</sub>O vapor in the atmosphere. Carbon dioxide, the main constituent in the Martian atmosphere, and water vapor are the only radiatively active gases in the model and their opacities are calculated from correlated-k distributions. The optical properties of radiatively-active dust and water ice clouds are determined based on their predicted effective particle size distribution and dust content in

their core. Visible & infrared fluxes are calculated using the two-stream solution to the radiative transfer equation (Toon et al., 1989) at each model layer boundary and at the surface, which are then converted to heating and cooling rates used to calculate the temperatures and the amount of solar energy absorbed by the surface. The radiative effects of CO<sub>2</sub>, H<sub>2</sub>O, and suspended dust are very important to the radiative heating of the atmosphere. Carbon dioxide strongly absorb energy at the 15 μm vibrational band while atmospheric dust is a strong thermal emitter near the 9 μm band. Latent heat changes due to the deposition and sublimation of CO<sub>2</sub> is also included as described in Murphy et al. (1995). The twelve spectral intervals incorporated into the model include 7 bands in the visible (0.24–4.5 μm) and 5 bands in the infrared (4.5–250 μm) (Robert M. Haberle et al., 2019) . Water and dust are strongly coupled in the MGCM, and both undergo exchanges between the surface and the atmosphere across the planetary boundary layer (PBL). In addition to model-resolved vertical winds, water, dust, and other tracers in the Martian atmosphere are vertically transported by turbulent eddy mixing and gravitational settling. The PBL scheme in the Ames MGCM is adapted from Haberle et al. (1999). Microphysical processes associated with the CO<sub>2</sub>, H<sub>2</sub>O, and dust cycles include the treatment of nucleation, growth, and sedimentation of CO<sub>2</sub> and H<sub>2</sub>O cloud particles, as well as interactive lifting & sedimentation of dust aerosols (Kahre et al., 2015; Kahre et al., 2006; Nelli et al., 2009). Water vapor interacts with airborne dust and can undergo heterogeneous nucleation onto the dust particles, while CO<sub>2</sub> cloud particles may nucleate on dust or water ice condensation nuclei. The full documentation other parameterizations included in the NASA Ames MGCM are referenced in (Robert M. Haberle et al., 2019).

## **2.3 The MRAMS Mesoscale Model**

### **2.3.1 MRAMS Heritage**

The Mars Regional Atmospheric Modeling System (MRAMS) is a non-hydrostatic, three-dimensional mesoscale model (Rafkin et al., 2001). This model descended from its terrestrial predecessor, the Regional Atmospheric Modeling System (RAMS) (Pielke et al., 1992; Tripoli & Cotton, 1980) with configurations appropriate for the Martian environment. MRAMS has capabilities for assessing water vapor and water ice transport in the lower atmosphere, making it ideal for our studies of the regional hydrological cycle on Mars. Previous scientific investigations using MRAMS include characterizations of boundary layer meteorology such as assessing near-surface air temperature and surface pressure cycles, local wind regimes, topographically forced circulations & atmosphere-surface interactions, studies of vertical water transport by mountain-Induced circulations (Michaels, 2006; Rafkin et al., 2002) as well as investigations of dust storms & aeolian processes (Rafkin et al., 2011). In addition to being a valuable tool for scientific investigations, MRAMS simulations are instrumental for engineering studies for landing site selection and characterization in support of a number of Mars missions including the Spirit and Opportunity Rovers, the Phoenix Mars Lander, the Curiosity Rover, the InSight Mars Lander, as well as ongoing efforts in preparation for the Mars 2020 Rover and other future missions (Rafkin & Michaels, 2003; Rafkin, Michaels, & Haberle, 2004; Michaels & Rafkin, 2009; Rafkin & Rothchild, 2011; Pla-Garcia et al., 2016; Rafkin et al., 2016). The general philosophy of using MRAMS and other mesoscale models in support of entry, descent, and landing (EDL) performance assessment

for surface-bound spacecrafts is to provide an envelope of scenarios at least three sigmas from the mean or most likely case.

## 2.3.2 MRAMS Model Specifics

### 2.3.2.1 MRAMS Dynamical Core

The governing equations in MRAMS are based upon the set of Reynolds-averaged primitive equations as shown in Eqs. 2.5 through 2.10. The model simulates atmospheric conditions including pressure, temperature, wind velocities, as well as tracers such as dust and water vapor abundances in any user-specified localized region of interest. Dependent variables predicted from conservation equations include  $\pi'$ ,  $u'$ ,  $v'$ ,  $w'$ ,  $\theta'$ , and  $r'$ .

$$\frac{D\pi'}{Dt} = \frac{c_s^2}{\rho_o \theta_o^2} \nabla \cdot \rho \vec{v} \theta_o \quad (2.5)$$

$$\frac{D\bar{u}}{Dt} = f\bar{v} - \theta \frac{\partial \pi'}{\partial x} + \nabla \cdot (K_m \nabla \bar{u}) \quad (2.6)$$

$$\frac{D\bar{v}}{Dt} = -f\bar{u} - \theta \frac{\partial \pi'}{\partial y} + \nabla \cdot (K_m \nabla \bar{v}) \quad (2.7)$$

$$\frac{D\bar{w}}{Dt} = -\bar{\theta} \frac{\partial \pi'}{\partial x} - g \frac{\theta'}{\theta_o} + \nabla \cdot (K_m \nabla \bar{w}) \quad (2.8)$$

$$\frac{D\bar{\theta}}{Dt} = \nabla \cdot (K_h \nabla \bar{\theta}) + \frac{\partial \bar{\theta}}{\partial t} |_{Diabatic} \quad (2.9)$$

$$\frac{D\bar{r}}{Dt} = \nabla \cdot (K_h \nabla \bar{r}) + \frac{\partial \bar{r}}{\partial t} |_{Source/Sink} \quad (2.10)$$



<b>Symbol</b>	<b>Definition</b>
$\pi = \frac{c_p T}{\theta}$	Exner function
$u$	East-west wind component
$v$	North-south wind component
$w$	Vertical wind component
$\theta$	Potential temperature
$r$	Gaseous & aerosol (Tracer) species
$c$	Speed of sound
$f$	Coriolis parameter
$K_m$	mixing coefficients for momentum
$K_h$	mixing coefficients for heat

All variables in the primitive equations are grid-volume averaged quantities. The variables are decomposed into 3 parts: a base state ( $\phi_o$ ), a model resolved perturbation from the base state ( $\phi'$ ), and an unresolved sub-grid scale term ( $\phi''$ ) (Eq. 2.11, 2.12). The base state is assumed to be hydrostatic and dynamically balanced, while the perturbation and the sub-grid scale terms are non-hydrostatic. At typical mesoscale grid spacing, the unresolved fluctuating component is assumed to be turbulence, modeled via eddy diffusivity terms and subject to closure using various turbulence scaling, laws, and empiricism.

$$\phi = \phi_o + \phi' + \phi'' \quad (2.11)$$

$$\bar{\phi} = \phi_o + \phi' \quad (2.12)$$

Due to the huge diabatic heating for Mars, a compressional heating term is added to the pressure equation (Eq. 2.5) in MRAMS. Nicholls & Pielke (1994; 2000) showed that neglect of this term results in a very poor representation of the thermal tide pressure signal.

No anelastic assumption is made in the mass continuity equation. Thus, compressibility is allowed in the atmosphere. Pressure gradient is expressed in terms of the Exner function  $\pi'$ , which simplifies the equations and makes computation of pressure gradients more numerically stable since gradients are smaller. An acoustic adjustment is included due to the  $\pi'$  tendency term, since acoustic waves are a solution to set of equations. The dynamics are split using an implicit acoustic solver so that acoustic modes are solved on a smaller time step while the longer modes are held constant. Equations (2.6) through (2.8) governs the conservation of momentum. Both the advection term & rotational effects are retained in the zonal & meridional (horizontal) equations of motion. However, the rotational term is dropped from the vertical equation of motion. The thermodynamics equation (Eq. 2.9) includes both thermal dissipation (via molecular motion) and diabatic heating. Potential temperature  $\theta$  is used as the prognostic variable in the heat conservation equation, as it is conserved for adiabatic processes. However, diabatic heating is present in MRAMS through radiative forcing, surface-atmosphere heat exchange, latent heating, cloud microphysical processes, as well as unresolved dynamics such as friction, boundary layer mixing, and wave breaking that are handled by the specific physical parameterization schemes used. Finally, equation (2.10) governs the conservation of dust, water, and other trace species. MRAMS can track the behavior of any number of individual tracers, bounded by computational capabilities, that the user may initialize heterogeneously in space. In addition to thermal dissipation, sources and sinks can be defined to represent tracer deposition and chemical processes.

### 2.3.2.2 MRAMS Physical Parameterizations

The radiative transfer algorithm in MRAMS closely resembles that used in the NASA Ames MGCM (refer to section 2.2.1), which includes the radiative effects of CO<sub>2</sub>, suspended dust, water vapor, and water ice clouds at visible and thermal infrared wavelengths. Radiative heating is based on a two-stream correlated-k parameterization (Toon et al., 1989), with dust optical properties given by Wolff et al. (2006). Turbulent mixing in MRAMS is parameterized, and the current version of MRAMS (2.9\_r37) includes nine subgrid-scale turbulence parameterization options (Rafkin & Michaels, 2019). The turbulent flux of scalars is expressed by multiplying the eddy diffusion coefficient, which varies in space and time, by the gradient of the quantity being transported. The turbulent tendency to the resolved scalars is given by the flux convergence of the Reynolds stress. Several of the schemes are high-order closures which prognose turbulent kinetic energy (TKE) and then use TKE to determine the mixing coefficients (Deardorff, 1972; Mellor & Yamada, 1982), while other schemes are lower order closures based upon the local strain and deformation (Smagorinsky, 1963). The subgrid-scale diffusion parameterization used in this dissertation are of the higher order turbulent closure schemes which calculate turbulent eddy viscosities (K factors) based on the level 2.5 turbulent scheme formulated by Mellor & Yamada (1982). The surface layer model couples the atmospheric surface layer with the regolith surface. The surface layer includes a prognostic conductive regolith model that includes carbon dioxide deposition and sublimation. Ice stability is governed by an energy balance model separate from the fluxes diagnosed from the surface layer model. For the subsurface, a separate

regolith model computes the subsurface properties and uses the atmospheric surface layer sensible heat flux as one of the inputs.

One of the key processes modeled in this research is the microphysical representation of water and dust. The microphysics parameterization in MRAMS is based on the Community Aerosol and Radiation *Model* for Atmospheres (CARMA) microphysical model (Toon et al., 1988). Dust in MRAMS is initialized following a standard Conrath-v prescription. Once initialized, dust, water ice, and CO<sub>2</sub> ice particles can be advected, diffused, sedimented. Dust aerosols can further be scavenged by water or CO<sub>2</sub> ice particles through the process of cloud condensation. While the Ames MGCM uses a moment scheme in its microphysical parameterization, CARMA uses bins to represent the particle sizes of dust, H<sub>2</sub>O ice, and CO<sub>2</sub> ice particles. Fully active dust, water vapor, and water ice microphysics are enabled in the aerosol code. The Martian hydrological cycle is intimately coupled to the dust cycle as dust particles are required as cloud condensation nuclei. Dust particles are tracked as cores within water ice condensates. Dust is liberated when water ice completely sublimates. Water vapor in MRAMS is always radiatively active when present. For our simulation, both dust and water ice are radiatively active in the radiative transfer calculations, and the advection, diffusion, nucleation, sedimentation, and precipitation of aerosols is enabled. Semi-empirical Mars dust is specified based on Wolff et al. (2006). Dust variables are separated into 8 different size or mass bins. The minimum particle radius starts at  $5.0 \times 10^{-2} \mu\text{m}$ , and the ratio of particle mass between successive bins is set to 7.2. The foreground atmospheric dust is initialized using a prescription as a function of latitude and  $L_s$  based on zonally-averaged TES Mars Year 24 extinction optical depth and an empirical raster haze top field derived from

SPICAM observations. The visible wavelength extinction dust column opacity at 9  $\mu\text{m}$  is set to 0.45 at a reference pressure of 610 Pa. The vertical distribution of dust is specified by a Conrath-nu parameter of 0.03. Suspended dust aerosols can have significant radiative effects on the temperature structure of the atmosphere. Water ice aerosols are separated into 10 size or mass bins, with a minimum particle radius of  $7.21 \times 10^{-2} \mu\text{m}$ . Similar to the dust bins, the ratio of particle mass between successive water ice aerosol bins is 7.2.

#### 2.3.2.3 MRAMS Initialization and Boundary Conditions

The MRAMS computational grids used in this research are Arakawa C-type projected onto an oblique polar stereographic map projection. Grid spacing is constant in linear distance, but not regularly spaced in latitude and longitude. The pole point of the projection is specified by the user to generally lies close to the center of the modeled domain, and does not need to coincide with the geographic pole. Two-way nested grids, where interactive updates to the state variables are sent from the parent grid to the daughter grid and back, are embedded inside the near-global scale mother domain such that computational power can be concentrated at progressively higher-resolution regions of interest.

MRAMS require initial and time-dependent boundary conditions for the during of the simulation. Initial conditions in the MRAMS simulations are user specified and variable in 3-dimensions. Temperature, pressure, winds, and advected tracers such as water are ingested into the mesoscale model on all domains based on the output from a previously Ames MGCM simulation. The initial state is specified on the finest MRAMS grid first, and on the coarsest grid last. In regions where the parent grid domain overlaps with the daughter grid domain,

those grid points on the parent grid are replaced by the higher resolution values that was previously initialized on the daughter grid. Thus, grid-1 will contain higher resolution information from the grid-2 initialization, which will contain information from the grid-3 initialization, etcetera. The gridded data from the MGCM are horizontally interpolated to the MRAMS polar stereographic projection via a bilinear interpolation scheme. The vertical initialization involves a linear interpolation of the MGCM data, which is on sigma-pressure surfaces, onto the MRAMS vertical grid, which is based on the terrain-following sigma-z coordinate. Given the higher resolution of MRAMS, topography in MRAMS is locally higher or lower than that in the MGCM. The initial atmospheric state within features that cannot be resolved by the Ames MGCM, such as Gale Crater and Valles Marineris, are done by linearly extrapolating the values from the lowest two levels of the MGCM onto the MRAMS levels all the way down to the MRAMS lower boundary. Time-dependent GCM-derived boundary conditions are updated every 1.5 Martian hours during the mesoscale simulation, where the model solution at the lateral boundaries as well as the model top are nudged towards the gridded analysis file. The four outermost grid points on the mother domain have been specified as the nudging region for the simulations performed in this study. The lower boundary of the model is governed by the topography and surface thermophysical properties. Topography is specified from standard latitude-longitude gridded data products from the Mars Orbiter Laser Altimeter (MOLA). The MOLA global topography maps used range from a resolution of 32 pixels per degree in the outermost grids, to 128 pixels per degree map in the finest grids. Topographical shadowing is enabled on all MRAMS grids. Thermal inertia on all grids is ingested from the THEMIS-derived global nighttime mosaic

(Putzig & Mellon, 2007), while the albedo is based on the Mars Global Surveyor (MGS) Thermal Emission Spectrometer (TES) Mars Year 24 global bolometric albedo map.

### **2.3.3 MRAMS Validation**

Mesoscale model validation is particularly challenging in the absence of adequate observational data. MRAMS has previously been validated at the Mars Pathfinder and Viking Landers 1 & 2 sites (Rafkin et al., 2001), and the model results at the Mars Exploration Rover (MER) landing sites are consistent with the environment encountered by the spacecraft during entry, descent and landing (Kass et al., 2003; Rafkin & Michaels, 2003). Most recently, an extensive model validation exercise was conducted with the data returned from the Rover Environmental Monitoring Station (Gómez-Elvira et al., 2012) onboard the Curiosity Rover. MRAMS has been shown to reproduce the observational data from the Rover Environmental Monitoring Station (REMS) within the range of the observational uncertainty (Pla-Garcia et al., 2016; Rafkin et al., 2016). In regions of complex topography such as Gale Crater, the ability of the model to match the Curiosity Rover's observations suggests that there is justifiable confidence that MRAMS is capable of capturing the concomitant complex circulations in other areas of complex terrain on Mars.

## **CHAPTER 3**

### **IMPLICATIONS OF FOG IN VALLES MARINERIS**

#### **3.1 Introduction**

Water-ice fogs on Mars have previously been observed in low-elevation regions such as Noctis Labyrinthus, Valles Marineris, and Hellas Basin, as well as in the north polar region (French et al., 1981; Hess et al., 1976; Kahn, 1984; Moores et al., 2011; Neumann et al., 2003). Low-level clouds, first observed as morning limb brightening in Viking Orbiter images that persisted for several hours after sunrise, were presumed to be fed by water ice particles condensing onto the surface at night and later released into the atmosphere during the morning which subsequently condensed in the cooler air above the low-level inversion layer (Hess et al., 1976). These near-surface condensate clouds were strongly modulated by the diurnal variation of the near-surface atmospheric temperature (Nelli et al., 2010). While water-ice clouds in the polar region have been directly detected using the in-situ instruments such as the Lidar onboard the Phoenix Mars Lander (Moores et al., 2011; Tamppari et al., 2010; Whiteway et al., 2009), fog and low-lying clouds in the near-equatorial canyons and in Hellas Basin have only been characterized from orbit. Fog observations are particularly challenging for sun synchronous spacecrafts which typically image the Martian surface in the mid-afternoon, as warmer daytime temperatures and lower relative humidity indicate that the presence of fogs might be expected to be at a minimum. Water-ice fog occurrences at other local times have been reported by the Mars Express (MEX) orbiter, which is in an elliptical orbit that enables observations with varying local time coverage. A particularly



interesting image of potential early morning water-ice fog taken by the High-Resolution Stereo Camera (HRSC) at 09:20 local time during southern fall ( $L_s=38^\circ$ ) shows atmospheric aerosols that are evidently-confined to low elevations within the walls of the canyon system (Fig. 3.1). While the aforementioned HRSC image has been often cited as a prime example of water-ice fog in Valles Marineris, there is still ongoing debate regarding the exact composition of the obscuration. Near-simultaneous spectral observations from the Planetary Fourier Spectrometer (PFS) and the Observatoire pour la Mineralogie, l'Eau, les Glaces et l'Activite (OMEGA) instrument collected around the same time as the HRSC image provided an opportunity to probe at the composition spectrally. Möhlmann et al. (2009)'s analysis using PFS data detected a water ice signature in the  $750\text{--}900\text{ cm}^{-1}$  range. PFS spectra were taken both inside and outside the canyon, and the  $1.5\text{ }\mu\text{m}$  band water-ice signature was present only inside the canyon. Meanwhile, Inada et al. (2008)'s analysis of OMEGA spectra showed that the same aerosol obscuration in the HRSC image was primarily composed of dust particulates, with optical depth of  $\sim 1.7$  to  $2.3$  at a wavelength of  $0.675\text{ }\mu\text{m}$ . Relative band depths of the  $\text{H}_2\text{O}$  ice absorption band at  $1.50\text{ }\mu\text{m}$  were  $< 2\%$  during orbits 438 and 482 (Inada et al., 2008). While OMEGA spectra interpreted the aerosol layer in Valles Marineris to be primarily comprised of dust, Inada et al.'s results did not exclude the occurrence of water ice, but any presence of water would have fallen below their detection limit.

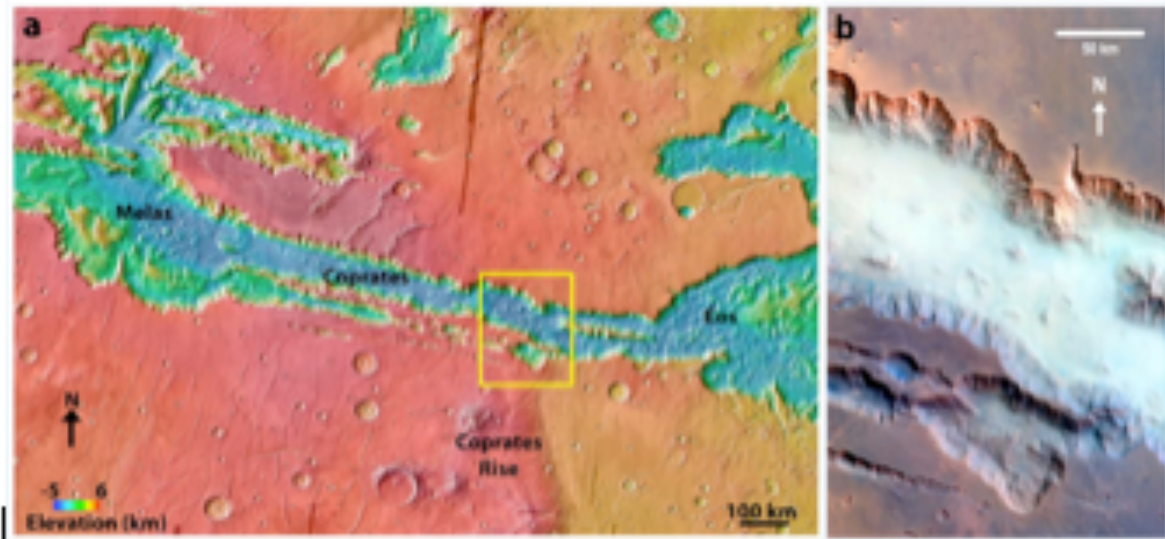


Figure 3.1 Image of potential morning ice fog in Valles Marineris. (a) Mars Orbiter Laser Altimeter (MOLA) topography of central Valles Marineris. (b) Potential morning ice fog in a low altitude aerosol layer imaged by the Mars Express High Resolution Stereo Camera (HRSC) in the Coprates Chasma region of Valles Marineris at 09:20 local time at  $L_s = 38^\circ$ . (Möhlmann et al., 2009's reproduction of HRSC image ID H0438\_0000\_ND4). The yellow box approximately outlines the region shown in panel b.

Regardless of the exact composition or the ratios of dust to water within the canyon, the presence of any water ice clouds at all inside Valles Marineris, even if dust makes up the vast majority of the observed aerosols, implies saturation conditions within the canyon. At the same time, the aerosol-free regions outside the canyon do not appear to be cloudy or even very dusty at all. This scenario is particularly interesting because it implies that the local atmospheric environment at the lower boundary layer can be vastly different inside the canyon than outside. For clouds to form in Valles Marineris when the environment outside the chasma appear cloud-free, temperatures must be cooler inside the canyon compared to the regions immediately outside the canyon if water concentrations are the same, or otherwise the water mixing ratio must be concentrated within the canyon system for similar

temperature structures inside and out. In situ atmospheric measurements of the lower planetary boundary layer on Mars have been limited to the few locations where landed spacecrafts have explored. The scenario where water ice clouds forms inside the canyon but not immediately outside is especially intriguing because water vapor mixing ratios are typically assumed to be uniformly well-mixed below the saturation level.

Motivated by the apparent presence of water ice clouds strictly inside Valles Marineris and the lack of thick clouds on the surrounding plateaus, we use numerical modeling techniques to provide regional context for the water cycle within Valles Marineris and the surrounding plateau. In this study, we evaluate the possible scenarios conducive to the formation of water ice fog inside the Valles Marineris canyon system. By investigating the radiative and dynamical environments in the vicinity of Valles Marineris, we examine the possible structure of the low-lying water ice clouds and their implications on the variability in local water abundances in the lower atmosphere. Section 2 of this chapter describes the atmospheric model setup and an overview of the global and regional water cycle at the season of interest in order to place the water abundances in Valles Marineris in the context of the larger scale water cycle. Mesoscale modeling results are presented in section 3 including an assessment of the thermal structure and water concentrations inside Valles Marineris and on the plateau. Section 4 discusses of the implication of water ice fogs on the regional radiative and dynamical forcing in Valles Marineris, and conclusions from this chapter are summarized in Section 5.

## **3.2 Method**

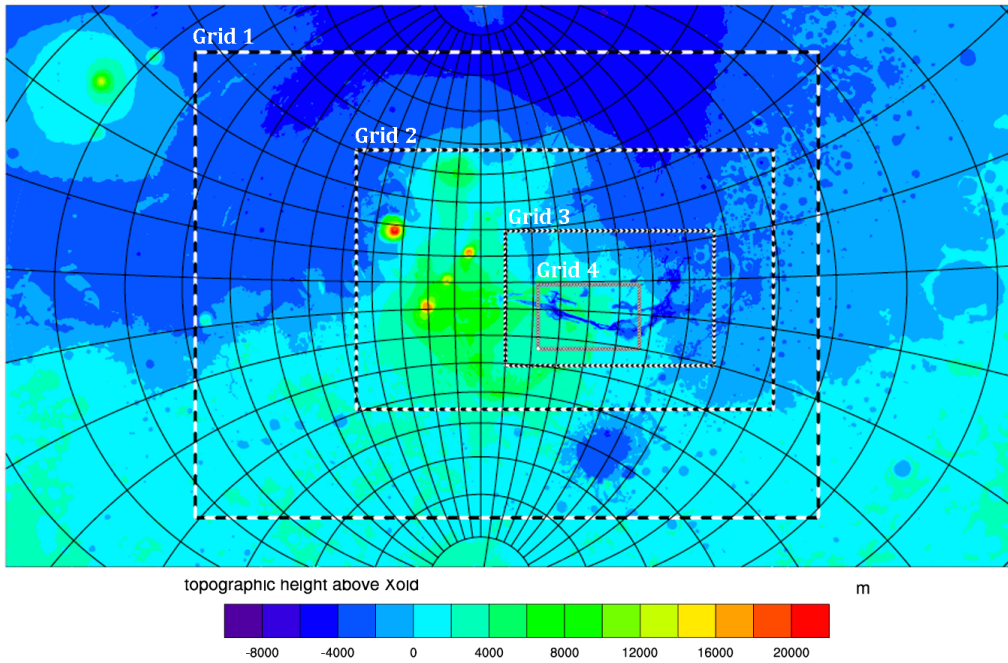
In situ meteorological measurements in the lower atmosphere within a topographically complicated location such as Valles Marineris are not readily available from current spacecraft observations, thus mesoscale atmospheric modeling provides an excellent opportunity to evaluate the diurnal variability in thermal and dynamical conditions in the canyon as well as the structure of any water ice fogs that may be present. For this study, the Mars Regional Atmospheric Modeling System (MRAMS) mesoscale atmospheric model (Rafkin et al., 2001) is used to simulate the circulations of the Martian atmosphere at regional scales. The usage of a limited area regional model ensures that topographic slopes are well resolved compared to the typical resolutions of a global-coverage general circulation model. The effects of shadowing and slope angle geometries on the energy budget are also taken into account, given surface radiative forcing based on topographic slope and shadowing effects is especially important in the complex terrain of the Valles Marineris region.

### **3.2.1 Grid Configuration**

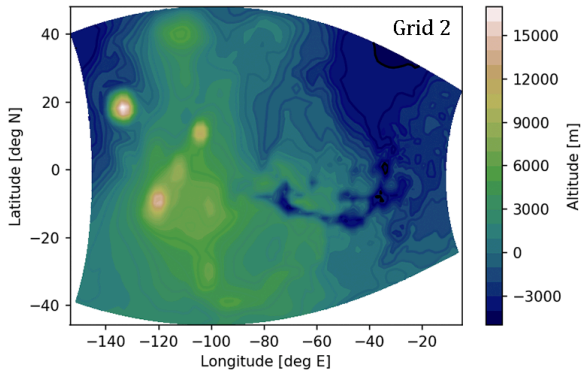
The mesoscale model configuration optimized for our simulations uses 4 two-way nested grids whereby progressively higher-resolution grids are embedded into a parent grid (Fig. 3.2). The grid-2 model domain fully encompasses Tharsis Montes and Valles Marineris, while the innermost grid (grid-4) focuses in on the canyon itself. The model grids are based on oblique polar stereographic map projections with a pole point located at 2.0° latitude and

-100.0°E longitude. The grid spacing between adjacent grid points is 240 km on the mother domain, while grid spacing on grid-4 reduces to 20 km near the center of the 74 x 116 grid points domain. The mesoscale simulations include 60 vertical atmospheric layers, with the bottom-most atmospheric layer midpoint at a level of  $\sigma_z=7.3$  meters above ground, and a model top at 50.7 km. A vertical grid stretch ratio of 1.12 is applied between z-levels for the lowest 46 atmospheric layers. The vertical grid spacing between the two lowest atmospheric layers is 15.9 m, gradually stretching to a constant maximum spacing of 2250 meters between adjacent layers above an altitude of 22 km. The bulk of the ~7 km deep Valles Marineris canyon system is captured by ~35 vertical layers, sufficient for resolving the circulation and thermal structure within the canyon.

**A**



**B**



**C**

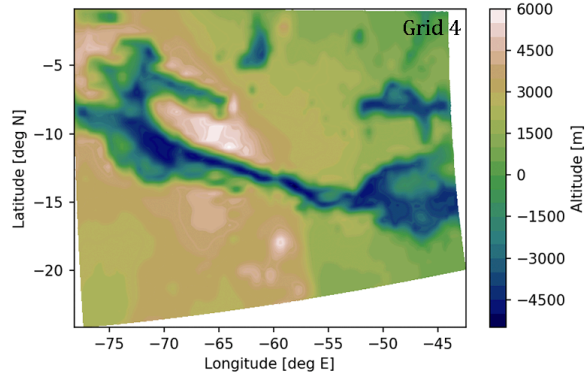


Figure 3.2 MRAMS Model Configuration.

(a) Numerical model domain boundaries shown as black and white boxes for the 4 two-way nested grids used in the mesoscale simulation. Each alternating black and white bar represents the model grid spacing on that grid. (b) Topography of the grid 2 model domain in latitude and longitude space.

(c) Topography of the grid 4 model domain.

### 3.2.2 Initialization & Boundary Conditions

The initial atmospheric state in MRAMS is taken from the output of a NASA Ames Mars General Circulation Model (MGCM) simulation that has reached climate equilibrium (Haberle et al., 2019). Temperature, pressure, winds, and water is applied on each grid by linearly interpolating the MGCM data onto the MRAMS grid points. Lateral boundary nudging on all grids is performed on the outermost 4 grid points of each of the grid domain boundaries, at a nudging time scale of 5548.4 seconds. Nudging at the top of the domain is performed above a geopotential height of 40 km. A more detailed description of the model initialization is described in Section 2.3.2.3. The MRAMS simulation is run with a constant dynamical timestep of 8 seconds on the coarsest grid. The number of timesteps at each daughter grid is double that the number of timesteps on its parent grid. The total simulation time for this experiment is 10 sols.

Special attention is paid to the water ingestion in this study since the global-scale model does not resolve the depths of the canyon in Valles Marineris. Profiles of water (and other state variables) are extrapolated down into the canyon in MRAMS by linearly extrapolating the values at the two lowest MGCM atmospheric levels. Given the depth of the canyon is ~7km beneath the adjacent plateau, a linear extrapolation down to the canyon floor can result in a significant amount of water placed at the lowest grid level in MRAMS. However, as there is no meteorological measurement inside Valles Marineris, the actual amount of water at the bottom of the canyon remains currently unknown. Near the beginning of the simulation, the column vapor abundance in Valles Marineris modeled by MRAMS is found to be higher compared to that at the nearest MGCM grid-point as well as the location

of the nearest binned TES data, likely as a consequence of the deeper total column inside the canyon that can be resolved by MRAMS. After approximately 5 sols into the simulation, the total water in the column adjusts to an equilibrated state and the diurnal fluctuation in the amount of total water stabilizes as shown in the time series of total column water (Fig. 3.3). A comparison of the total water column in the canyon versus that above the plateau shows that the total water above the plateau does not require nearly as long to equilibrate. This is a direct a consequence of the discussion above. Whereas a higher quantity of extraneous water may be artificially emplaced inside the canyon, the quantity of water initialized on the plateau more closely resembles that in the lowest levels of the MGCM. Accounting for the stability of water in the model, the initial 5 sols of this simulation are considered as spin-up, and the diurnal average of only the last 5 sols in the experiment are used for analysis.

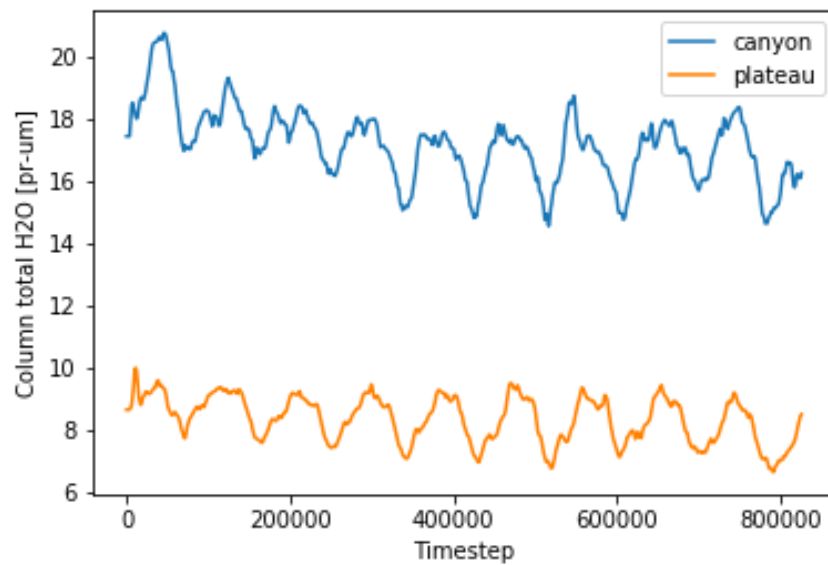


Figure 3.3 Time series of the total column water in the canyon and above the plateau over the duration of the 10-sol simulation. The decrease in column water over the first 5 sols is indicative of the spin-up required for water to equilibrate in the MRAMS simulation.



### **3.2.3 Global Water Cycle at $L_s=38^\circ$**

Water vapor is ingested into the mesoscale model on all domains based on output from the Ames MGCM. Zonally-averaged water vapor column from the MGCM as a function of season and latitude is compared to Thermal Emission Spectrometer (TES) & Viking Mars Atmospheric Water Detector (MAWD) observations from Mars Year 24, an annual cycle that is typically used as a canonical standard for the typical Martian atmosphere (Fig. 3.4). Repeatable inter-annual patterns such as high vapor abundances at high latitudes in the summer hemisphere is reflected in both TES water vapor retrievals and the MGCM results.

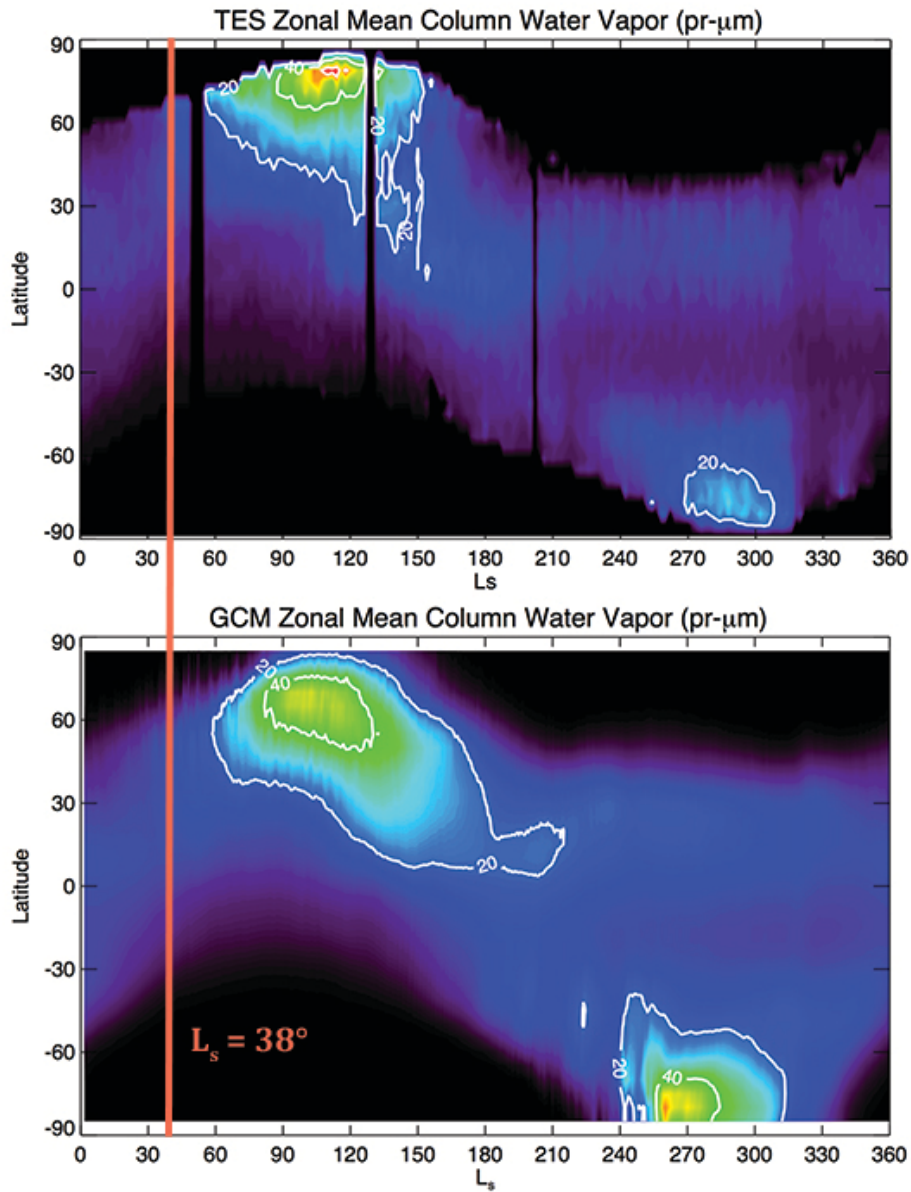


Figure 3.4 Column vapor abundances in TES and the Ames MGCM.  
 The season of interest for this study is at  $L_s \sim 38^\circ$ .  
 (Kahre, personal communication)

The annual global water cycle on Mars is governed primarily by the deposition of water ice onto the winter polar cap, sublimation of the seasonal ice deposits during spring,

and the cross-equatorial exchange of water between the northern and southern hemispheres (Houben et al., 1997). As described in section 1.2, the main source of water in the Martian atmosphere comes from sublimation of the north pole during northern spring. Figure 3.5 shows the global projection of total column water, column water vapor, and column water ice at our season of interest ( $L_s=38^\circ$ ). The mean meridional circulation dominates the forcing of water to lower latitudes and dictates the global concentration of water during this time of year. A moist tongue of vapor emerges from the northern polar region as warm daytime temperatures sublimate the edges of the polar ice caps. This moisture travels towards the northern mid-latitudes to bring about an easterly moist front to transport higher concentrations of water vapor towards the eastern end of Valles Marineris. The overall distribution of the total water column show little variability over the diurnal cycle as the distribution of water in the column is determined primarily by the Hadley circulation. However, water vapor and water ice mixing ratios in the planetary boundary layer closest to the surface show a clear night side versus dayside contrast. The concentration of water vapor in the lowest atmospheric level night side of Mars appears to be much wetter as water ice sublimates into water vapor on the warmer dayside, and water vapor condenses back into water ice in the night side in the lowest scale height of the atmosphere.

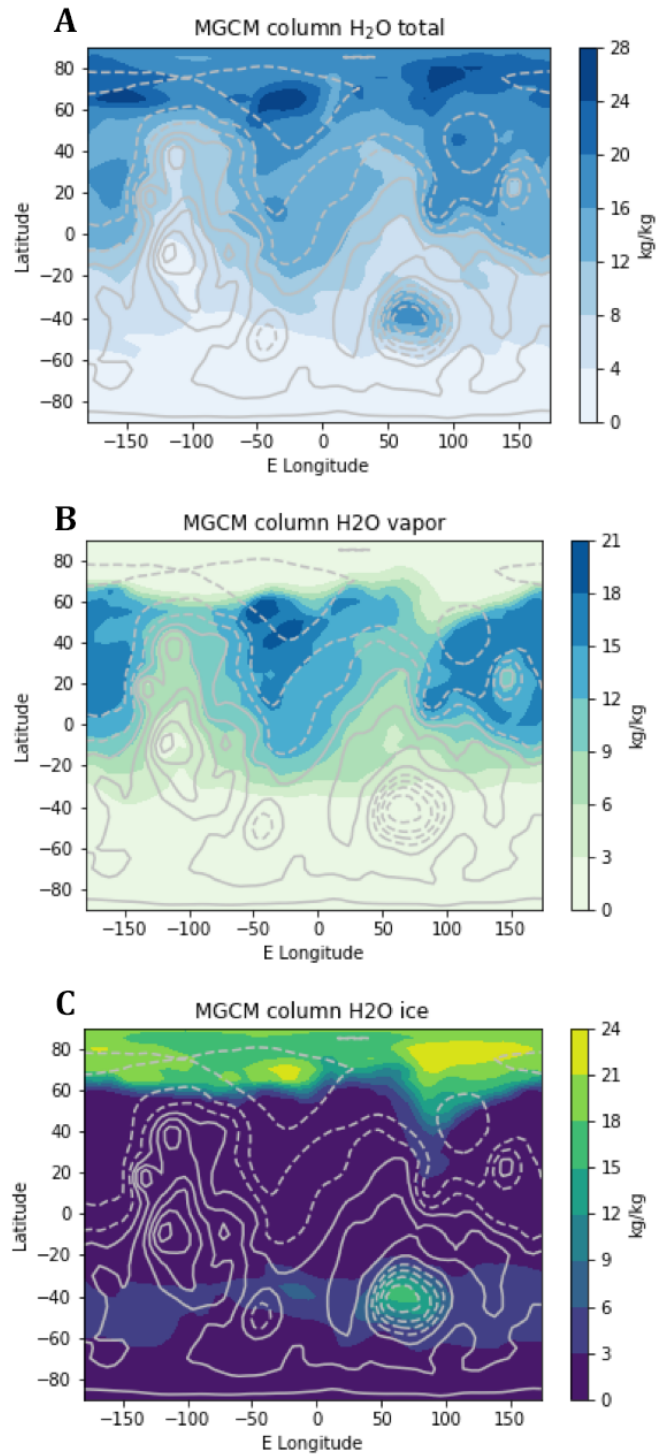


Figure 3.5 Simulation results of water from the Ames Mars GCM at  $L_s = 40^\circ$ .  
 (a) Global map of total water in the column, (b) water vapor in the column, and (c) water ice in the column.

### **3.2.4 Regional Water Cycle at Ls=38°**

MRAMS modeling results from grid 2 show similarities between modeled water ice cloud optical depths and the locations of water ice clouds identified in the Mars Orbiter Camera (MOC) global mosaics (Fig. 3.6). The regional transport mechanisms of water in the Tharsis plateau and Valles Marineris regions can also be characterized using mesoscale modeling results. In contrast to the moisture brought southward from the northern polar region, a southerly dry front sweeps cross-canyon resulting in a larger diurnal swing of water vapor inside the canyon than on the plateaus (Fig. 3.7). The simulated wind structure produces a strong cyclonic flow northeast of the Tharsis – Valles Marineris region.

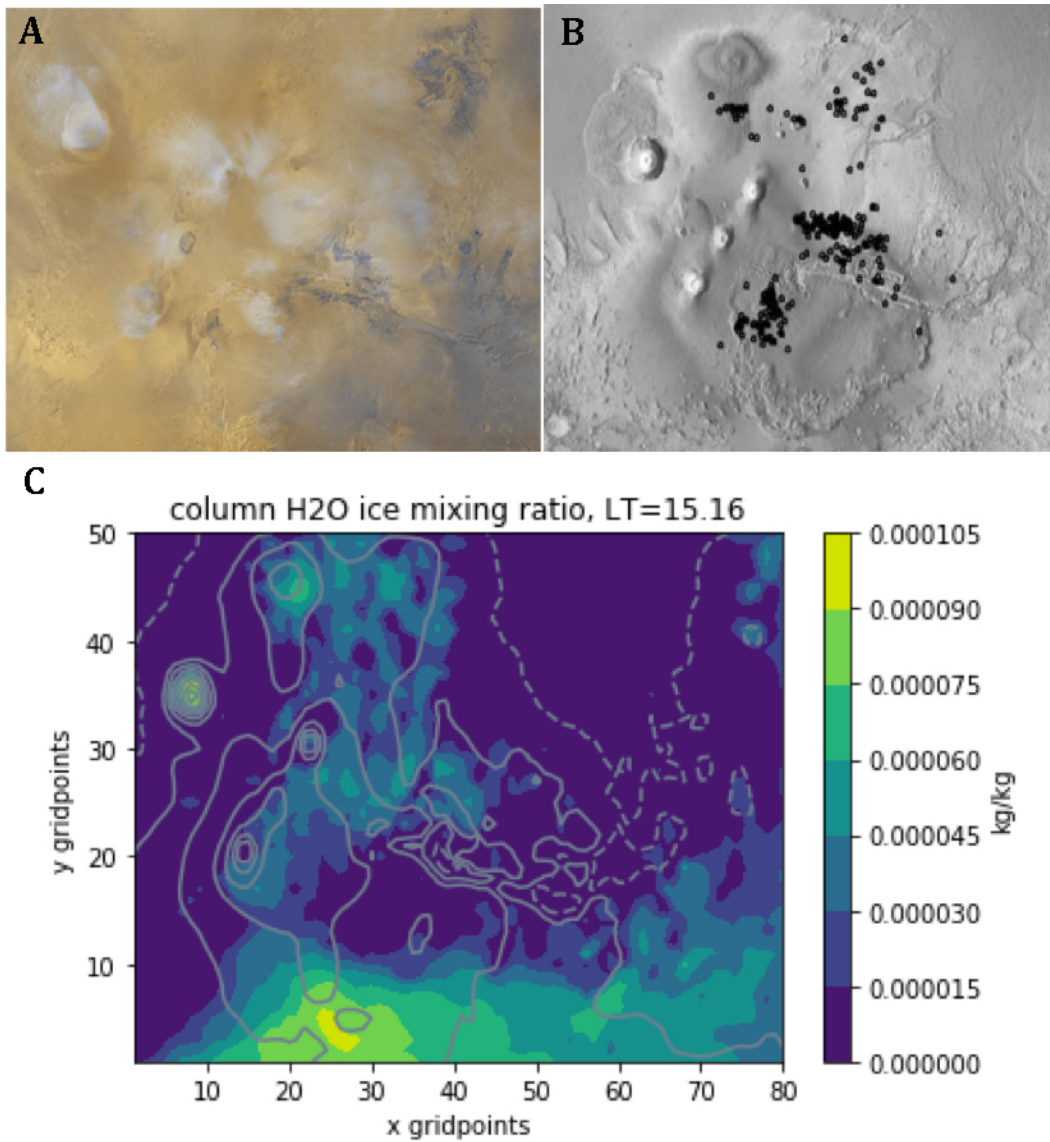


Figure 3.6 MOC cloud observation versus water ice clouds in MRAMS  
 (a) MGS MOC2-144 global mosaic showing typical afternoon clouds. (b) Benson et al. (2003) Cloud center locations between  $L_s = 0^\circ\text{--}90^\circ$  (c) Simulated water ice cloud optical depth in the Tharsis & Valles Marineris region in grid-2 (Refer to figure 3.2b).

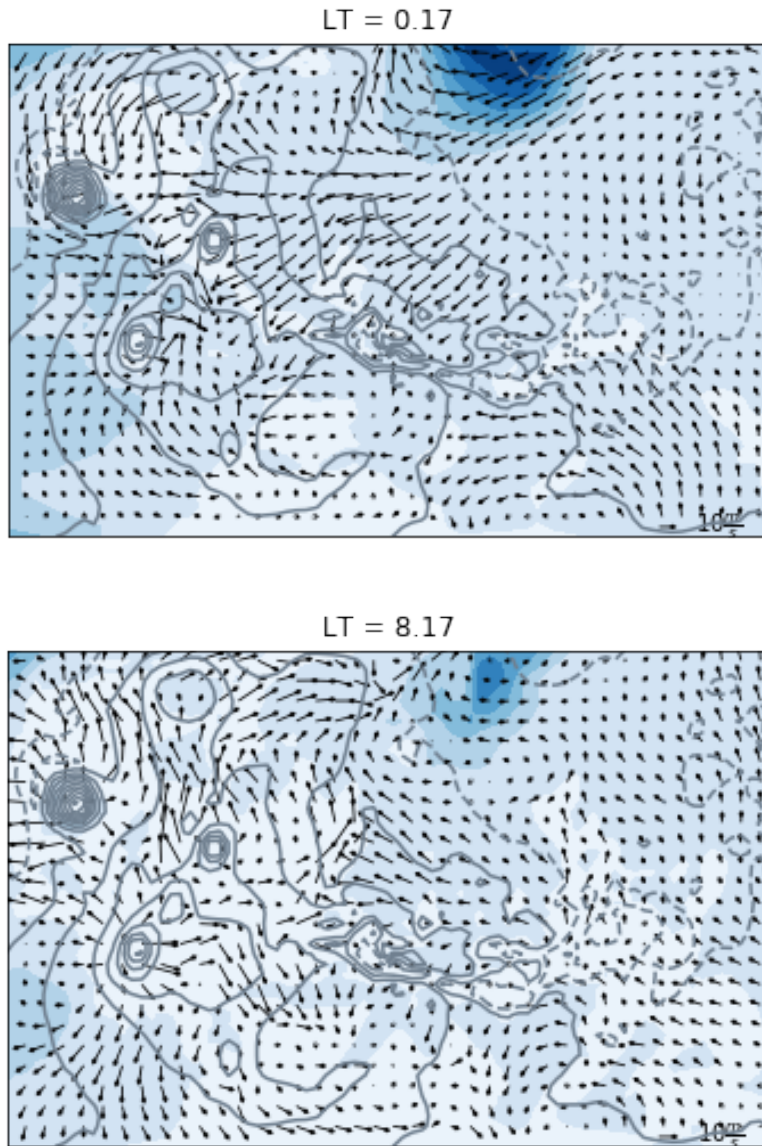


Figure 3.7 Low-level circulation of water vapor on the grid-2 domain.

The regional atmospheric circulation on Mars is highly influenced by local topographic gradients, and the importance of topography on Mars' regional and local circulations has been suspected for some time. Ye et al. (1990) theorized that slope circulations would be substantially stronger on Mars. Even small topographic features can



substantially affect the nominal atmospheric circulation through mechanical blocking. Rafkin et al. (2001) further showed that radiative forcing, as well as direct mechanical topographic influence play an important role in the mesoscale circulation. Terrain-following air parcels forced along the slopes of the major volcanoes in Tharsis Montes and the steep canyon walls of Valles Marineris can significantly impact the local water vapor concentration and the associated conditions for cloud formation. Figure 3.8 illustrates the transport of moisture along the flanks of the major Tharsis volcanoes and structure of clouds aloft directly above the plateau.

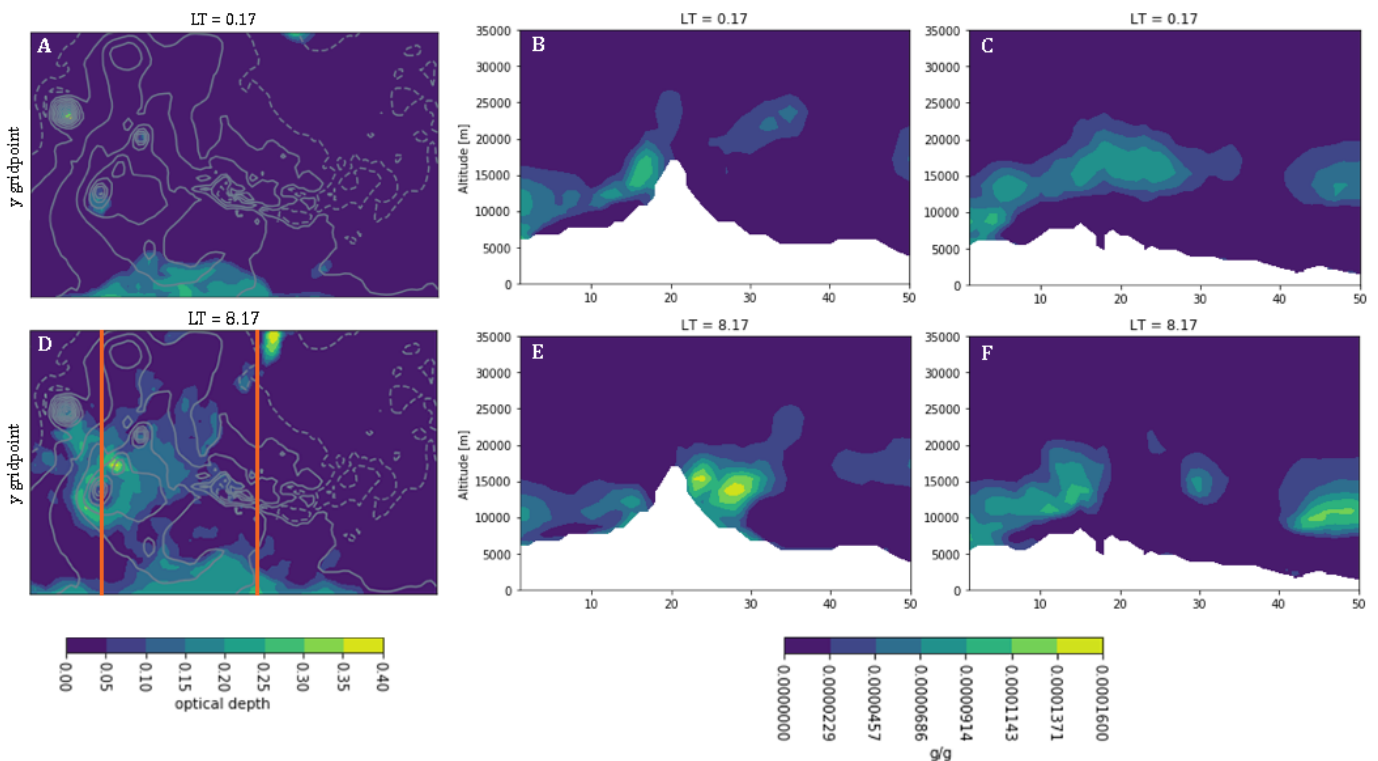


Figure 3.8 Diurnal variations of H<sub>2</sub>O ice mixing ratio at 0.17 LT and 8.17 LT on the grid 2 model domain (a & d) Nadir View, (b & e) cross-sections over Arsia Mons, (c & f) cross-section above Valles Marineris and the surrounding plateau. The locations of the cross-sections are denoted by the two red lines in panel d.



## **3.3 Results**

### **3.3.1 Simulation Results**

Mesoscale modeling results on the innermost grid-4 domain centered on Valles Marineris and the plateau immediately adjacent to the canyon show widespread water ice cloud formation throughout the Valles Marineris region, both inside the chasma and above the plateaus during the early morning (Fig. 3.9). This is inconsistent with spacecraft observations such as the example shown in figure 3.1 which reveals a high-opacity obscuration inside the canyon only while widespread clouds are absent above the plateau.

Formation of water ice fogs require either the air temperature to dropping to the dew point, or that water vapor is added until saturation is reached. Thus, if the modeled temperature structures are representative of reality and if clouds are present and confined within the canyon, higher temperatures inside the canyon necessitate a higher concentration of water in the canyon than outside the canyon due to the exponential dependence of saturation vapor pressure on temperature. Conversely above the plateau, the model shows that clouds are wide-spread whereas the observations do not. This signifies that the model is generating clouds where it shouldn't. The modeled atmosphere above the plateaus may be too cold or has too much moisture such that model atmosphere reaches saturation causing H<sub>2</sub>O ice clouds to condense over the plateaus.

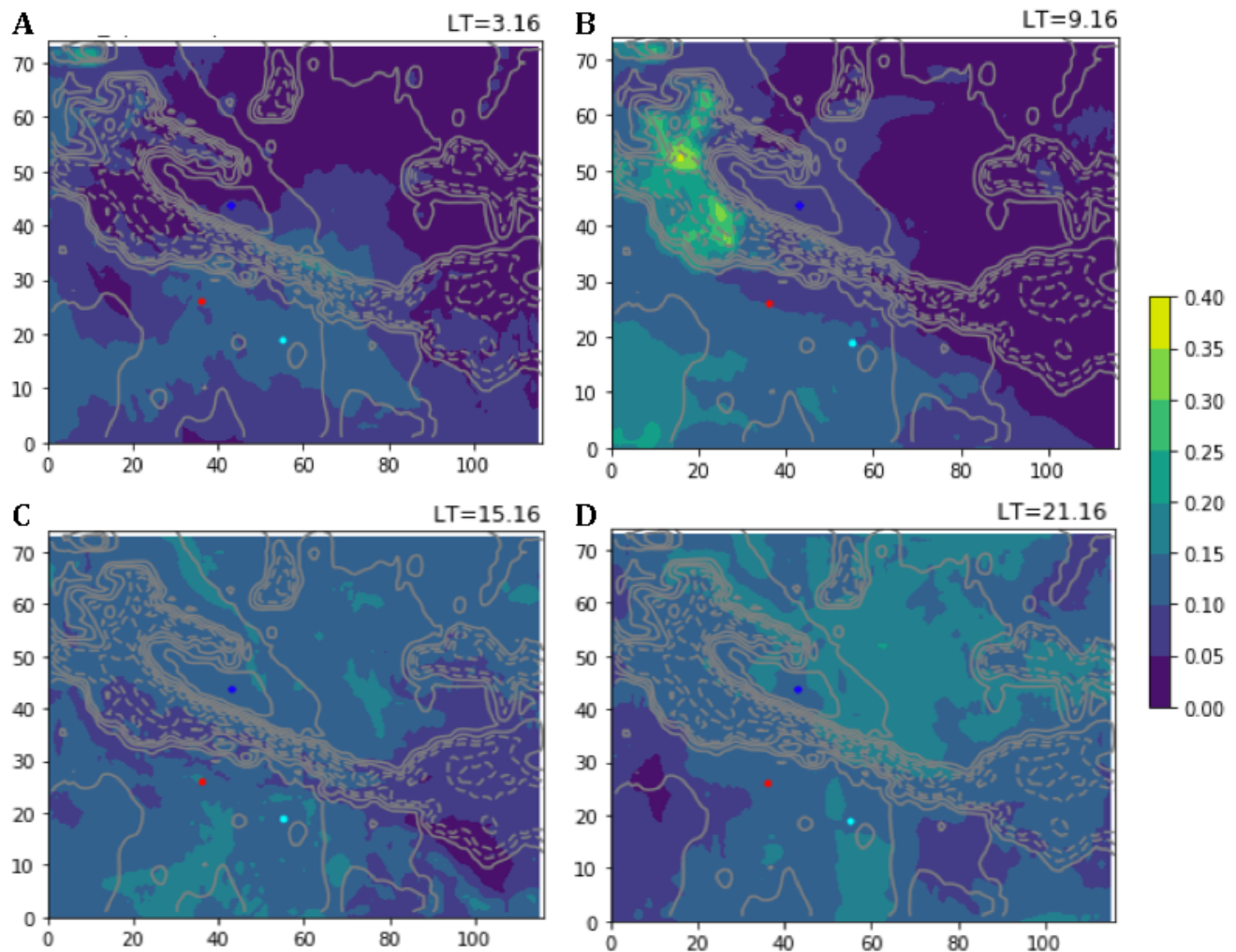


Figure 3.9 Baseline Column H<sub>2</sub>O ice optical depth at approximately (a) 03:00, (b) 09:00, (c) 15:00, and (d) 21:00 LT. Formation of water ice clouds is widespread over the grid-4 model domain.

If the observations of fogs confined only within the canyon are real, the lack of high-opacity low-lying fogs forming exclusively in Valles Marineris in our simulation is indicative that the modeled temperature and/or the modeled water concentration may be incorrect. Otherwise, the observations may be suspect, or the presence of a potential local water source

may exist in Valles Marineris, or we don't understand the physics of cloud nucleation on Mars. The following results and discussion sections evaluates these possible scenarios.

### **3.3.2 Thermal Structure**

A comparison of the diurnal cycle for near-surface temperature, total H<sub>2</sub>O, H<sub>2</sub>O vapor, and H<sub>2</sub>O ice mixing ratios inside the canyon and on the plateau is shown in figure 3.10. The temperature inside the canyon (red curve) remains higher than the temperature on the plateau (blue curve) at all times of day. This temperature differential is challenging to overcome. The amplitude of the total water inside the canyon varies by ~20% over the diurnal cycle with a short-lived minimum at 05:00 LT. In comparison, the amplitude of the total water fluctuates by a factor greater than two on the plateau reaching a maximum total water content at 10:00 LT, and a minimum value occurring around midnight. A small amount of H<sub>2</sub>O ice forms inside the canyon near 05:00 LT, whereas the formation of clouds above the plateau is much more abundant and persists from 22:00 until 09:00 LT in the morning. At no point in the day diurnal cycle does water ice form inside the canyon when water ice clouds over the plateau is absent.

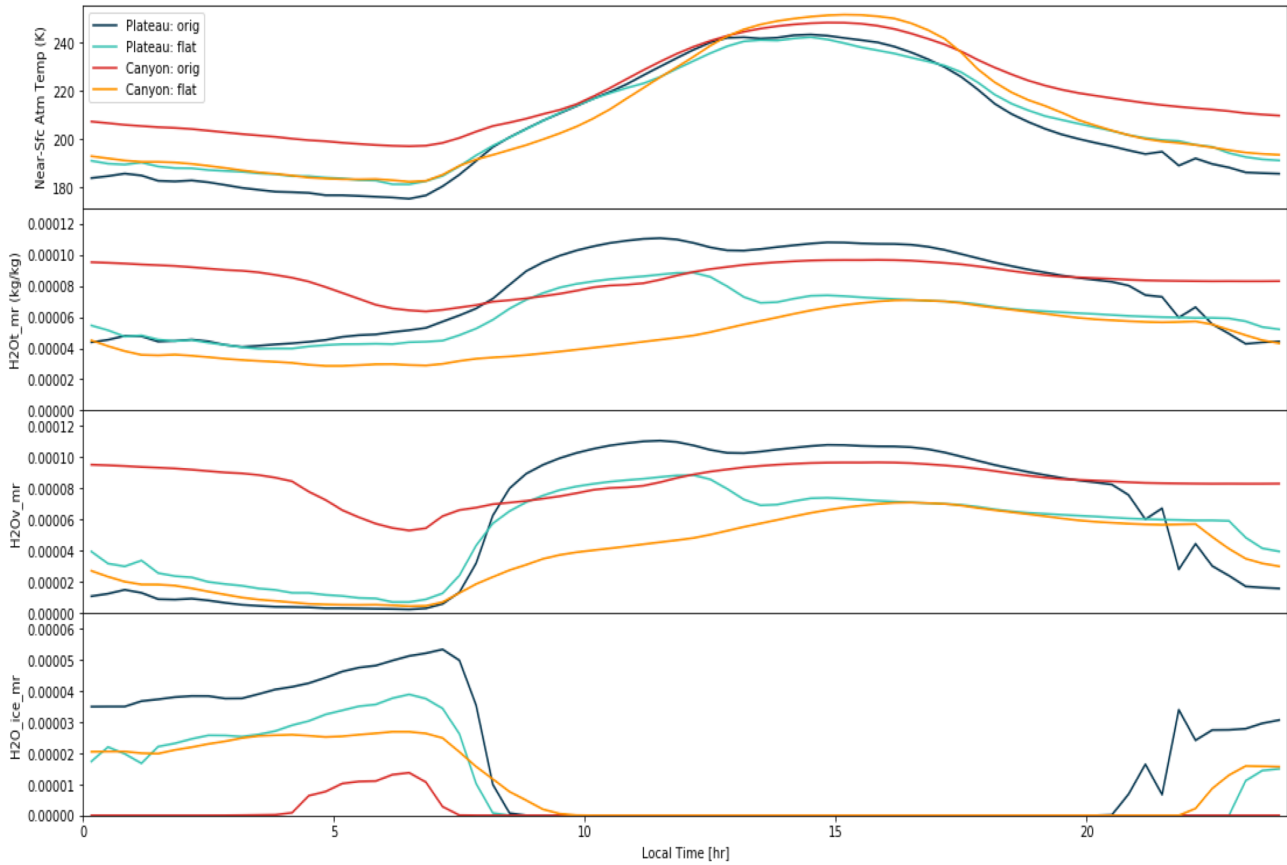


Figure 3.10 Diurnal cycle of temperature, total H<sub>2</sub>O, H<sub>2</sub>O vapor, and H<sub>2</sub>O ice mixing ratios at the lowest atmospheric layer (z= 7m) comparing points inside the canyon versus outside above the plateau. Both the baseline case and constant thermal inertia case is shown.

To investigate the radiative forcing of surface temperature differentials and may affect the formation of water ice fog in Valles Marineris, a constant thermal inertia scenario simulated which eliminate the contrast between high thermal inertia inside the canyon versus lower thermal inertia on the surrounding plateau. The model set-up for this set of

simulations is identical as the baseline scenario, using the same physical processes and grid configuration, with the exception that the thermal inertia of the entire grid 4 model domain is set to a constant value of  $250 \text{ Jm}^2\text{K}^{-1}\text{s}^{-1/2}$  and a constant albedo of 0.15 (Fig. 3.11). The baseline scenario showed widespread cloud formation over the plateau, whereas the result of the flat thermal inertia case showed high column opacity directly over the Valles Marineris canyon only without similarly high opacity water ice clouds over the plateau region, as would be the case consistent with observations of the high opacity obscuration (Fig. 3.12). The diurnal cycle for temperature, total  $\text{H}_2\text{O}$ ,  $\text{H}_2\text{O}$  vapor, and  $\text{H}_2\text{O}$  ice mixing ratios for the flat thermal inertia case is shown in figure 3.10 along-side the baseline case. While the model was able to reproduce the observed, water ice cloud distribution in the canyon once thermal inertial contrast is eliminated, a defensible justification cannot be made to drastically change thermal inertia, the remainder of the analysis will proceed with the results from the baseline scenario showing generally warmer temperatures in the canyon.

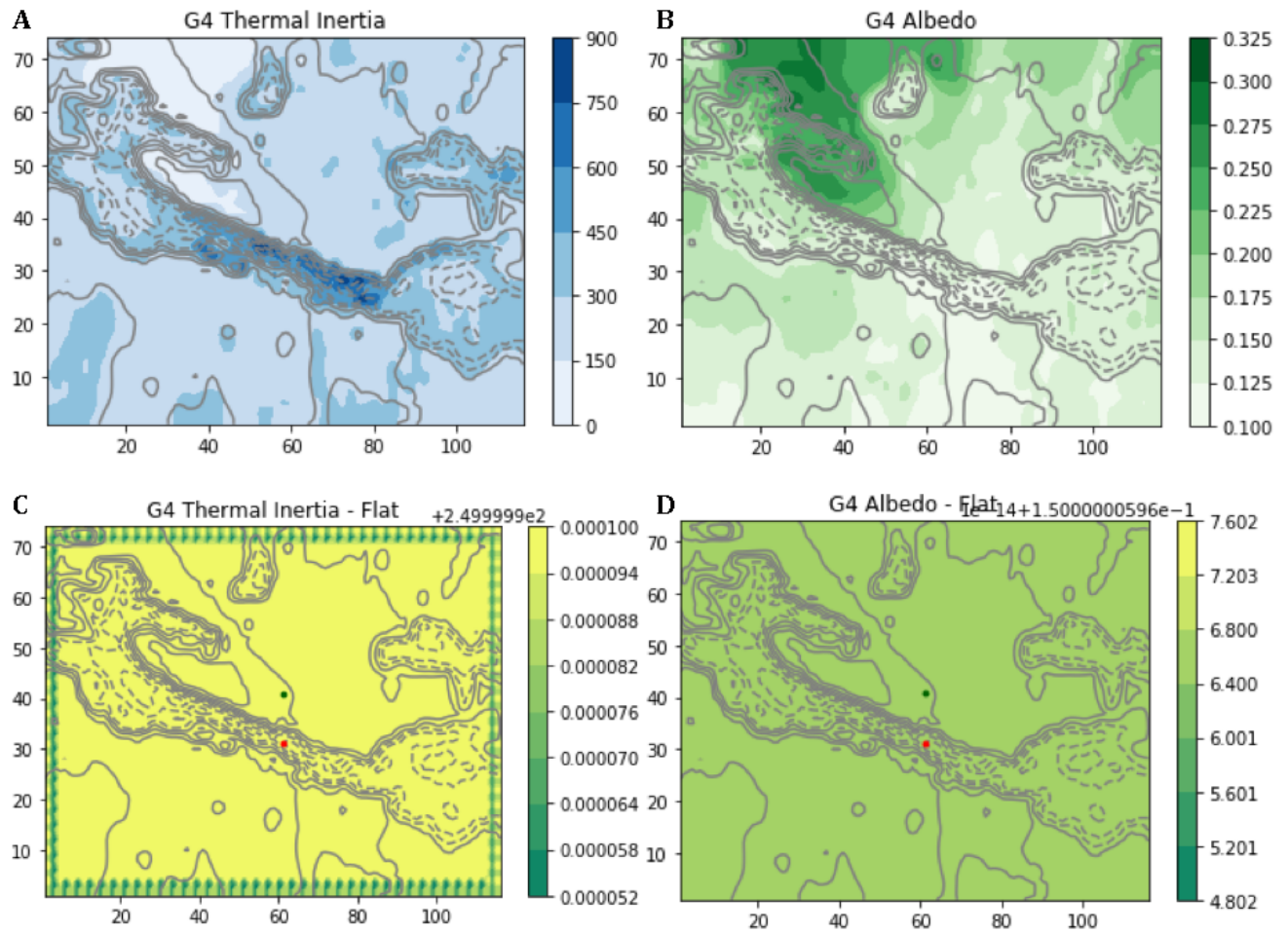


Figure 3.11 Baseline (a & b) vs. Flat (c & d) Thermal Inertia and albedo on grid-4. Red point indicates location inside the canyon, Green point indicate location on the plateau north of the canyon.

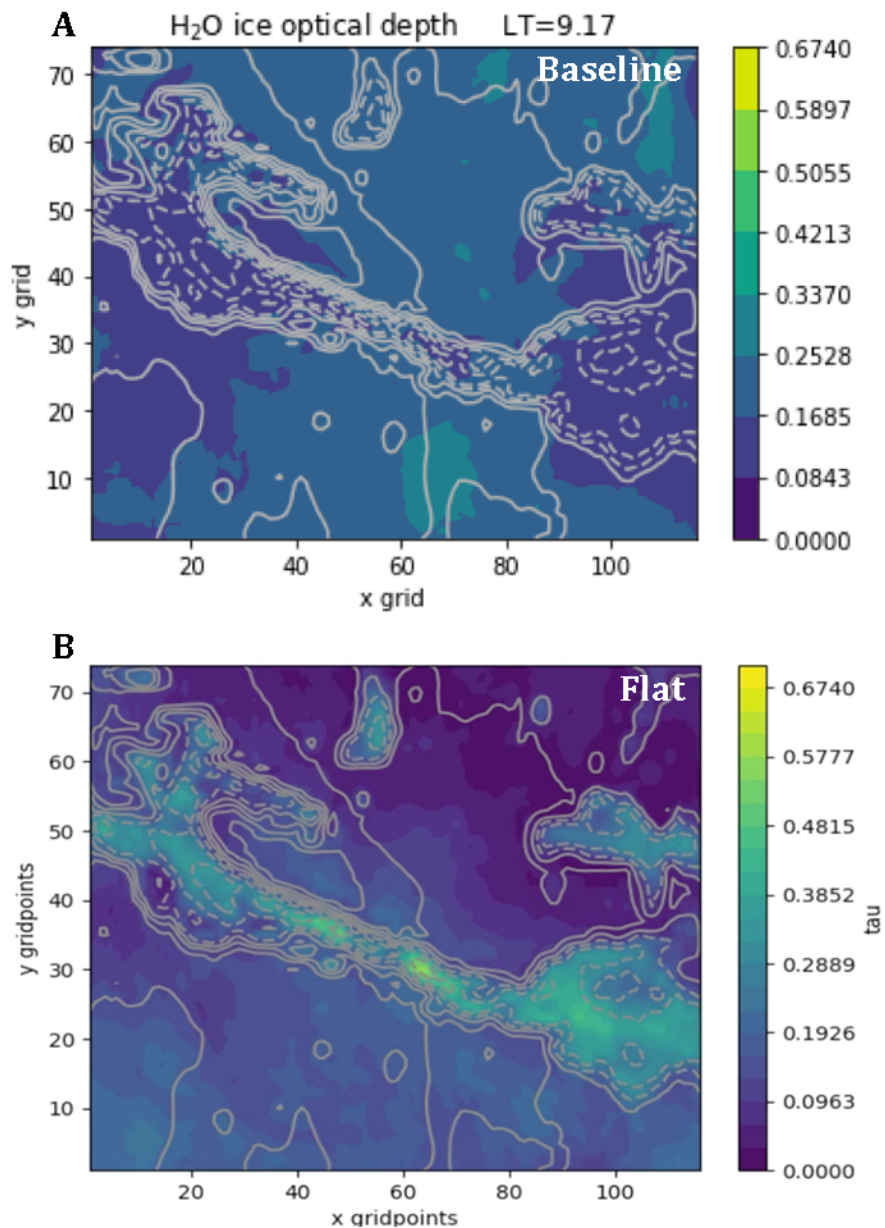


Figure 3.12 (a) Baseline vs. (b) constant thermal inertia and albedo simulation results showing grid-4 column water-ice opacity during 09:00 LT. Clouds are present both inside and outside the canyon in the baseline scenario, whereas much higher concentrations of water ice clouds can be seen inside the canyon and not on the surrounding plateau for the flat thermal inertia case.

### 3.3.3 Water Concentrations

A nadir view of the modeled precipitable water in the column minus the diurnal mean is plotted for total water, water vapor, and water ice in the column. The panels in the middle column show an excess of water vapor inside the canyon in the mid afternoon at 15:30 LT and a deficit during the morning at 06:00 LT compared to the diurnal mean value (Fig. 3.13). At the same time, the opposite is true for water ice in the column. These plots are indicative of a phase change between water vapor and water ice within the confines of the canyon. The higher concentration of ice in the morning correspond to lower temperatures when water ice clouds form, while the concentration of water vapor is higher in the canyon in the afternoon (15:30 LT) when the clouds sublimate.

Diurnal slope winds in complex terrains are typically characterized by the reversal of wind direction twice per sol: upslope during the day, and downslope at night. A substantial asymmetry in the direction of the day-night circulation results from the complex topography in the region imposed by the planetary dichotomy to the south, and the Tharsis Rise to the west. Fig. 3.14 show a convergence of moist air masses entering Valles Marineris via easterly flows, whereas dry air sweep across the plateau of the canyon system from the south towards the north in the evening. However, little of this regional advection of water make their way into the depths of the canyon, as evidence by the relatively well-mixed water concentrations inside the canyon (Fig 3.10). Vertical cross-sections of water vapor mixing ratio in the canyon is plotted in Figure 3.15 with water ice clouds in shown as contours. Vectors of vertical and meridional winds are superimposed as black. Water carried upslope



along the walls of the canyon in the mid-afternoon returns back into the canyon via subsidence, which acts to adiabatically warm the canyon and in turn exert feedbacks on the local circulation.

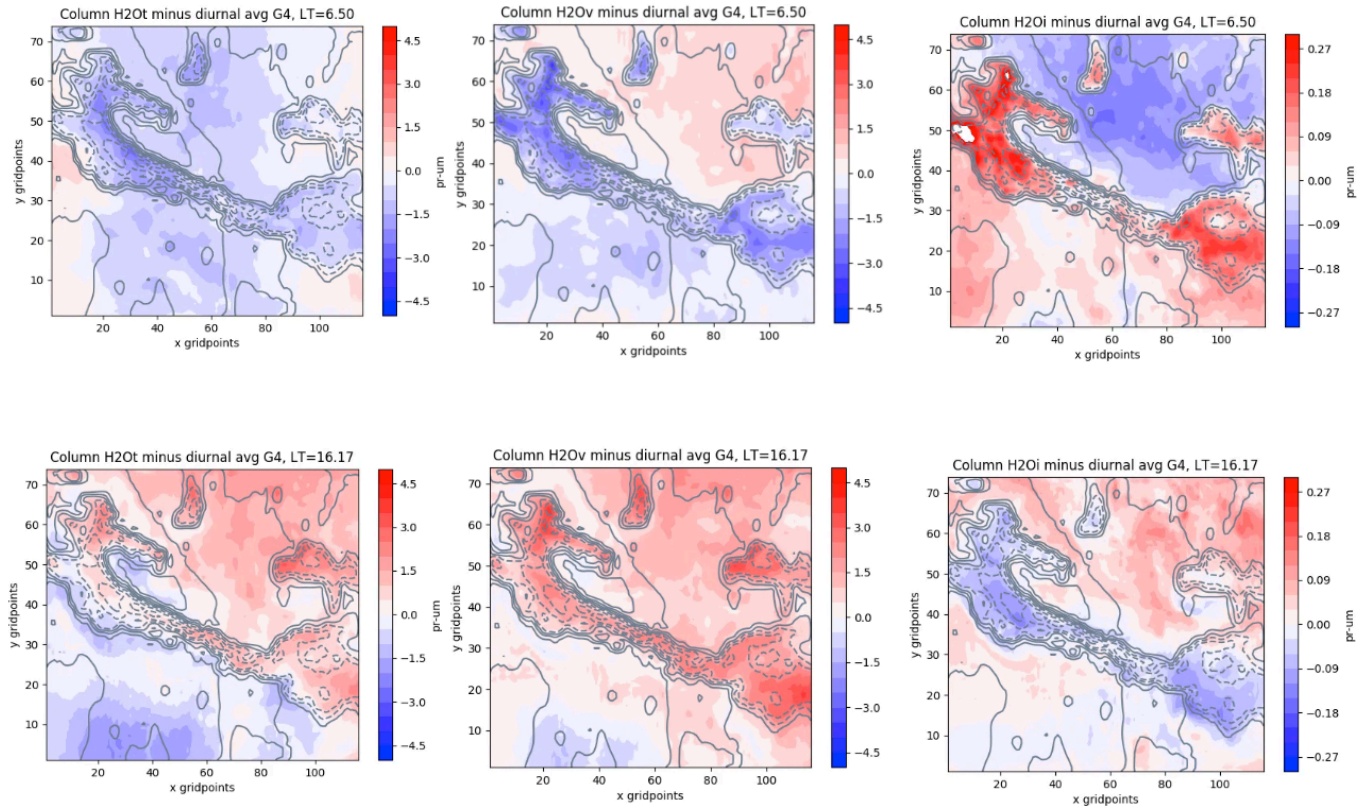


Figure 3.13 Total column H<sub>2</sub>O, column H<sub>2</sub>O vapor, and column H<sub>2</sub>O-ice minus the diurnal average showing the exchange of water between the vapor and ice phases. Higher concentration of ice is seen in the morning (06:50LT) when lower temperatures allow for the formation of water ice clouds, while the concentrations of water vapor is higher in the canyon in the afternoon (16:17 LT) when the clouds sublimate.

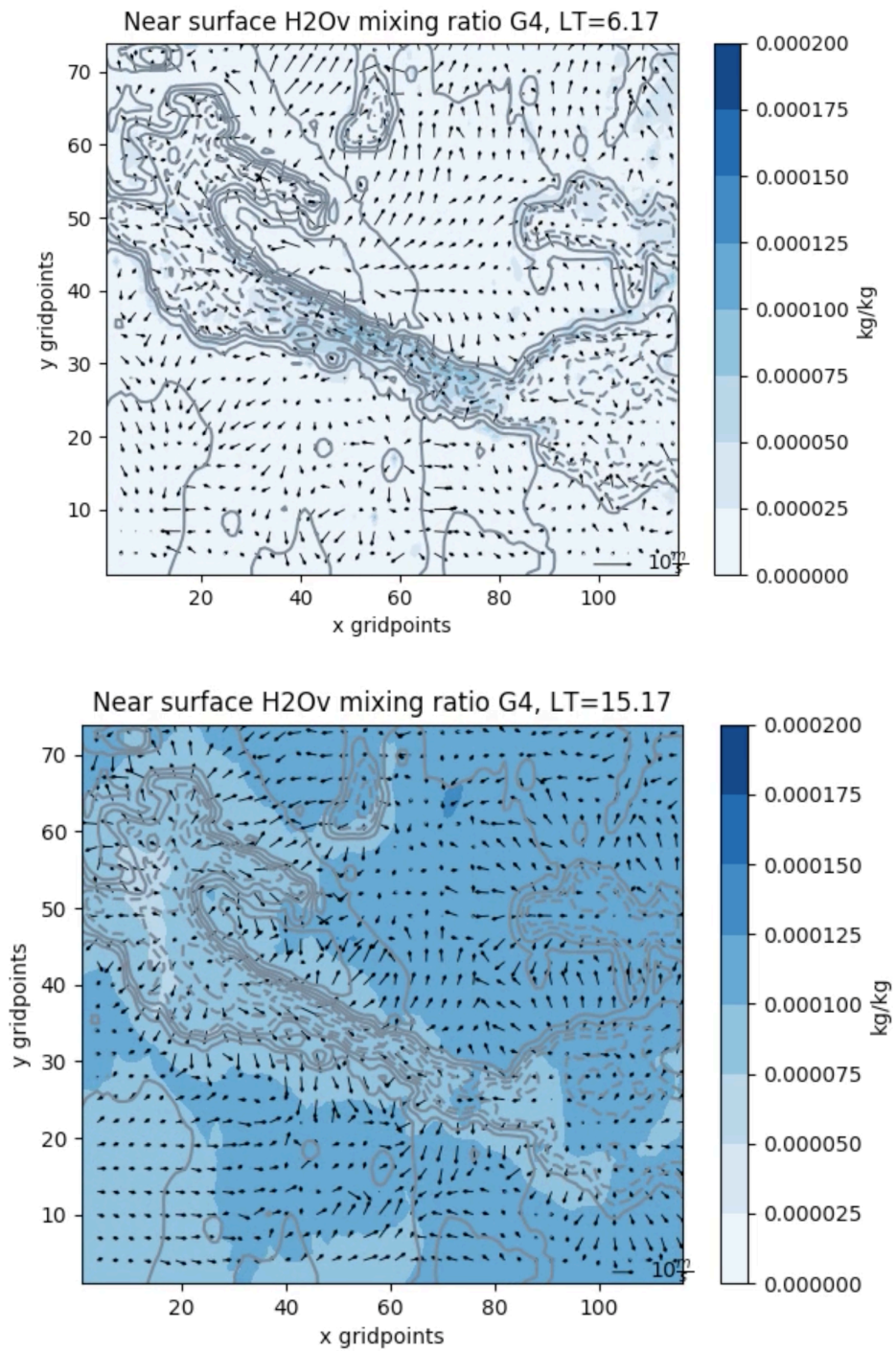


Figure 3.14 Near-surface winds and water vapor mixing ratio on grid-4 in the early morning at 06:00 vs. mid-afternoon at 15:00 LT

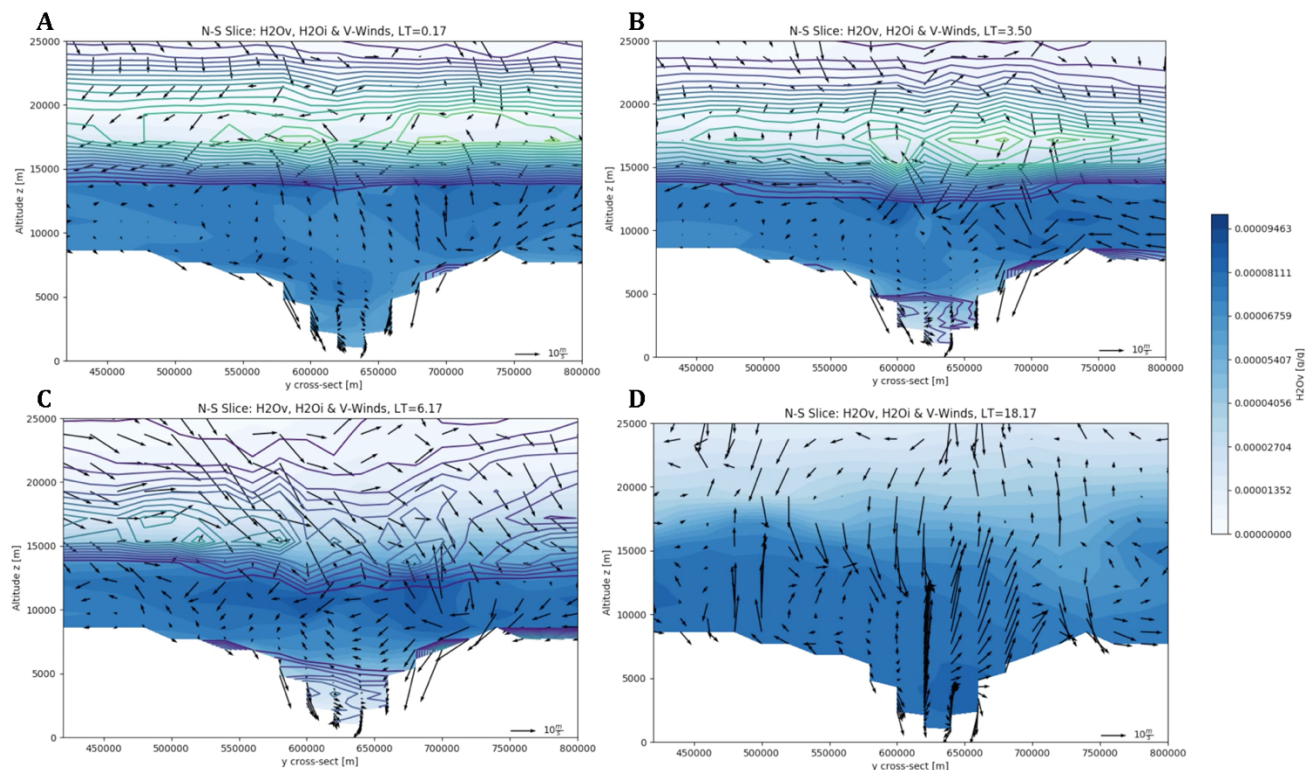


Figure 3.15 Cross-sectional view of vertical and meridional winds at 00:00, 03:00, 06:00, and 18:00 LT. Overnight formation of water ice clouds are shown in green & purple contours at the bottom of the canyon and aloft above the canyon. The length of vertical wind vectors have been exaggerated 4x.

The vertical distribution of water is commonly assumed to be uniformly well-mixed in the lower atmosphere from the surface up to the water vapor condensation level (Maltagliati et al., 2011; Smith, 2002, 2009). However, our mesoscale modeling results show that this generally may not be the case. While the vertically well-mixed assumption is mostly true above  $\sim z=5\text{km}$ , large variability in water concentration persist in the lowest kilometer of the atmosphere closest to the surface. This is especially evident in the vertical profiles of total water, water vapor, and water ice over the plateau (Fig. 3.16) where the nighttime total water mixing ratio at the surface is a factor of two less than the total water mixing ratio just

2 km above. Similar trends can be seen in the water vapor mixing ratio as well as the water ice mixing ratio, particularly at 03:00 LT. The vertical variability in water mixing ratio in the lowest scale height above the canyon floor is only is  $\sim 20\%$ , and appears much more well-mixed compared to the plateau.

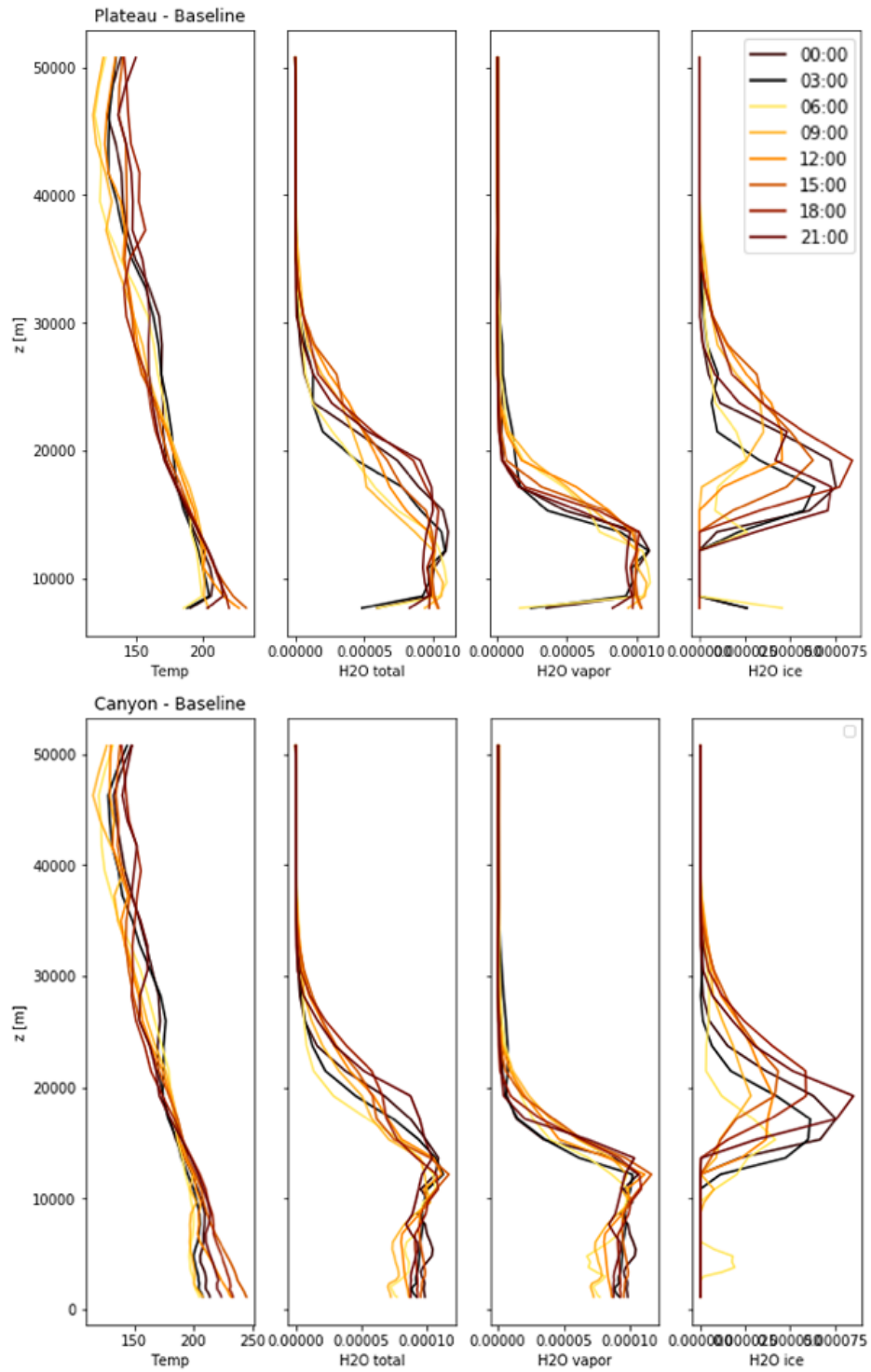


Figure 3.16 Vertical profiles of temperature, total water, water vapor and water ice mixing ratios in the canyon versus on the plateau



## **3.4 Discussion**

### **3.4.1 Nature and Structure of the ‘fog’**

The implications of these results show that under the nominal simulated scenario, the canyon remains too warm at night for high opacity water-ice fogs to form inside Valles Marineris only, with no formation of clouds over the plateau. However, the thermodynamic conditions do allow for the formation of water ice clouds inside Valles Marineris, in conjunction with wide-spread water ice clouds development over the plateau region as well. The top of the simulated water ice cloud layer is located approximately half way up the 7 km canyon. The thickness of the fog is highly dependent on the vertical temperature profile, and may exist as a detached layer that does not extend to the surface (Fig 3.16).

### **3.4.2 Effect of Thermal Inertia**

Due to the low density of Mars’ atmosphere, the Martian surface temperature is strongly modulated by radiative forcing by underlying surface properties such as thermal inertia. Cooler temperatures inside the canyon maybe allowing water-ice clouds to form more readily. The sensitivity analysis conducted with the flat thermal inertia and albedo simulation shows that to first order, cloud formation inside the canyons is primarily controlled by radiative effects exerted by surface properties such as thermal inertia. Initially, our regional atmospheric simulations in the Valles Marineris region used the thermal inertia map as derived from TES retrievals (Putzig & Mellon, 2007). According to this data, the thermal inertia values inside the canyon are higher than on the plateau by nearly a factor of

four. In this scenario, our model showed that nighttime temperatures inside the canyon are generally much warmer than those outside, making it thermodynamically difficult to form optically thick clouds inside the canyon and little to no clouds outside. On the other hand, when we ran the same simulation set up for a scenario with a constant thermal inertia value in the canyon and on the plateau, the temperature contrasts are dramatically reduced, resulting in the lingering of higher opacity water layers inside the canyon during the morning at times consistent with when the HRSC observations were taken. While flattening the thermal inertia dramatically changed the radiative forcing, it is important to remember that radiative and dynamical processes are non-linearly coupled, such that changing the thermal inertia will change the temperature, which in turn changes the circulation and the dynamical heating.

While cloud formation in the model can be influenced by imposing a constant thermal inertia, there is abundant evidence for higher thermal inertia (i.e., rocky) surface materials inside Valles Marineris, so making it the same as outside the canyon is not realistic. Nonetheless, the results from changing the thermal inertia in the canyon are interesting and point to a primarily radiative process for the warming seen in the unaltered thermal inertia scenario. Although the constant thermal inertia case resulted in the formation of water ice fogs exclusively inside the canyon resembling the observation by PFS and HRSC, there is insufficient justification for dramatically changing the thermal inertia in the canyon. However, Wilson et al. (2007) showed that the presence of atmospheric dust and clouds could potentially bias the retrieved thermal inertia, since orbital measurement in dusty and cloudy scenarios may be probing the top of the aerosol layer instead of the surface. Given

dust is frequently observed in Valles Marineris, estimating the error in the THEMIS-derived thermal inertia values associated with aerosol in the canyon may be a more appropriate sensitivity analysis rather than applying a constant thermal inertia to the entire grid-4 domain.

### **3.4.3 Bias in Modeled Water Concentration**

As discussed in section 3.2.2, water in MRAMS is initialized from the MGCM. However, the global scale model cannot resolve the depth of Valles Marineris. The ingested profile of water in MRAMS is based on a linear extrapolation of the quantity of water at the two lowest MGCM atmospheric levels. As of yet, no spacecraft has taken measurements of water concentrations inside Valles Marineris, and a validation of the MRAMS distribution of water used in our simulation against observations is not possible. However, given the significant depth of the canyon below the altitude of the lowest MGCM layer, there is reason to believe that the amount of water in the MRAMS initial state may be artificially high. The quantity of water in MRAMS is expected to equilibrate after spin-up. But it is still worth noting that our analysis of cloud formation conditions in Valles Marineris may hinge on a 3-dimensional distribution of water that carries an intrinsic degree of bias.

### **3.4.4 Potential Water Source?**

Though infrequent, terrestrial fog events have been observed in the Arizona Grand Canyon on Earth where the canyon fills with clouds while the surrounding plateau remains essentially cloud-free (Fig 3.17). While the fog on Earth is composed of liquid water droplets



instead of water-ice, valley fogs may be regarded as a terrestrial analog for the phenomenon we observe on Mars. Grand Canyon fogs typically occur in the winter, in the presence of a nocturnal temperature inversion, and following heavy precipitation where the ground becomes a local water source. The evaporation of water droplets coupled with the statically stable atmosphere increases the atmospheric water vapor in the canyon. Unlike other terrestrial valleys, winter time temperature profiles in the Grand Canyon on Earth exhibit a neutral to isothermal stratification during both daytime and nighttime, with only rare instances of actual temperature inversions (Whiteman et al., 1997). The canyon warms during daytime and cools during nighttime more or less uniformly through the canyon's entire depth. This weak stability and temperature structure evolution differ from other mountain valleys, which develop strong nocturnal inversions and exhibit convective and stable boundary layers that grow upward from the valley floor (Whiteman et al., 1997).

While the fog in the Grand Canyon results from the combination of rainfall combined with infrequent nocturnal inversions, our simulations show that nocturnal inversions in Valles Marineris is rather common, making the Martian counterpart more effective at confining water ice and dust in the lowest atmospheric layers. However, the requirement of significant amount of rainfall for Grand Canyon fog formation is difficult to justify for Mars. The physical dimension of Valles Marineris is much greater than any terrestrial counterparts, and the volume estimates of Valles Marineris is many times the volume of the Grand Canyon on Earth. The persistence of a local water source in Valles Marineris sufficient to provide the quantity of moisture needed to saturate the canyon is highly improbable.



Figure 3.17 Fog event observed at the Grand Canyon, Earth  
(Image Credit: National Park Services)

### **3.5 Conclusions**

The investigation of water ice fogs inside the Valles Marineris canyon system revealed that it is possible to form thin layers of water ice clouds in Valles Marineris that are confined entirely within the lower reaches of the canyon under certain conditions when the atmosphere becomes saturated. However, the nature of the low-lying clouds inside Valles Marineris is completely unlike fogs observed in terrestrial canyons such as those in the Grand Canyon on Earth. Any potential fogs in Valles Marineris typically form in conjunction with much higher opacity dust layers, and are highly influenced by the radiative feedbacks due to the thermal properties of the underlying surface. Orbital images from the Mars Express High-Resolution Stereo Camera (HRSC) revealed a high opacity layer that appeared to be confined entirely within the bottom of the canyon. Coordinated spectral observations

using the OMEGA instrument interprets the aerosol layer to be primarily comprised of dust (Inada et al., 2008), while the Planetary Fourier Spectrometer detects the presence of a water ice signature (Möhlmann et al., 2009). Our mesoscale modeling study tries to resolve this apparent discrepancy by simulating the dynamics of winds, dust, and water in Valles Marineris and evaluating the thermodynamic conditions required for the formation of fogs and low lying-clouds in those regions.

An interesting finding from this research shows that to first order, cloud formation inside the canyons is primarily controlled by the thermal inertia of the surface. Initially, our regional atmospheric simulations in the Valles Marineris region used the thermal inertia map as derived from TES retrievals (Putzig & Mellon 2007). According to these data, the thermal inertia values inside the canyon are higher than on the plateau by nearly a factor of four. In this scenario, our model showed that nighttime temperatures inside the canyon are generally much warmer than those outside, making it thermodynamically difficult to form optically thick clouds inside the canyon and little to no clouds outside. On the other hand, when we ran the same simulation with a constant thermal inertia value in the canyon and on the plateau, the temperature contrasts are dramatically reduced, resulting in the lingering of higher opacity water layers inside the canyon during the morning at times consistent with when the HRSC observations were taken. Nocturnal clouds and fogs present in Valles Marineris and not on the surrounding terrain indicate non-homogeneous mixing of water vapor throughout Valles Marinaris and the surrounding plateaus. Differential rates of heating and cooling inside versus outside the canyon are off-set in phase, leading to conditions that are more conducive to cloud formation inside the canyon during the early

morning. Additional simultaneous observations by imagers and spectrometers of high opacity aerosol layers in Valles Marineris would be helpful for determining the exact nature, composition, and temporal variability of the water-ice fog.

## CHAPTER 4

### ATMOSPHERIC INFLUENCES ON RECURRING SLOPE LINEAE ACTIVITY

#### 4.1 Introduction

Recurring slope lineae (RSL) are narrow, dark streaks that incrementally lengthen when temperatures are warm, fade when inactive (usually during cooler seasons), and reappear over multiple Mars years (McEwen et al., 2011; 2014). RSL typically occur on steep low-albedo slopes, and are characterized by their annual recurrence in the same approximate location, even following the same complex flow paths at times (Schaefer et al., 2019). The lengthening rates of mid-latitude RSL are highest at the beginning of each season, followed by a much slower lengthening phase. RSL emanate from bedrock outcrops on the walls of well-preserved craters, central peaks and pits of impact craters, canyon walls, fossae, and light-toned layered deposits (LLDs), and many terminate on large sediment fans (Chojnacki et al., 2016; Stillman, 2017). Others leave bright deposits when inactive from previous years.

The Mars Reconnaissance Orbiter (MRO) High Resolution Imaging Science Experiment (HiRISE) (McEwen et al., 2007) has been instrumental in detecting new occurrences of RSL as well as monitoring seasonal and interannual variations of RSL activity. While RSL are typically found in association with outcropping bedrock on low-albedo, steep slopes, many locations exhibiting these characteristics lack RSL activity. Only ~11% of the locations targeted by HiRISE deemed as high RSL potential locations yielded detections of RSL (Stillman, 2017), suggesting that the presence of RSL is dictated by factors in addition to

morphological constraints. After the 2018 planet-encircling dust storm, RSL activity in the southern middle latitudes were significantly enhanced (McEwen, 2018). Furthermore, Stillman (2017) constrained the seasonality of five RSL regions as a function of slope orientation, and showed that some regions have two or more pulses of activity, indicating that triggering mechanisms must occur multiple times and reset quickly during the RSL active lengthening season.

The origin of RSL remains an open question. A number of formation hypothesis have been proposed, including dry, wet, and wet-triggered mechanisms. For dry granular flows (Dundas et al., 2017; Schmidt et al., 2017), darkening may be caused by changes in surface roughness, grain sorting, or dust removal, while fading could occur via subsequent atmospheric dust deposition (Dundas et al., 2017) or by removing dust from areas surrounding the RSL (Schaefer et al., 2019). Many RSL terminate on slopes at the dynamic angle of repose of active dune slip faces on Mars, 28-32° (Atwood-Stone & McEwen, 2013), suggestive of granular mass wasting. However, large interannual variations in RSL length may indicate that RSL do not stop advancing because they encounter slopes that are less than the angle of repose, but rather stop advancing because the mechanism that controls their flow is no longer active. In fact, Stillman et al. (2020) has shown that some RSL can have mean slope angles that are below the angle of repose.

Wet-dominated mechanisms such as seeping water or surface flow involve liquids percolating downslope to produce incremental lengthening (Chevrier & Rivera-Valentin, 2012; Grimm, Harrison, & Stillman, 2014; J. Levy, 2012; Ojha et al., 2015; Stillman, Michaels,

& Grimm, 2017; Stillman, Michaels, Grimm, & Hanley, 2016; Stillman, Michaels, Grimm, & Harrison, 2014; Watkins et al., 2014). While the origin of the saline brines may be sourced from shallow ice melts or groundwater aquifers, Levy et al. (2011; 2012) suggests that deliquescence of subsurface or atmospheric vapor onto oxychlorine salts (chlorates and perchlorates) may be sufficient to dampen the uppermost layer of soil to cause darkening. Analog studies of terrestrial water tracks in Antarctica found liquids flowing through the top tens of centimeters within the unfrozen active layer near the surface (Levy et al., 2011; Levy et al., 2012), and darkening of the ground occurs when salts deliquesce during periods corresponding to relative humidity surges (Dickson et al., 2013). It has been suggested that RSL may result from a similar process of darkening of the soil by deliquescence of perchlorate and chloride salts present in the Martian soil (Heinz, Schulze-Makuch, & Kounaves, 2016).

Finally, the wet-triggered debris flow hypothesis postulates a primarily dry granular flow with the role of a volatile to initiate activity. Dundas et al. (2017) proposes that small amounts of liquid may initiate the granular flow due to the destabilization of grain contact cohesion as the volume of salts changes as they undergo cycles of hydration and dehydration. Massé et al. (2016) posits boiling liquid can induce grain saltation that leads to slope destabilization and triggers dry granular flow (as little as 70 grams in Masse's experiments). Experiments by Raack et al. (2017) further showed that rapidly boiling freshwater forms saturated sediment pellets that partially levitate on a cushion of water vapor leading to a sediment transport capacity nine times greater than when this effect is absent. Debris flows

resulting from wet-triggered mechanisms may create a geomorphological impact that is disproportionately greater than the amount of liquid involved. Given the widespread terrains on which RSL are found, it has even been suggested that RSL may be formed by multiple mechanisms under different conditions (Stillman, 2017).

The temperature dependence and seasonality of RSL activity strongly suggest that a volatile may be involved. No spectroscopic evidence for actual water has been detected for RSL. The spectral signature of hydrated oxychlorine salts have been identified by MRO's CRISM (Compact Reconnaissance Imaging Spectrometer for Mars) spectrometer at four RSL locations only during the active seasons of RSL when the surface is darkened (Ojha et al., 2015) but recent work suggests that the hydrated oxychlorine absorption bands are actually artifacts from the CRISM data processing (Leask et al., 2018). Laboratory experiments show that only small amounts of water (5 wt. % and no liquid film on surface) is needed to darken basaltic soils while producing weak spectral features (Pommerol et al., 2013). Chloride salts have not been detected from orbit at any RSL sites (Mitchell & Christensen, 2016). It is possible that the spectral signature of the salt is hidden under a layer of unconsolidated regolith on top of a salt encrusted layer.

Chlorine-bearing salts, including oxychlorine and chlorides, are of particular interest because of their ability to transition from a solid crystalline salt into an aqueous solution given the appropriate temperature and relative humidity (Gough et al., 2011; 2014; Nikolakakos & Whiteway, 2018; Nuding et al., 2014; Fischer, Martínez, & Renn, 2016; Zorzano et al., 2009). Although pure liquid water is typically unstable on the surface of



present-day Mars, salty brines may be temporarily stable on the surface or subsurface (Brass, 1980; Clark, 1978; Ingersoll, 1970), especially during the pre-dawn and early morning hours (e.g., Gough et al., 2011, 2014; Nikolakakos & Whiteway, 2018; Nuding et al., 2014). In situ observations of perchlorate ( $\text{ClO}_4$ ) salts have been identified at the Phoenix landing site (Hecht et al., 2009), by the Curiosity Rover (Leshin et al., 2013; Ming et al., 2014), and implied in the re-analysis at the two Viking Lander locations (Navarro-González et al., 2010). Even so, the quantity of perchlorate is small (<1%) so the potential liquid volumes are likely limited and transient.

There is compelling evidence supporting the influence of the atmosphere on RSL activity. RSL are widely distributed geographically and appear over a variety of landforms as well as elevations. They have been found to extend from the tops of ridges, as well as from the crest of dunes composed of permeable sand where a groundwater source of water is unlikely (McEwen et al., 2015). If a volatile is involved in the formation of RSL, the source of water needs to be ubiquitous, suggesting an atmospheric source. The atmosphere may further exert control on the activity of RSL via thermodynamic conditions. As mentioned previously, RSL show a strong dependence on surface temperature, which can be modulated based on the condition of the atmosphere. Finally, RSL are especially active following dust storms which have the effect of altering the local temperature and water content, further suggesting that the atmosphere play a role in the activity of RSL.

The water budget estimates for RSL based on wet-dominated flows at sites investigated by Grimm et al. (2014) and Stillman et al. (2016; 2017) is greater than  $0.4 \text{ m}^3$  of brine per meter of headwall. This quantity is estimated by determining the amount of water

needed to fill interstitial pore space and by calculating the water lost via evaporation or sublimation using the outputs from thermophysical and porous flow models (Grimm et al., 2014). This translates to a flow rate of approximately  $7 \text{ ml s}^{-1}$  as described by Raack et al., (2017). The average global annual column abundances of water vapor in the Martian atmosphere is about  $10 \text{ pr-}\mu\text{m}$  (Bruce M. Jakosky & Farmer, 1982). At a 50% trapping efficiency, at least  $0.7 \text{ km}^2$  of atmosphere is required to satisfy the RSL water budget (Stillman et al., 2016). Atmospheric water vapor alone is unlikely to be the source of volatile for wet-dominated flows without an extremely efficient mechanism for concentrating the vapor onto the RSL. However, deliquescence of Cl-bearing salts may extract enough atmospheric water to support RSL formation via near-surface dampening or wet-triggered debris flows.

In this research, we evaluate the influences of the atmosphere on RSL activity. We investigate the conditions for deliquescence at four RSL sites across five different seasons to estimate the water budget available from the atmosphere for deliquescence, and to determine any correlation between seasons where conditions for deliquescent is favored versus the frequency of RSL activity observed. Our investigation will address the seasonal and diurnal variability of deliquescence conditions based on an evaluation of temperature and relative humidity as related to the stability of liquid brines on the surface of Mars. In situ measurements of temperature and relative humidity in the equatorial and mid-latitudes have only been observed at Gale Crater and at the Viking Landers sites. A mesoscale atmospheric model is appropriate for this study as it is able to simulate near-surface

environments across different regions of Mars where data are not currently available. Section 2 of this paper describes the modeling setup. Results on the duration and timing of liquid brine stability along with the quantity of water that may be extracted from the atmosphere are presented in section 3. In section 4, we provide a comparison between modeled deliquescence with observed RSL activity, and conclusions are presented in Section 5.

## **4.2 Methods**

### **4.2.1 Model Description and Set-Up**

Four RSL sites have been selected for this study: Rauna Crater, Krupac Crater, Garni Crater, and Hale Crater. Each of these study sites represents a confirmed, well-monitored RSL location, exhibiting characteristic RSL behavior of incremental growth, fading, and annual recurrence. The four sites were selected to span across a variety of longitudes, latitudes, elevations, and geographic settings (Table 4.1; Fig. 4.1). In the northern mid-latitudes, Rauna Crater in Acidalia Planitia hosts RSL that are found on steep slopes below the elevation of the surrounding plains (Stillman et al., 2016). Krupac Crater is located close to the equator in the low-albedo tropical highlands of Tyrrhena Terra at an elevation of 1800 m, where little surrounding terrain lies above this height. RSL at Krupac Crater emanate below exposed ancient bedrock especially along the crater's eastern rim. Garni Crater, situated in eastern Melas Chasma on the canyon floor of central Valles Marineris, represents one of the lowest lying RSL sites at an elevation of nearly -5000 m (Stillman, 2017). Lineae activity observed at this equatorial site have dramatic contrasts in seasonality depending on

whether the slope is generally north-facing or south-facing. For example, RSL on north-facing slopes are most active when the subsolar latitude is to the north, then cease and commence on south-facing slopes at the season when the most insolation is received on south-facing slopes (McEwen et al., 2014). Slope-dependent seasonality are less apparent at mid-latitude sites since equator-facing slopes have a permanent thermal advantage. Finally, Hale Crater in the southern mid-latitudes is a larger impact crater compared to the other sites in this study, and RSL there are found on the steep slopes within the central peaks of the crater (Stillman & Grimm, 2018).

<b>RSL Site</b>	<b>Region</b>	<b>Latitude</b>	<b>Longitude (E)</b>	<b>Crater Diameter (km)</b>
<b>1</b> Rauna	Chryse & Acidalia Planitiae (CAP)	35.260°N	327.928°	2.53
<b>2</b> Krupac	Low-Albedo Tropical Highlands (LATH)	7.803°S	86.059°	10.0
<b>3</b> Garni	Valles Marineris (VM)	11.516°S	290.308°	2.57
<b>4</b> Hale	Southern Mid-Latitudes (SML)	35.682°S	323.484°	137.5

Table 4.1 Characteristics of the four RSL study locations. RSL regions are classified according to (Stillman, 2017)

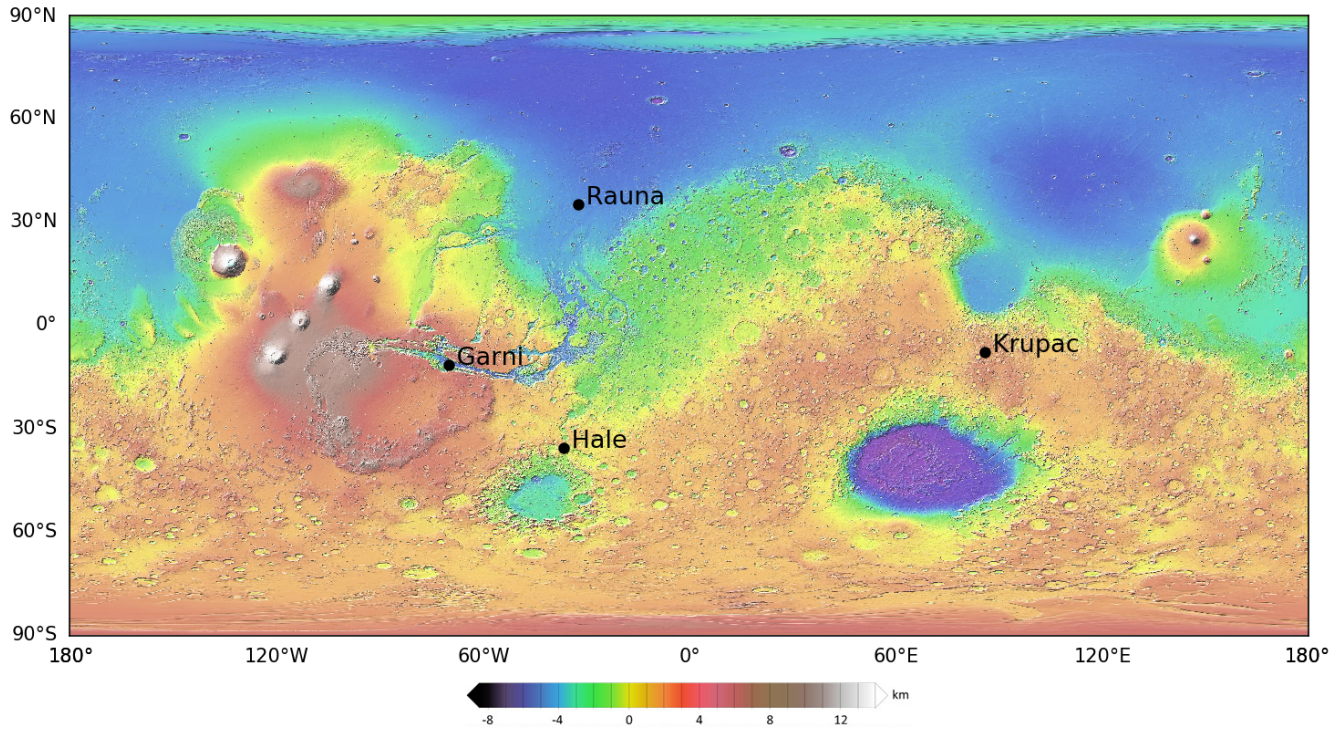


Figure 4.1 The location of the four RSL sites in this study superimposed on a MOLA topographic map. The four sites, Rauna Crater, Krupac Crater, Garni Crater, and Hale Crater were chosen to span over a variety of areas on Mars covering equatorial region in the east and the west as well as northern and southern mid-latitudes locations.

Numerical simulations at each of the four RSL locations are generated using the Mars Regional Atmospheric Modeling System (MRAMS), which is a non-hydrostatic, 3D mesoscale model that includes a fully interactive water cycle, cloud microphysics, interactive dust lifting, and a subsurface soil model (Rafkin et al., 2001). For each of the four study sites, MRAMS is used to simulate the near-surface atmospheric conditions at five seasons of interest: solar longitude  $L_s = 20^\circ, 140^\circ, 180^\circ, 270^\circ, 345^\circ$ . These times of year were chosen to bracket the seasons of RSL activity (Stillman, 2017), including the onset of incremental

growth, peak lengthening, fading, as well as periods when no activity is observed. The initial atmospheric state and boundary conditions are taken from the output of a NASA Ames Mars General Circulation Model (MGCM) simulation. A detailed description of the model initialization is presented in Section 2.3.2.3. For this mesoscale model simulation, cloud microphysical processes and sedimentation have been turned off. Water vapor is radiatively active, while dust remains radiatively inert for this experiment. Dust is kept as a passive trace as the radiative effects of dust is not the dominant process investigated in this study. For each of the four simulated RSL sites, MRAMS is configured to use 8 nested model grid domains, with the inner-most grid centered directly on the region where RSL are observed (Figure 4.2 to 4.5). The grid spacing between adjacent grid points is 240 km on the mother domain, ~3 km on grid-5, and reduces to ~100 m near the center of the innermost grid-8 domain.

The topography at the lower boundary in the MRAMS grid-8 domain is based on the 128 pixels per degree MOLA data. It is important to note that RSL source regions are typically craggy rocky outcrops in bedrock alcoves with lots of high slopes and shadows that are unlike the rolling MOLA topography simulated in MRAMS. Analysis using HiRISE orthorectified-images and Digital Elevation Maps (DEM) have recently been developed to characterize the thermal environments of RSL sites (Schorghofer et al., 2019) and to detect seasonal changes on numerous slope orientations (Stillman et al., 2020) at high spatial resolutions (up to 1 m per pixel). While MRAMS is unable to resolve slopes at these resolutions, the strength of this mesoscale study lies in the seasonal representation of the

regional near-surface temperatures and water content, rather than an attempt to replicate the specific slope angles and surface thermal properties of each RSL.

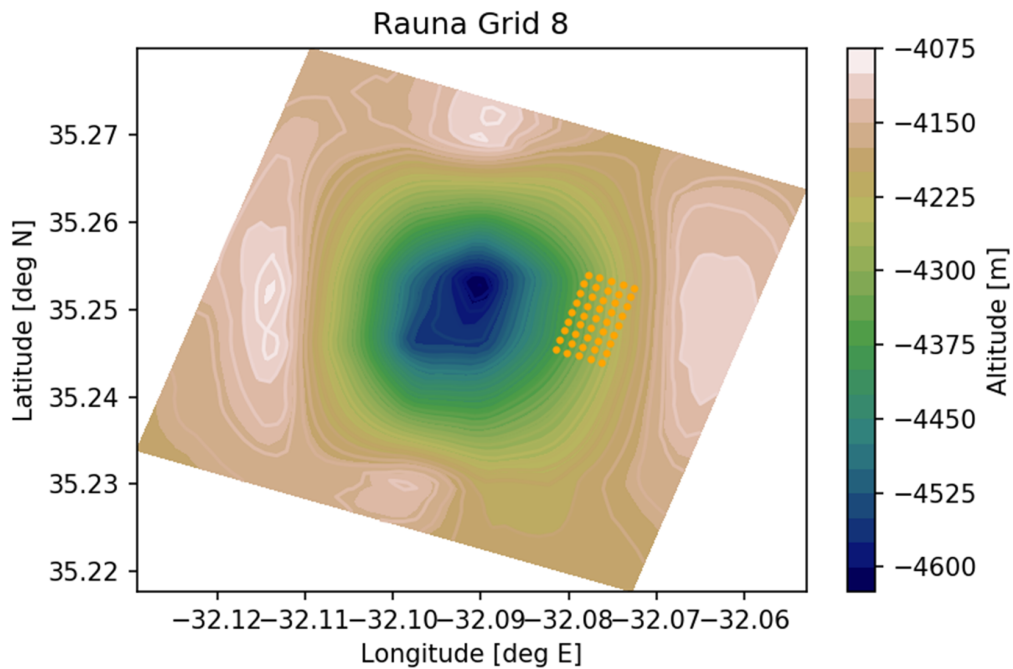
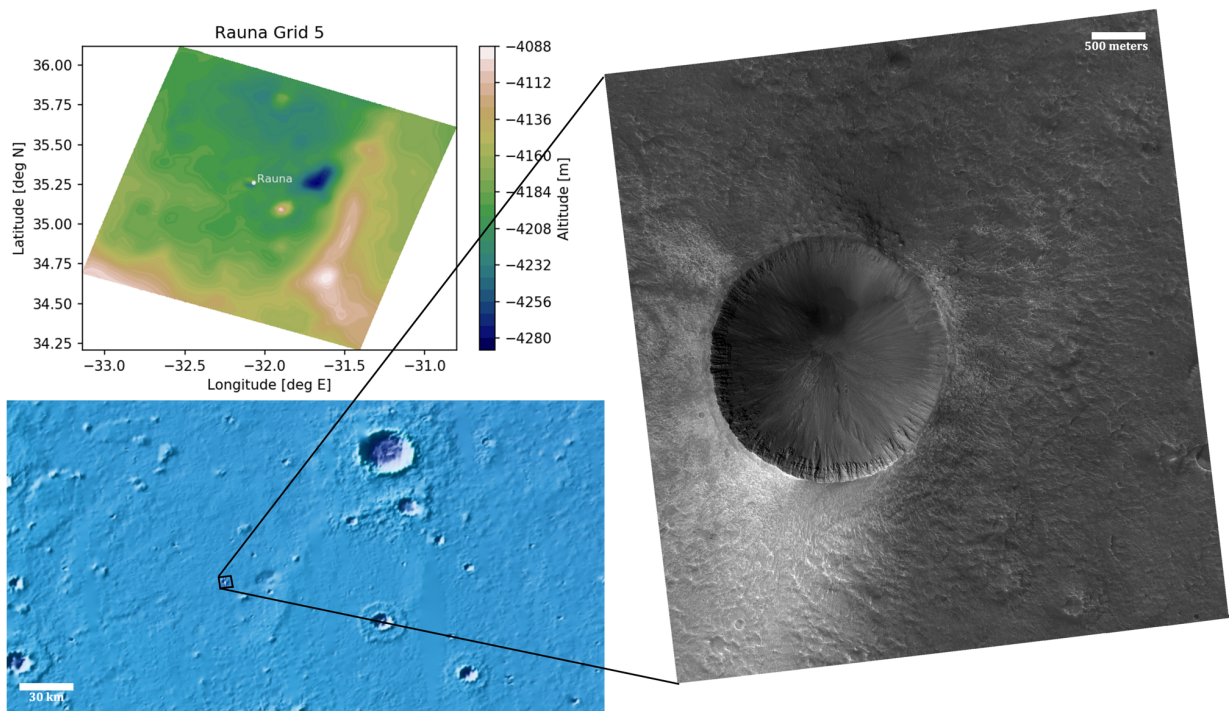


Figure 4.2 RSL site at Rauna Crater ( $35.260^{\circ}\text{N}$ ,  $327.928^{\circ}\text{E}$ )  
 (a) MRAMS grid 5 model configuration. The location of Rauna Crater is marked near the center of the grid domain. (b) MOLA color-coded elevations. MOLA colors are same



as the scale in figure 4.1. The blue box over Rauna crater outlines the HiRISE stamp for image ESP\_041976\_2155. (c) Map-projected HiRISE image ESP\_041976\_2155. (d) MRAMS grid-8 model configuration. Orange dots on the western portion of the crater covers regions associated to where RSL are present in observations. Spacing between orange dots corresponds to the model grid spacing. Points shown represent the grid points used for performing a spatial averaging on the model output.

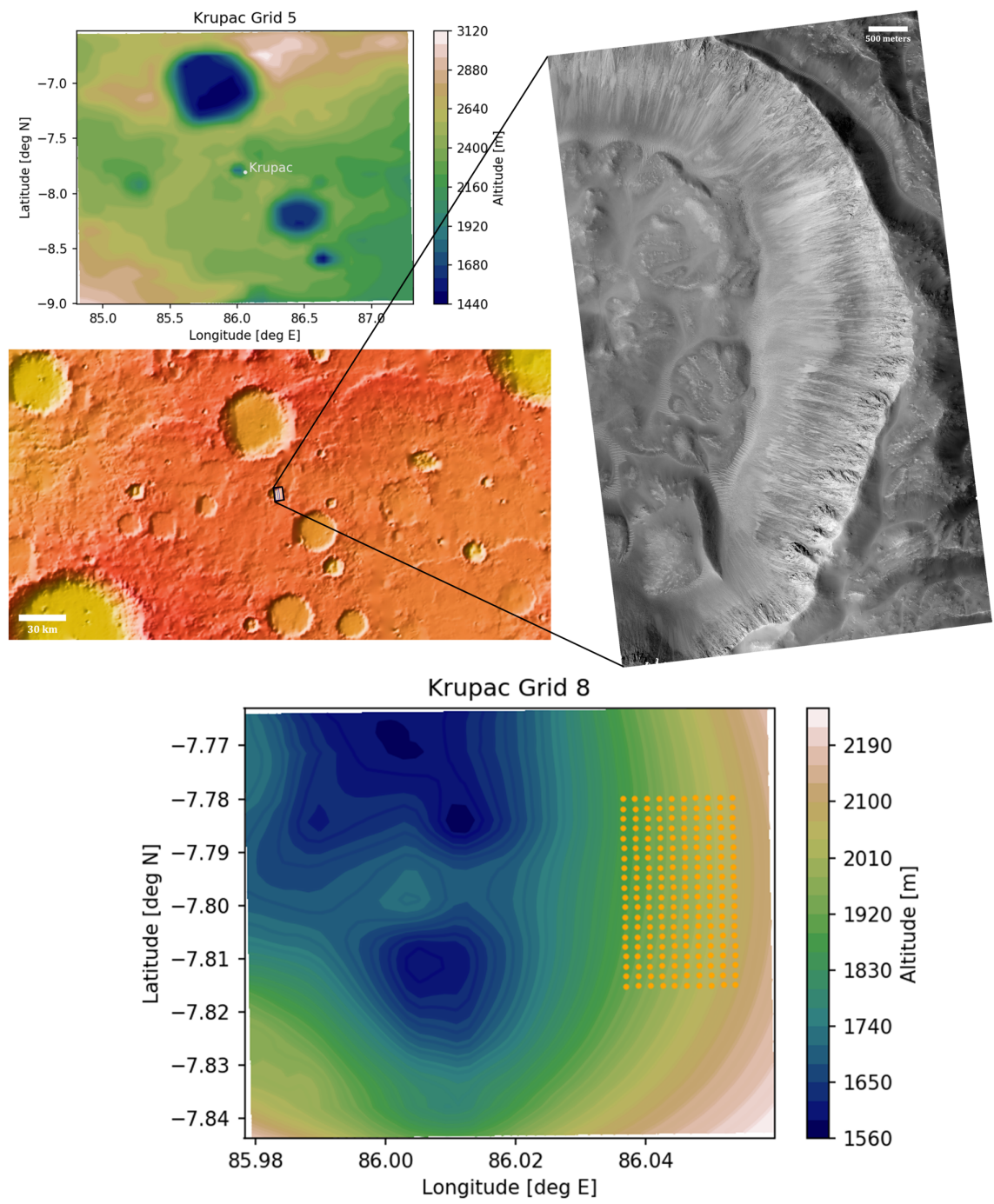


Figure 4.3 RSL site at Krupac Crater (7.803°S, 86.059°E)  
 (a) MRAMS grid 5 model configuration. (b) MOLA color-coded elevations, with HiRISE stamp in blue outline. (c) HiRISE image ESP\_057044\_1720. (d) MRAMS grid-8 model configuration showing grid points used for analysis.

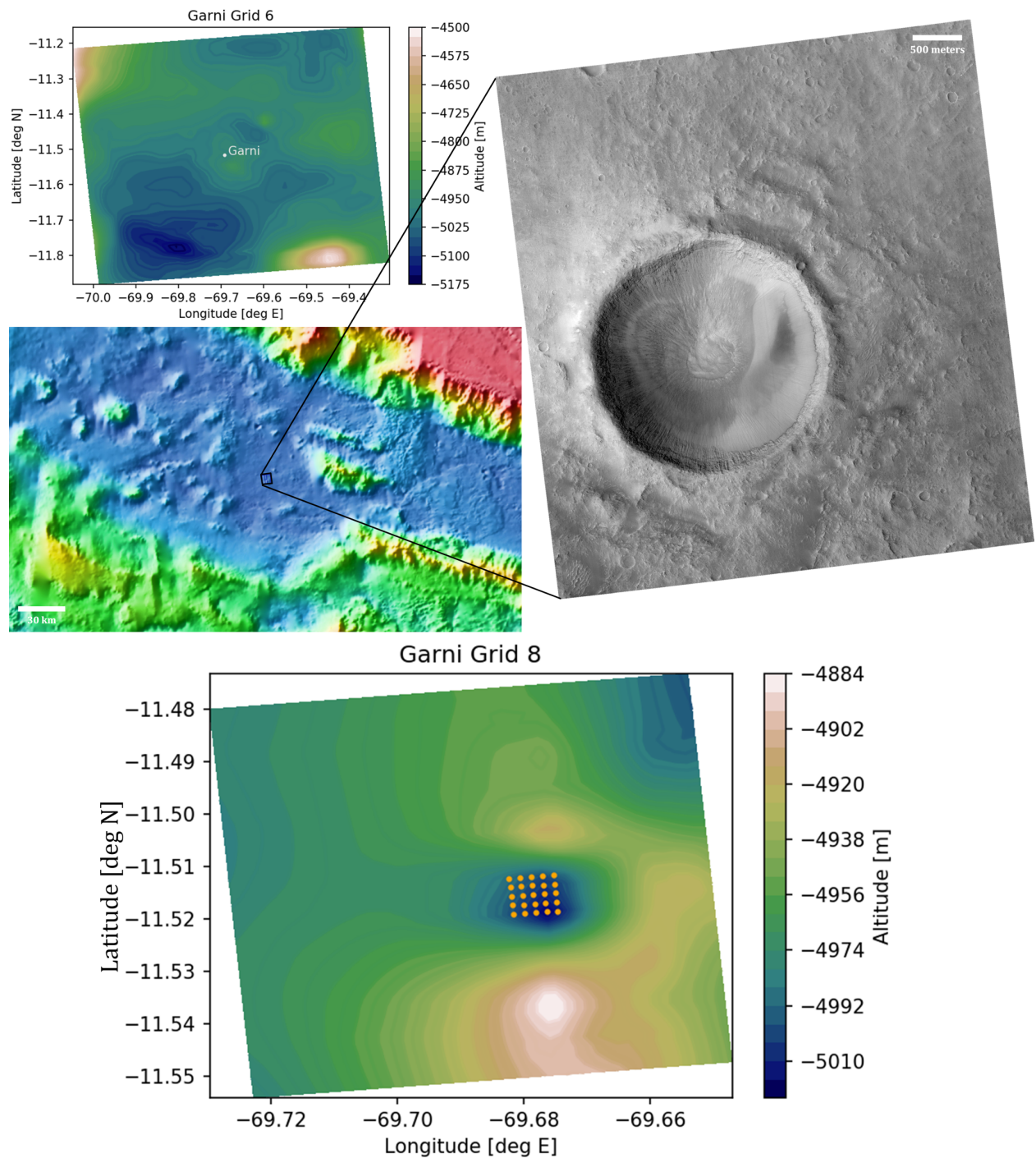


Figure 4.4 RSL site at Garni Crater ( $11.516^{\circ}\text{S}$ ,  $290.308^{\circ}\text{E}$ )

- (a) MRAMS grid 6 model configuration. (b) MOLA color-coded elevations, with white box around Garni crater. (c) HiRISE image ESP\_049375\_1685. (d) MRAMS grid-8 model configuration showing grid points used for analysis.

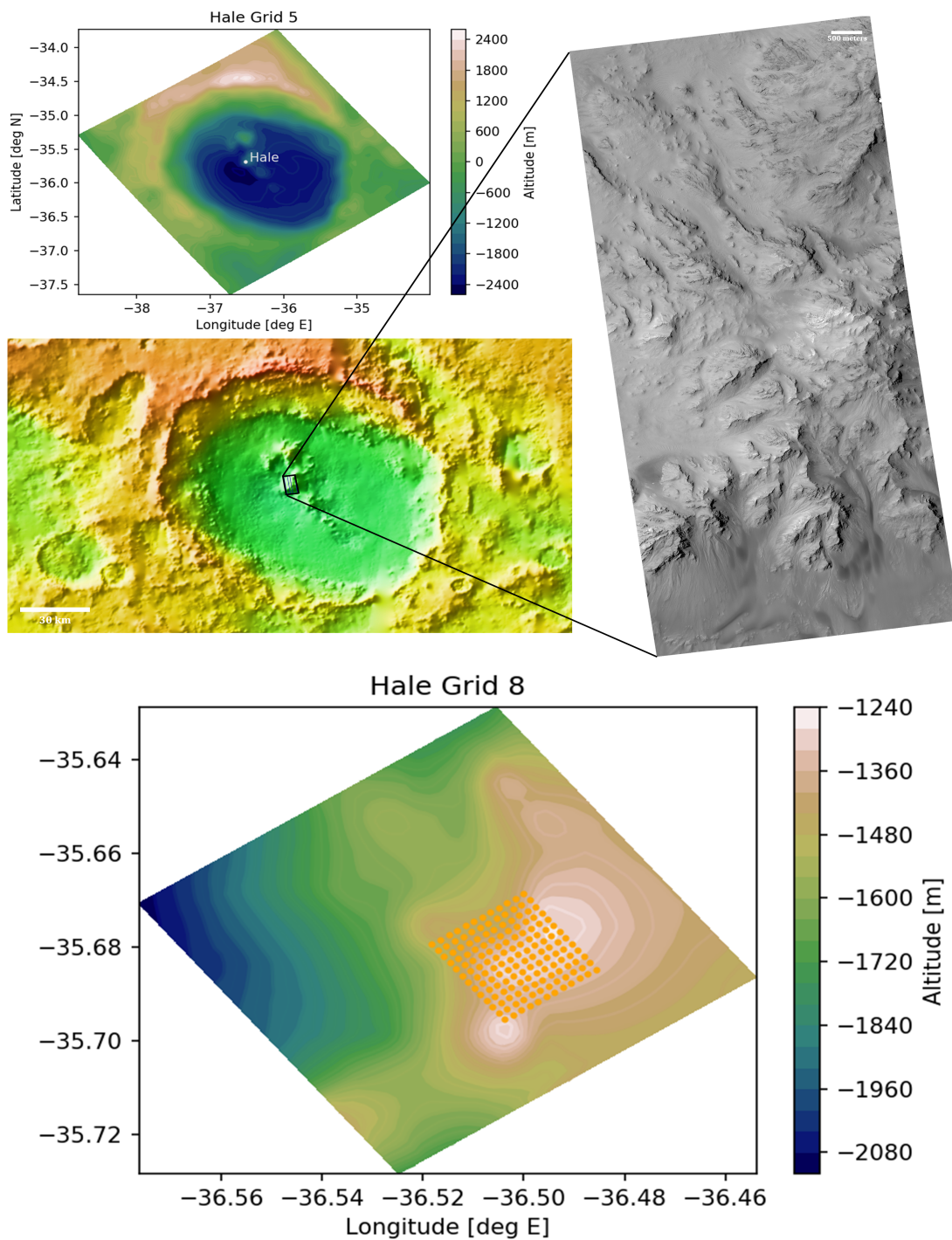


Figure 4.5 RSL Site at Hale Crater ( $35.682^{\circ}\text{S}$ ,  $323.484^{\circ}\text{E}$ )  
 (a) MRAMS grid 5 model configuration. (b) MOLA color-coded elevations, with white box around Garni crater. (c) HiRISE image ESP\_031203\_1440 (d) MRAMS grid-8 model configuration showing grid points used for analysis.

#### 4.2.2 Chlorine-Bearing Salts

A number of candidate oxychlorine and chloride salts may be actively participating in deliquescence on the surface of Mars. Potential candidates include sodium perchlorates and chlorides, magnesium perchlorates and chlorides, as well as calcium perchlorates and chlorides. Laboratory experiments determining the phase diagrams for a range of different salts (Gough et al., 2016; Hanley et al., 2015; Nuding et al., 2014; Wang et al., 2019) show that calcium perchlorate ( $\text{CaClO}_4$ ) has amongst the widest range of temperatures and relative humidity where deliquesce is possible under Mars conditions. Its low eutectic temperature allows deliquescence to occur at the lowest temperatures and lowest relative humidity compared to other salts such as  $\text{CaCl}_2$ ,  $\text{MgClO}_4$ , and  $\text{MgCl}_2$ , as illustrated by comparing the phase diagrams of four Cl-bearing salts in figure 4.6. For our study, we consider the likelihood of deliquescence of calcium perchlorate since we are interested in constraining an upper limit for water extracted from atmospheric vapor under the most favorable conditions and predicting the greatest range of times that are advantageous for deliquescence. The amount of water deliquesced onto calcium perchlorate represents the most optimistic volumes, and higher quantity of deliquesced liquid would not be expected by considering the other candidate Cl-bearing salts.



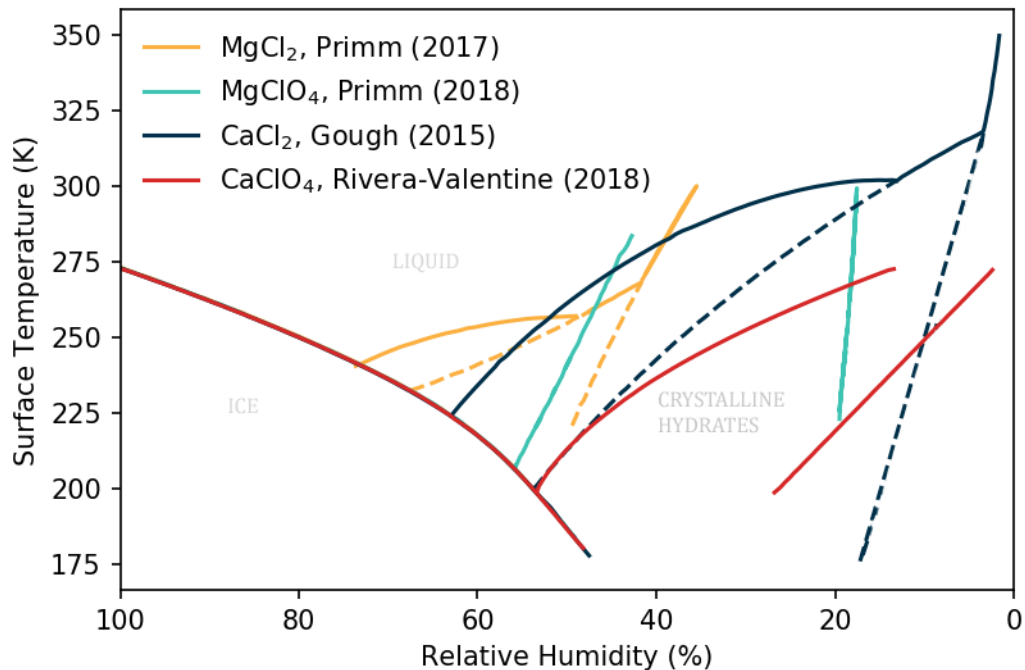


Figure 4.6 Phase diagrams of four Cl-bearing salts including magnesium chloride (Primm et al., 2017), magnesium perchlorates (Primm et al., 2018), calcium chloride (Gough et al., 2016), and calcium perchlorate (Rivera-Valentín et al., 2018). The three general phases are labeled with solid lines indicating stable phase transition boundaries, while dash lines represent metastable transition boundaries.

### 4.2.3 Seasonal Temperatures and Water Vapor Abundances

The regional water distributions at each of the four study sites are influenced by mechanisms operating at the synoptic scale, and should be understood in the context of the Martian global water cycle. The Martian atmosphere is near its driest at the start of northern spring equinox while water is locked up in the north polar ice cap. As the season progresses, the warming of the northern cap and subsequent sublimation of water vapor at high northern latitudes doubles the amount of water vapor in the atmosphere (M. D. Smith, 2002).

Summertime extraction of water from the polar region leads to the gradual propagation of water towards the equator, increasing water vapor mixing ratios in the northern mid-latitudes, while the cross equatorial transport of water via the Hadley circulation transports water to the southern hemisphere. Column water vapor in the northern mid-latitudes peaks  $\sim L_s 130^\circ$ , while the equatorial region peaks slightly later close to  $L_s 170^\circ$  and maintains a moderate amount of vapor in the atmospheric column well into mid-northern winter. Meanwhile, water in the south is locked up at the polar ice cap beneath a permanent  $\text{CO}_2$  cover due to colder temperatures in the south. Water vapor column abundance in the southern hemisphere peaks around  $L_s \sim 290^\circ$ , however the maximum amount corresponds to only half that of the peak in the northern hemisphere. Furthermore, the stronger Hadley cross-equatorial circulation during southern summer forces water back to the northern hemisphere where water preferentially resides. These seasonal trends in column atmospheric vapor should be taken into account when considering atmosphere vapor as a potential source of volatile for deliquescence.

The seasonal variability in surface temperature and column precipitable water vapor observed by the Thermal Emission Spectrometer (TES) (M. D. Smith, 2002, 2004) is shown in figure 4.7 for each of the four study RSL sites. Given the Mars Global Surveyor's (MGS) sun-synchronous orbit, TES surface temperature observations are available near 02:00 and 14:00 local time (LT), while column vapor mixing ratio is available at 14:00 LT. The TES datasets for surface temperatures and water vapor abundances from Mars Year 26 are binned into  $3^\circ$  latitude by  $7.5^\circ$  longitude bins every  $5^\circ L_s$ . The TES total column water vapor

values used derives from the binned climatology data by Smith (2004), which is not normalized to 611 Pa. Located in the northern mid-latitudes, Rauna Crater is the only site we examined in the northern hemisphere. A column water vapor abundance of  $\sim 10$  pr- $\mu\text{m}$  during early northern spring ramps up to its annual peak of 30 pr- $\mu\text{m}$  at  $L_s = 140^\circ$ , then drops down to below 10 pr- $\mu\text{m}$  throughout northern fall and into northern winter. TES data also shows a slight increase  $\sim L_s = 285^\circ$ . The water cycle for the remaining three RSL sites throughout the southern hemisphere share similar seasonal trends in the rise and fall in water vapor column abundances. The atmosphere remains dry throughout southern fall and winter, but humidity rises around  $L_s = 150^\circ$  peaking shortly after southern spring equinox prior to gradually dropping back to the wintertime minima. Hale Crater lies in the southern mid-latitudes and represents the southern-most RSL site in our study. The seasonal trend at Hale Crater contains a deep minimum of only 1 or 2 pr- $\mu\text{m}$  throughout southern fall and winter, and reaches a maximum just shy of 10 pr- $\mu\text{m}$ . While Krupac Crater and Garni Crater are both situated slightly south of the equator at comparable latitudes, the elevations are very different and the water column at Garni Crater is slightly higher throughout the year due to its location on the floor of the Valles Marineris canyon system. Krupac Crater reaches a maximum of  $\sim 13$  pr- $\mu\text{m}$  at  $L_s = 180^\circ$  while Garni Crater peaks at 16 pr- $\mu\text{m}$  around the same time. While the broad characterization of the global water cycle above is described with respect to column precipitable water vapor, our objective to determine the most favorable surface conditions for deliquescence is most affected by the temperature and water abundances in the boundary layer closest to the surface.



While CRISM column abundances of H<sub>2</sub>O are not directly used for this study, nevertheless they are useful as a comparison to the TES water vapor column abundances. At the Garni Crater location in Valles Marineris, CRISM measurements of ~3 pr- $\mu\text{m}$  at  $L_s = 90^\circ$  and ~12 pr- $\mu\text{m}$  at  $L_s = 180^\circ$  are comparable to TES' measurements of ~5 pr- $\mu\text{m}$  at  $L_s = 90^\circ$  and ~12-16 pr- $\mu\text{m}$  at  $L_s = 180^\circ$ . In contrast, CRISM data shows the H<sub>2</sub>O column steadily rises to an abundance of 12pr- $\mu\text{m}$  at  $L_s = 220^\circ$ , compared to TES' peak of ~16 pr- $\mu\text{m}$  earlier in the season at  $L_s = 190^\circ$ . Both instruments consistently show water vapor column dropping to 8 pr- $\mu\text{m}$  by  $L_s = 280^\circ$ . Whereas the comparison between CRISM and TES at Garni Crater are similar within CRISM errors, larger discrepancies between the two instruments are seen at Hale Crater in the southern mid-latitude. For TES, the southern hemispheric location shows a sharp increase in water vapor column between  $L_s = 150^\circ$  to  $210^\circ$ , peaking at a maximum value of 8 pr- $\mu\text{m}$  at  $L_s = 210^\circ$ . It is then followed by a very gradual fall to 5pr- $\mu\text{m}$  at  $L_s = 350^\circ$ , and finally reaching the annual minimum at  $L_s = 50^\circ$ . For CRISM, the vapor column annual trend has a much narrower peak that happens later in year. Available data begins at  $L_s = 180^\circ$  with 3.5 pr- $\mu\text{m}$ , rising to peak of 14pr- $\mu\text{m}$  at  $L_s = 260^\circ$ , and dropping to 5 pr- $\mu\text{m}$  by  $L_s = 350^\circ$ . CRISM measurements are binned by 5 degrees in longitude, 2 degrees in latitude, 30 degrees in  $L_s$ , and is normalized to a reference 6.1 mbar pressure surface (Toigo et al., 2013), whereas the TES dataset used in our study is not scaled to a reference pressure surface. Thus, the absolute values of column water vapor abundances do not represent a one-to-one comparison between the two instruments. However, it is still useful to look at the trends in water vapor behavior, and at which season the column peaks throughout the year.

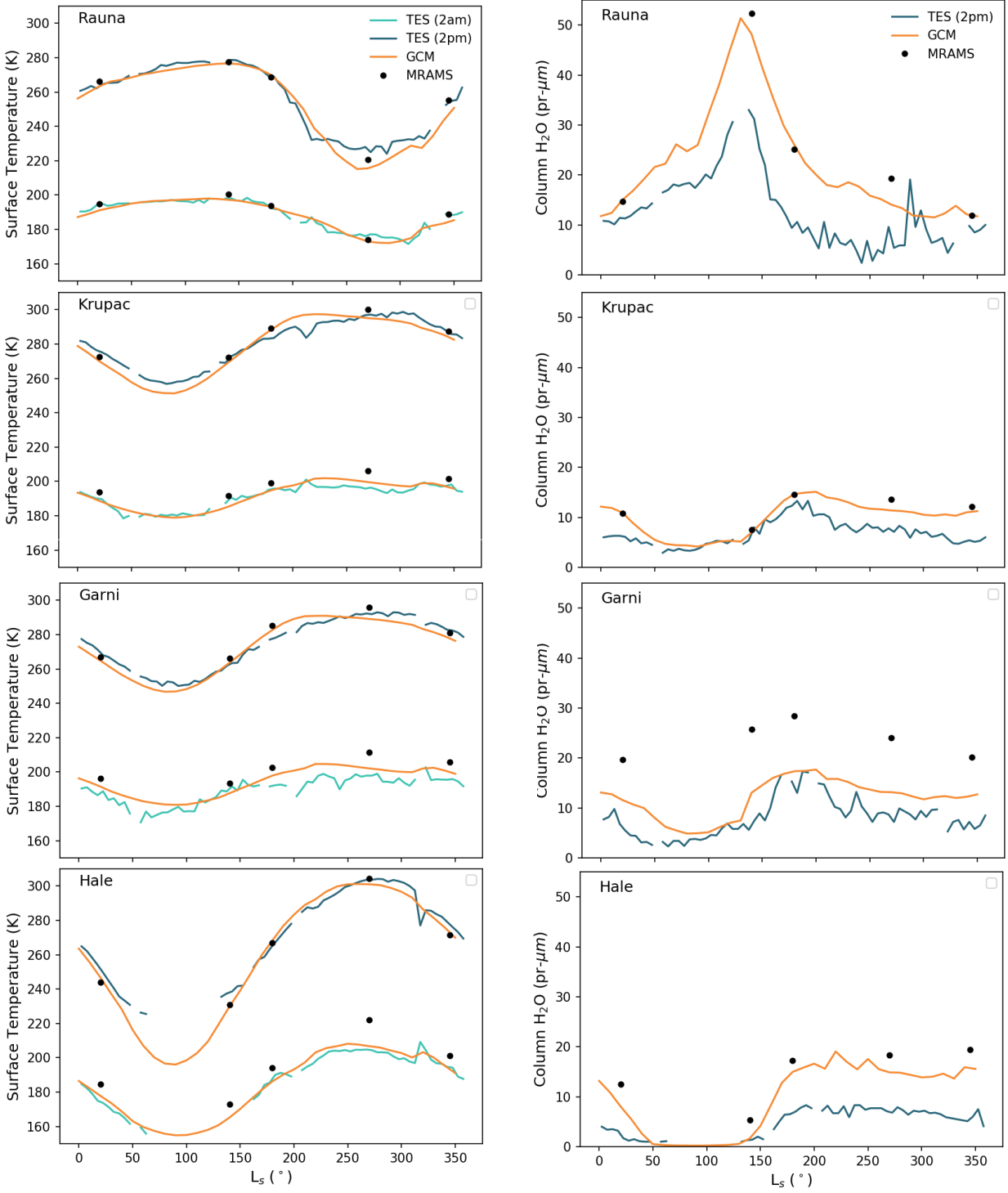


Figure 4.7 . TES versus model comparison for surface temperature and column water at the four RSL study sites (Rauna, Krupac, Garni, and Hale Crater). TES surface temperatures are obtained at 0200 and 1400 local time, whereas column water vapor abundances are only available at 1400. MGCM model outputs are given by the orange

curves. Mesoscale output at the five seasons modeled in this study are shown as black dots. The discrepancy in column water vapor modeled by MRAMS compared to TES and the MGCM appears especially large since Garni Crater lies inside Valles Marineris, which neither the GCM or TES footprint is able to resolve.

Modeled temperatures and water abundances, in the GCM as well as from MRAMS are compared against observed values by TES to evaluate the precision of the modeled quantities. Local variability is expected across the RSL regions of interest. TES' spatial footprint measuring (9 km across track (east–west) by 10–20 km along track (north–south) (M. D. Smith, 2004) is much greater than MRAMS' resolution, which is four times the innermost grid spacing of 100 m. In lieu of higher resolution measurements of near-surface water vapor at our study locations, TES column precipitable water still represents the most appropriate water vapor input for this work. Binned TES values are interpolated to the latitude, longitude, and  $L_s$  of interest for comparison with modeled quantities. A comparison of TES, MGCM, and MRAMS temperature and column water vapor shows that the models typically follow the trends in TES observations (Fig. 4.7). Modeled surface temperatures fall within observational errors, while the amount of water vapor in the column predicted by the models tends to be high compared to observations. It is important to note that as MGCM results are used as boundary and initial conditions for the MRAMS runs, water mixing ratios in MRAMS are inherited from the GCM and reflect the tendency of the model to be generally wetter compared to TES.

To keep water vapor mixing ratios in our analysis consistent with observed values, we define a bias correction factor by taking the ratio between MRAMS and TES column water

values at each location and season of interest. This adjustment factor is applied to the post-processed MRAMS output in order to match TES column vapor within errors. The H<sub>2</sub>O mole fractions in the MRAMS results are scaled downward because of the mismatch between the GCM and observations. We acknowledge that while it would be more ideal to scale the initial GCM input to MRAMS rather than applying a H<sub>2</sub>O scaling to the mesoscale results, the appropriate scaling factor would need to be determined via an iterative process from a series of MRAMS simulations. Mesoscale simulations are computationally expensive and due to resource restrictions, it was determined that it would be most efficient to apply the correction factor to the MRAMS output.

To further optimize computational resources, microphysical processes such as sedimentation and nucleation have been excluded from our simulations. In the absence of nucleation, it is possible for our modeled atmosphere to be supersaturated, reaching relative humidity greater than 100% in lieu of the formation of cloud condensates. Preliminary model results comparing simulations which included microphysics versus those without showed that surface temperatures and near-surface water vapor concentrations were not significantly impacted by the inclusion of cloud processes and the generalized results of this study would not be greatly affected. Typically, the inclusion of microphysics in MRAMS enables atmospheric water vapor in excess of saturation to form water ice clouds, capping relative humidity at or very near 100%. However, given our decision to scale the post-processed MRAMS water concentration to observed TES abundances due to computational resources availability, the inclusion of condensates would have presented several additional complications. In the case when cloud microphysics is included, the application of a bias

correction to the fraction of water in the vapor phase to match TES observations would not represent an appropriate adjustment of the total water contained in the system given the interplay between water in the vapor and condensate phases. A simple scaled factor would fail to account for the portion of water present as clouds that would have sublimated to compensate for the reduction in vapor during the scaling. When the resulting MRAMS water vapor is scaled in a simulation that included cloud microphysical processes, the diurnal relative humidity distribution with respect to surface temperature becomes skewed. It can be seen that the initial, unscaled diurnal surface temperature curve as a function of relative humidity is confined below 100% relative humidity. Furthermore, for a period of time in the morning, the temperature and relative humidity conditions falls within the liquid portion of the phase diagram thus allowing for a period when deliquescence is possible. However, after the water vapor is scaled in this microphysics simulation, the maximum relative humidity the diurnal curve reaches is only 50%, and the possibility for deliquescence is no longer indicated. In reality, the relative humidity would have readjusted itself to a higher value as a portion of the cloud condensate would sublime into water vapor. Given these considerations, the decision to apply the bias correction to the MRAMS output necessitated simulations for our experiments be conducted with cloud microphysical processes turned off. In another preliminary experiment when deliquescence is indicated for both the microphysics and non-microphysics case, we found that the relative amount of H<sub>2</sub>O of 0.0445  $\mu\text{m}$  and 0.12  $\mu\text{m}$  for the cloud vs no cloud case respectively. Although the results differ by a factor of greater than two, the absolute amount of H<sub>2</sub>O is still very small compared to RSL water budget estimates. However, since the objective of this study is to investigate the

volumes of water the atmosphere can supply, the exclusion of microphysical processes in our simulations is not expected to significantly affect the basic objective of this study.

## **4.3 Results**

### **4.3.1 Regional Results at Four RSL Sites**

Surface temperature and water vapor concentration are used as the primary prognostic variables to determine the surface stability of calcium perchlorate brines as well as the timing for when deliquescence may occur. Water vapor mixing ratio is evaluated at the lowest mesoscale model atmospheric level 7 meters above the ground. Given that vertical heat and momentum fluxes are almost independent of height varying less than 10% of the mean magnitude within the surface layer (Stull, 1988), the near surface water vapor mixing ratio at 7 meters can be taken as a sufficient approximation of the value at the surface. In the following sections, we will first describe the full analysis sequence at Krupac Crater during  $L_s = 20^\circ$ , followed by the seasonal variability at Krupac Crater, ending with the key results for all the seasons at the three subsequent RSL study sites.

#### **4.3.1.1 Krupac Crater $L_s = 20^\circ$**

The diurnal cycle of surface temperature and water vapor concentrations are evaluated to assess when conditions for the stability of deliquesced liquid are met. Using the MRAMS simulation output from the grid-8 domain, a spatial average of temperature and water vapor is taken over grid points of interest at the RSL site as specified in figure 4.3e. For

Krupac Crater, 200 model grid points are used covering the eastern region of the crater where are RSL are observed. The grid-8 mesoscale model domain offers high enough spatial resolution necessary to capture the variability within Krupac Crater, reflecting the topography of the crater and the effects of slopes on ventilation patterns. Slight local temperature variations of two to three degrees exists across different illuminated portions of Krupac Crater (Fig. 4.8b) and water vapor mixing ratios variations of  $\sim 3\%$  can be seen throughout the area of interest (Fig. 8d). This can be compared to the grid 5 domain (Fig. 4.8a & c), where only two model grid points span across the entire diameter of the crater. Note that even at the grid-8 model domain, the area the model represents after spatial averaging is a few kilometers across. This study does not attempt to simulate each individual RSL, but instead is looking at the local scale environment that captures a bunch of RSL.

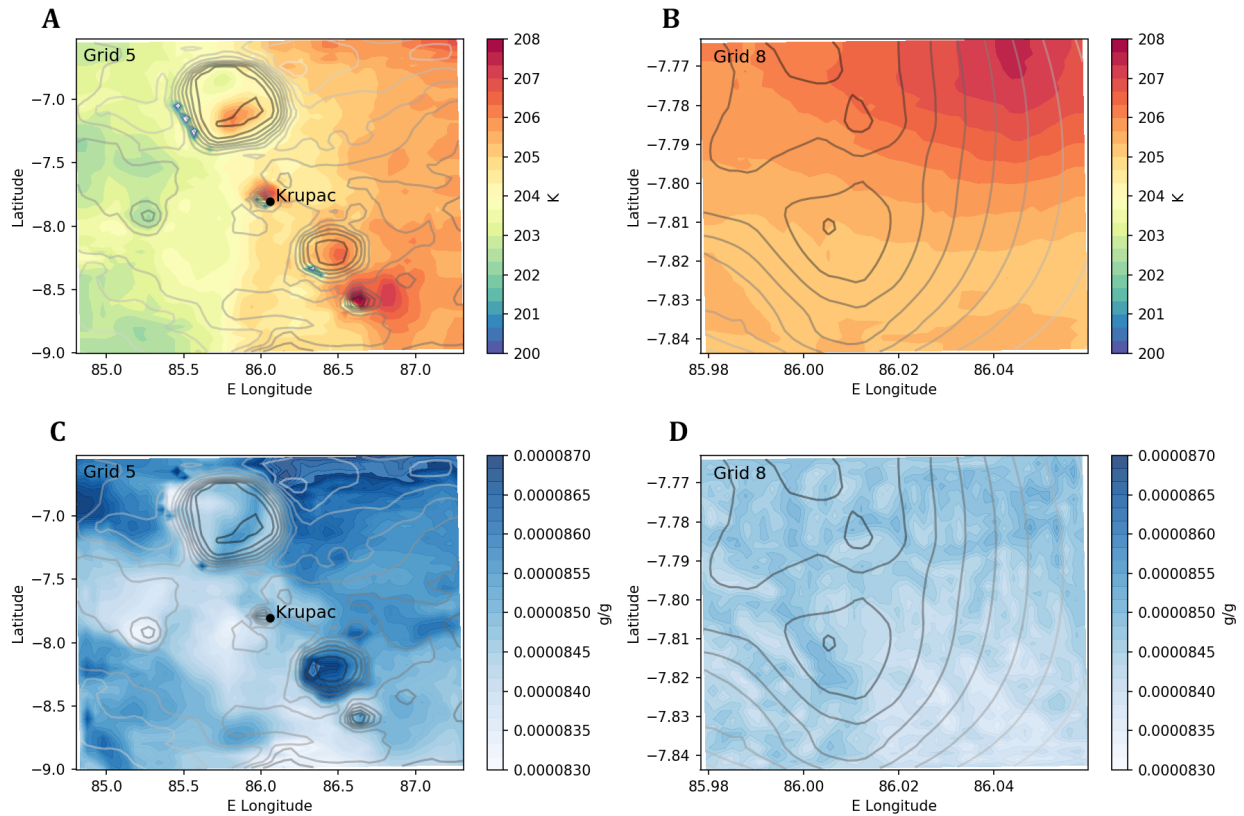


Figure 4.8 Medium resolution (grid 5) versus high resolution (grid-8) MRAMS results of surface temperature and near-surface water vapor mixing ratio at Krupac Crater during  $L_s = 20^\circ$  at 0800 LT.

Over the grid points of interest, a 10-sol average taken over the duration of the simulation is used to find the resultant diurnal cycle of surface temperature, near-surface water vapor mixing ratio, as well as relative humidity (Fig. 4.9). Shaded regions represent one standard deviation from the mean in spatial and temporal variability. Mean surface temperature at Krupac Crater at  $L_s = 20^\circ$  varies from a minimum of 190 K to a mid-afternoon maximum of 268 K. Diurnal temperature swings of nearly 80 K is typical in Martian conditions where the heat capacity is low compared to the Earth. Near-surface water vapor concentrations reach a minimum of  $2 \times 10^{-5}$  kg/kg at the time of the temperature minimum,



and increases by a factor of four at its maximum near 1700 LT. The uncertainty in water vapor concentrations is greater during the mid-afternoon reflecting the uncertainty in TES observations. Relative humidity is calculated with respect to saturation vapor pressure over pure liquid water. Although water vapor mixing ratios peak during mid-afternoon, relative humidity is much more sensitive to variabilities in temperatures, and thus maximum relative humidity values overnight and in the early morning are governed primarily by the local times when temperatures are the lowest.

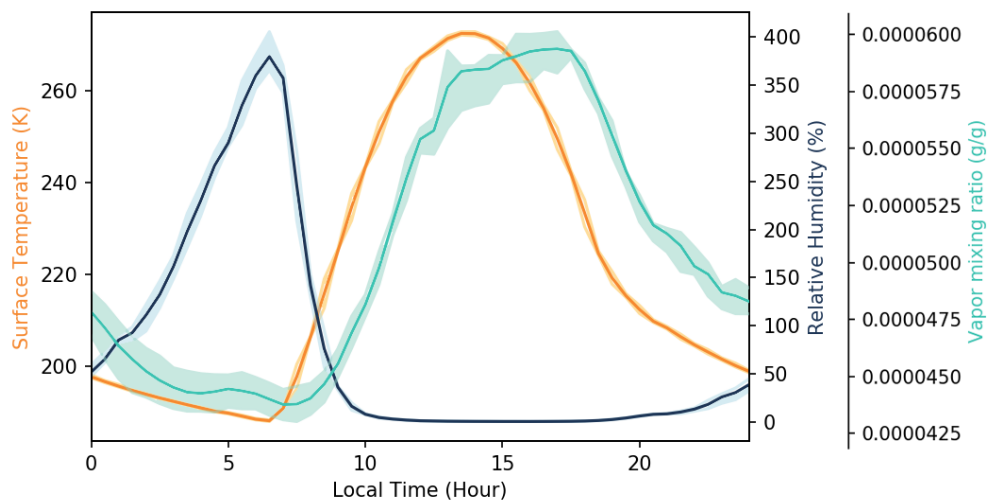


Figure 4.9 Diurnal cycle of surface temperature, relative humidity, and water vapor mixing ratio at Krupac Crater during  $L_s = 20^\circ$ . Diurnal curve represents a 10-sol average. Shading shows model output one sigma from the mean value.

Diurnal variability in water vapor flux is calculated assuming water vapor in the atmosphere is transported to the surface by turbulence, which represents one of the most efficient methods to deliver water to the surface. Vapor pressure at the lower boundary is set to zero such that that the surface layer is assumed to be an infinitely absorbing sponge.

Once deliquescence initiates, atmospheric water is further assumed to be replenished immediately. This method of calculating the water vapor fluxes is optimistic by design to probe at the maximum amount of water that can be supplied to the surface by the atmosphere. The resulting diurnal flux as shown in figure 4.10. Flux from the atmosphere into the surface is at a maximum in the ~1500 LT because turbulence is greatest typically in the mid-afternoon. Keeping the surface layer completely dry represents the most optimistic case and should provide an upper limit for the water budget available from an atmospheric point of view. In addition, this study assumes that all available atmospheric water interacts with the surface via deliquescence only. In reality, the diurnal of exchange of water vapor with the surface also occurs through the adsorption of water vapor onto soil grains, which would limit the quantity of atmospheric water available solely for deliquescence.

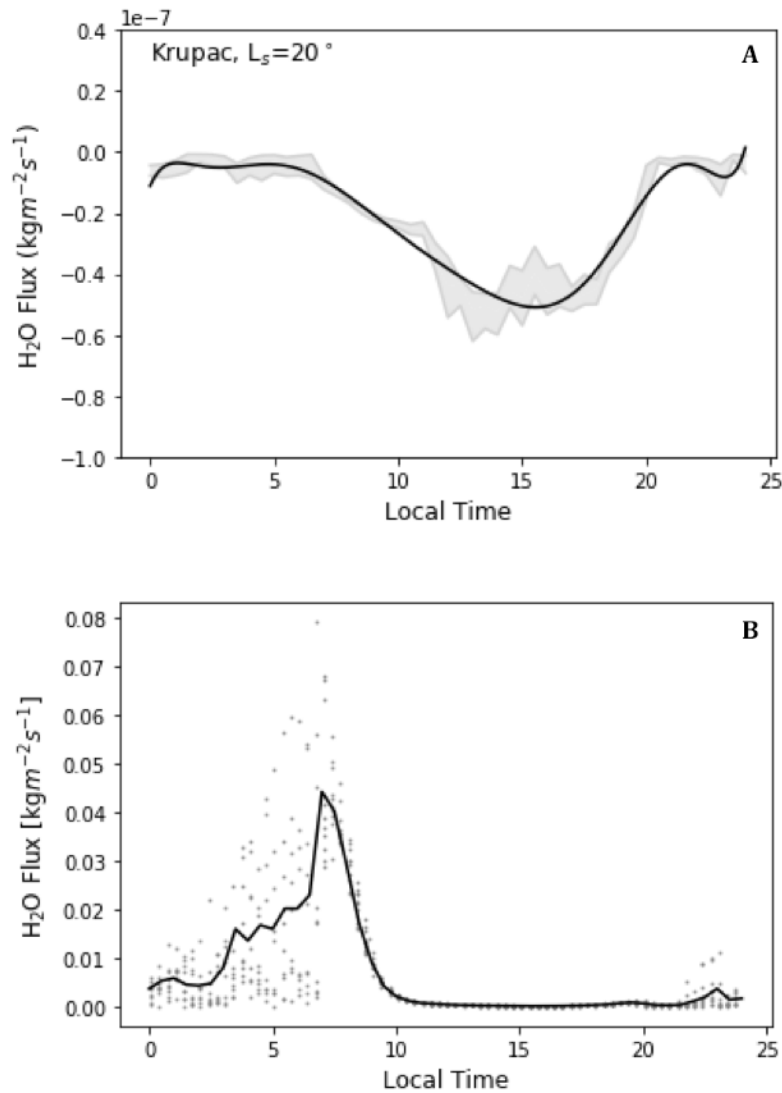


Figure 4.10 Diurnal H<sub>2</sub>O flux ( $\text{kg m}^{-2} \text{s}^{-1}$ ) used in the model (a) based on the assumption that the surface is an infinite sponge layer. (b) based on the assumption that the vapor mixing ratio at the surface layer is equal to the saturation vapor pressure. The black curves are fitted to the modeled turbulent flux in gray.

Flux calculations used in this study assumes that the water vapor mixing ratio at the surface is zero. This surface represents an infinite sponge layer at the lower boundary, thus ensuring that that flux is always negative drawing vapor from the atmosphere into the

ground. The case of an infinite sponge represents the absolute most H<sub>2</sub>O available for deliquescence. Doing so enables our result to find the highest amount of water vapor that can be extracted from the atmosphere onto the deliquescing salt. For a more realistic scenario, we also determine the diurnal water vapor flux by setting water vapor at the surface equal to the saturated vapor pressure. The resulting diurnal flux allows movement of water vapor into and out of the surface layer depending on the time of day (Fig. 4.10b). When the saturation vapor pressure is used instead of an infinite sponge, flux could be out of the ground indicating that the surface layer would actually be expelling water into the atmosphere.

One experiment showed that the resulting amount of deliquesced liquid for the original case of an infinite sponge layer was 0.0608  $\mu\text{m}$  whereas when the surface layer was set to the saturation vapor pressure, the result would cause an expulsion of 46056  $\mu\text{m}$  of vapor from the surface into the atmosphere over the duration of 47.7 minutes. However, this scenario is unrealistic as it assumes that the water at the surface layer is constantly replenished during this time, such that the vapor mixing ratio remains at the saturated vapor pressure. In this case, because the atmosphere was sub-saturated while the surface layer is saturated during times when the temperature and relative humidity could allow for deliquescence, vapor from the surface layer transforms to the liquid phase which subsequently enables the flux of vapor from the surface into the atmosphere. This is an interesting comparison to the infinite sponge layer scenario, however the shape of the diurnal flux absorption model is still not representative of the actual diurnal flux on Mars as modeled by Savijärvi et al. (2016), where the direction of surface flux during the early

morning hours between ~06:00 to 10:00LT is expected to reflect the absorption of vapor from the atmosphere into the ground as the surface layer is desiccated during this period.

Calcium perchlorate's low eutectic point and highly deliquescent properties allows it to form aqueous solutions at temperatures as low as 197 K at a relative humidity of 55% (Nuding et al., 2014; Pestova et al., 2005; Rivera-Valentín et al., 2018). At higher temperatures between  $277 \text{ K} \leq T \leq 283 \text{ K}$ , the relative humidity necessary drops to  $13\% \leq \text{RH} \leq 17\%$  (Ferris et al., 2017). These temperature ranges fall well within conditions found on the Martian surface. However, whether deliquescence occurs and when it may be occurring depends on when the appropriate relative humidity and temperature conditions are simultaneously satisfied. The necessary combination of moderate relative humidity paired with sufficiently low temperatures typically only occur in the early morning when temperature is increasing as the relative humidity falls, or in the evening when temperature drops and relative humidity rises.

Simulations at Krupac Crater at  $L_s = 20^\circ$  (Fig. 4.11) show that local temperature and relative humidity conditions may support deliquescence for several hours during the early morning local time. Deliquescence occurs when a substance absorbs sufficient water to form an aqueous solution, while efflorescence involves the conversion of a hydrate into its anhydrous form as the solvent in which the substance is dissolved evaporates, leaving behind a coating of the salt. The deliquescence relative humidity (DRH) and efflorescent relative humidity (ERH) curves for calcium perchlorate are derived from lab work by Rivera-Valentine et al. (2018). The blue curve represents the spatially averaged 10-sol diurnal mean of the surface temperature versus relative humidity result from our mesoscale simulation.

The curve forms a continuous arc over the 24-hour period. The portion to the left of the figure is not shown, since relative humidity greater than 100% is an artifact of our simulation since microphysical processes are absent. Under Martian conditions, the lower segment of the diurnal surface temperature vs relative humidity cycle typically corresponds to the evening hours while the upper leg of the curve occurs during the morning. At Krupac Crater during  $L_s=20^\circ$ , deliquescence may be possible when local surface temperature and relative humidity falls within the liquid phase on the calcium perchlorate phase diagram. In this scenario, the blue diurnal curve advances clockwise over the course of the day. The combination of modeled temperature and relative humidity during evening local times never crosses over into the liquid phase, denoting that deliquescent conditions are not met. Meanwhile, the top branch of the blue curve, corresponding to early morning, does intersect with the saturation vapor curve at 08:14 local time, and crosses the deliquescent relative humidity curve and into the liquid phase at approximately 08:22 LT. A hysteresis effect extends the duration for which the deliquesced liquid can remain in a liquid state until local temperature and relative humidity conditions intersects with the ERH curve, which in this case occurs at 09:03 LT. In total, deliquesced liquid is predicted to be stable at this location during this season for a duration of 48.6 minutes. Totaling to an amount equal to 0.0620  $\mu\text{m}$ .

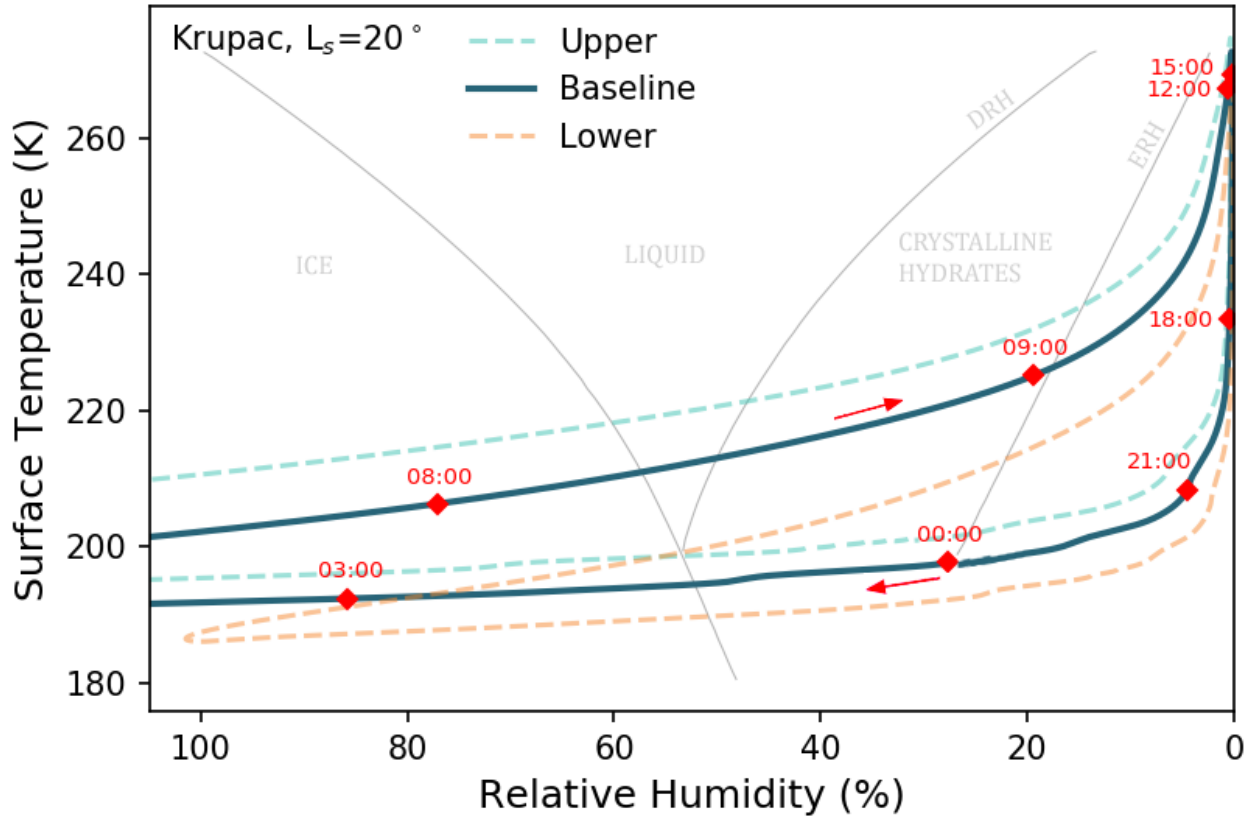


Figure 4.11 Stability diagram for the  $\text{CaClO}_4\text{-H}_2\text{O}$  system at Krupac Crater during  $L_s=20^\circ$ . Overlain by the MRAMS simulated diurnal relative humidity and surface temperature cycle. The dark blue diurnal curve is the baseline scenario modeled by taking a 10-sol mean over a spatial average of the grid-8 grids points as specified in figure 4.3e. The upper and lower range of expected conditions found from a sensitivity analysis are shown as dashed curves. The upper bound is expected for the scenario of +2K in surface temperature & 150% of the baseline  $\text{H}_2\text{O}$  vapor mixing ratio, and the lower bound is expected for the scenario of -2K & 50%  $\text{H}_2\text{O}$  of the baseline values.

We assess the sensitivity of our results to temperature and water vapor errors inherent in the model. Based on our previous experience with MRAMS, reasonable surface temperature uncertainties of  $\pm$  a few degrees kelvins and water vapor uncertainties of  $\pm$  50% can be expected. For the current scenario Krupac Crater at  $L_s=20^\circ$ , increasing surface

temperature by 2K increased the amount of water deliquesced by 4.5% compared to the nominal baseline value while decreasing temperature by 2K increased the amount by 23%. For uncertainties in water vapor, increasing water mixing ratio by 50% increased the amount of deliquesced water by 70%, while decreasing water mixing ratio outputs by 50% decreased the amount of deliquesced water by 48%. For an upper bound of the amount of deliquescence that can be expected, simultaneously increasing the surface temperature by 2K and increasing water mixing ratio by 50% resulted in a total amount of water deliquesced of 0.1021  $\mu\text{m}$ , a 64.6% increase compared to the nominal baseline value of 0.0620  $\mu\text{m}$ . In the lower bound where surface temperature is decreased by 2K and the water mixing ratio decreased by 50%, the diurnal relative humidity-temperature curve falls just barely below the eutectic point in the phase-space so no amount of deliquescence takes place. This sensitivity analysis is carried through to the remaining seasons and RSL sites. Diurnal temperature-relative humidity curves for the upper and lower limits in our sensitivity analysis are depicted by the light blue and orange curves respectively in figure 4.11.

#### 4.3.1.2 Krupac Crater $L_s = 140^\circ, 180^\circ, 270^\circ, 345^\circ$

At Krupac Crater, the timing and duration for when deliquescence is favorable differs from season to season. Conditions favorable for deliquescence at  $L_s = 140^\circ$  occur marginally later in the morning between 06:59 and 07:40 LT for a duration of 41.4 minutes. The amount of water deliquesced during this time amounts to 0.04045 $\mu\text{m}$  (figure 4.12a). Compared to  $L_s = 20^\circ$ , the southern spring equinox ( $L_s = 180^\circ$ ) hosts the next favorable combination of surface temperatures and relative humidity allowing deliquescence to possibly occur for a total of



45 minutes from 06:14 to 06:59 LT, accumulating a total of 0.0605  $\mu\text{m}$  of water from the atmosphere. The sensitivity analysis shows that in the upper limit where surface temperatures were increased by 2K and water vapor is increased by 50%, the diurnal curve at  $L_s = 180^\circ$  intersects the aqueous phase both in the morning from 06:32 to 07:25 LT for 53 minutes, and in the evening from 01:45.5 to 01:50 LT for another 4.5 minutes (Fig. 4.12b). The total amount of water extracted over the duration of one sol is 0.1233  $\mu\text{m}$ . Deliquescence is not predicted during  $L_s = 270^\circ$  or  $L_s = 345^\circ$  for the baseline values of surface temperatures and water vapor mixing ratios (Fig. 4.12c & d). Under the most optimistic conditions of a 2K increase in surface temperatures, and a 50% increase in water vapor mixing ratios compared to baseline conditions, the upper bound of deliquescence at  $L_s = 345^\circ$  yield 0.0674  $\mu\text{m}$  of water. For  $L_s = 270^\circ$ , none of the scenarios within our sensitivity analysis show that deliquescence is possible at any point during the modeled diurnal cycle.

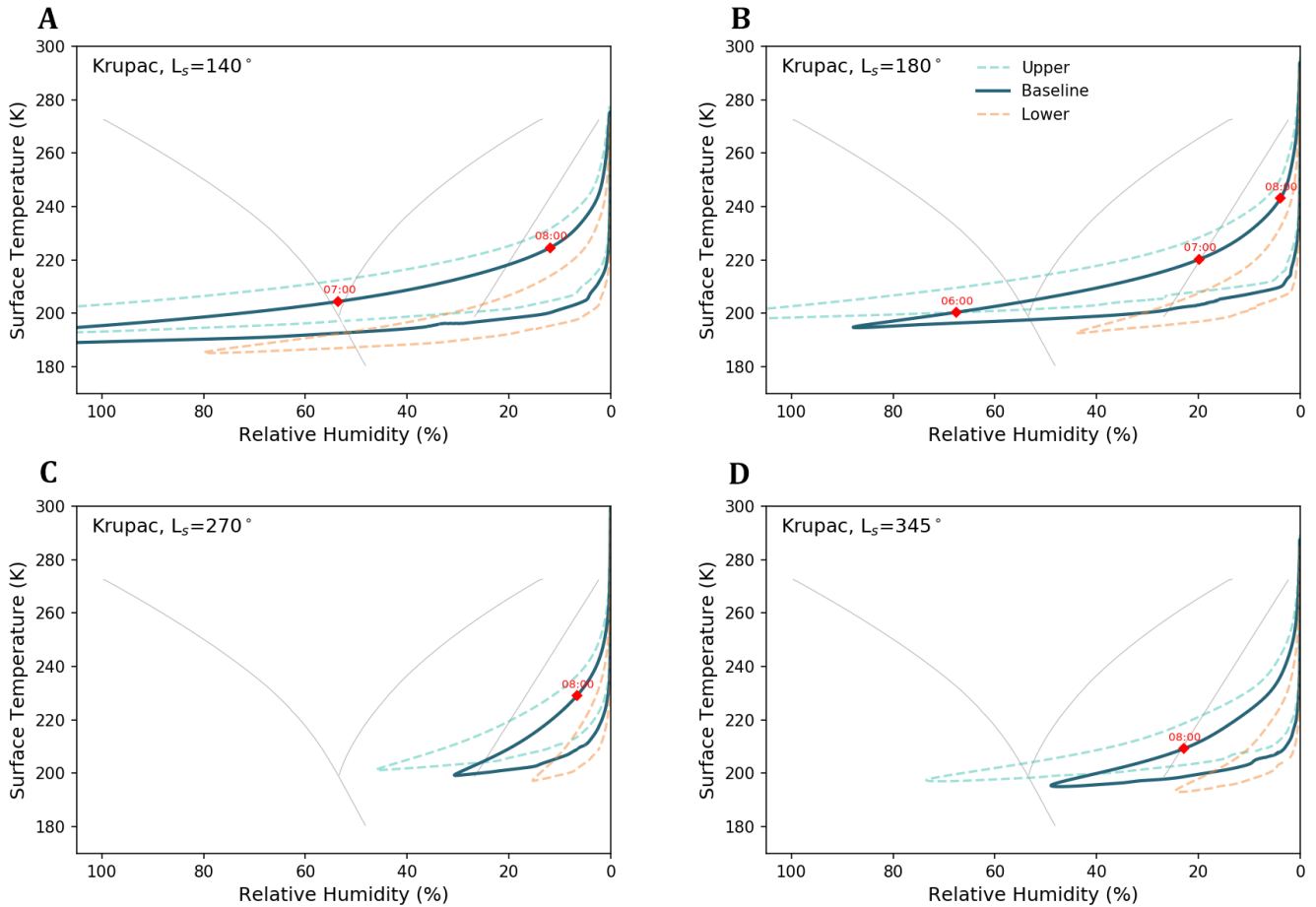


Figure 4.12 Seasonal temperature-relative humidity phase diagram at Krupac Crater for (a)  $L_s = 140^\circ$ , (b)  $180^\circ$ , (c)  $270^\circ$ , and (d)  $345^\circ$ .

#### 4.3.1.3 Rauna Crater, Garni Crater, and Hale Crater

While calcium perchlorate is shown to readily absorb water vapor from the atmosphere and deliquesce into an aqueous solution at all our study locations, the quantity of water extracted from the atmosphere is limited and their seasonality differs with local conditions. In general, our analysis shows that regardless of the latitude of the RSL site, deliquescence occurs much more readily at the beginning of the year, and diminishes

considerably or does not occur at all in the latter part of the year. This is surprising as environmental conditions should be opposite in the northern hemisphere versus the southern hemisphere at any given time of year, with higher temperatures and water vapor content found during summer time, dropping to a minimum during winter time.

A number of simulations show that deliquescence is not observed given modeled temperature and relative humidity fall outside of the range of calcium perchlorates' aqueous phase space for the duration of the simulation (Table 4.2). This is the case for baseline conditions at Krupac during  $L_s = 270^\circ, 345^\circ$ , at Garni during  $L_s = 180^\circ, 270^\circ, 345^\circ$ , and at Hale during  $L_s = 180^\circ, 270^\circ, 345^\circ$ . All three of these sites reside in the southern hemisphere where temperatures and water vapor mixing ratios are low during southern spring and winter. For all of these scenarios, relative humidity remains too low as surface temperature changes throughout the day, as shown by the temperature- relative humidity diurnal curve falling to the right of the deliquescence relative humidity curve at all times of day.

For simulated cases when deliquescence is observed, we find that deliquescence in the south is governed primarily by temperature, while deliquescence in the north is affected most by the availability of water vapor. Deliquescence at sites in the southern hemisphere such as Krupac, Rauna, and Hale Crater, are confined primarily between  $L_s = 0-180^\circ$  for the baseline values of modeled temperature and water vapor. During southern fall and winter, temperatures and water vapor abundances are at their annual minimum. Hale Crater is the southern-most study location, where the atmospheric water content is generally low compared to the northern hemisphere or even equatorial regions. Deliquescence is only predicted for  $L_s = 20^\circ$  and  $L_s = 140^\circ$  for baseline conditions at Hale Crater, where the timing

for deliquescence generally occurs later in the morning compared to other sites, likely due to the dry atmosphere, and high solar incident angle at the southern mid-latitude location. Deliquescence at  $L_s = 20^\circ$  occurs for 70 minutes between 09:05 to 10:15 LT while deliquescence at  $L_s = 140^\circ$  occurs for a similar duration of time 76.5 minutes but starting nearly an hour later with water extraction occurring between 09:57 LT to 11:13 LT. Similarly, water vapor abundances at Krupac and Garni Crater are at a minimum during southern winter near  $L_s = 90^\circ$ . All else being equal, the diurnal temperature variability in the  $L_s = 140^\circ$  simulation dominates the local environment and determines whether conditions are warm enough to allow for a sufficient rise in relative humidity to initiate deliquescence. In contrast, deliquescence in the northern hemisphere appears to be dependent on the availability of water vapor in the atmosphere. Rauna Crater is our only RSL study site in the northern hemisphere, and is the only site that exhibits deliquescence all year round for all five seasons that we explored. Greater seasonal variability in the volume of water extracted is also observed at this location. From the modeled simulations, the highest amount of water extracted from any of our experiments occur during  $L_s = 140^\circ$  where  $1.03 \mu\text{m}$  of water is extricated over a period of 85.2 minutes. This reflects the high abundances of atmospheric water migrating equatorward at his season from the northern polar cap and reaching the northern lowlands where Rauna Crater is located. The scenario at  $L_s = 270^\circ$  presents an interesting case where the diurnal surface temperature versus relative humidity distribution is skewed towards very high relative humidity causing much of the curve to lie beyond 100% relative humidity. As a result, our analysis shows that the amount of water extracted during  $L_s = 270^\circ$  is low, possibly not because of a lack of water vapor, but because of a highly

saturated environment. This may be the result of a model artifact due to the exclusion of microphysical process in the simulations, which does not preclude relative humidity at this season from becoming artificially high. In a realistic scenario, one would expect cloud condensate formation to cause relative humidity to be capped at 100%, provided condensation nuclei are present, thus pushing the surface temperature – relative humidity curve to spend a greater portion of the diurnal cycle within the aqueous phase, thus aiding in a higher amount of deliquesced liquid than simulations suggest. A summary of the simulated range of water extracted from the atmosphere is presented in figure 4.13 for each of the five simulated seasons at the four RSL study sites.

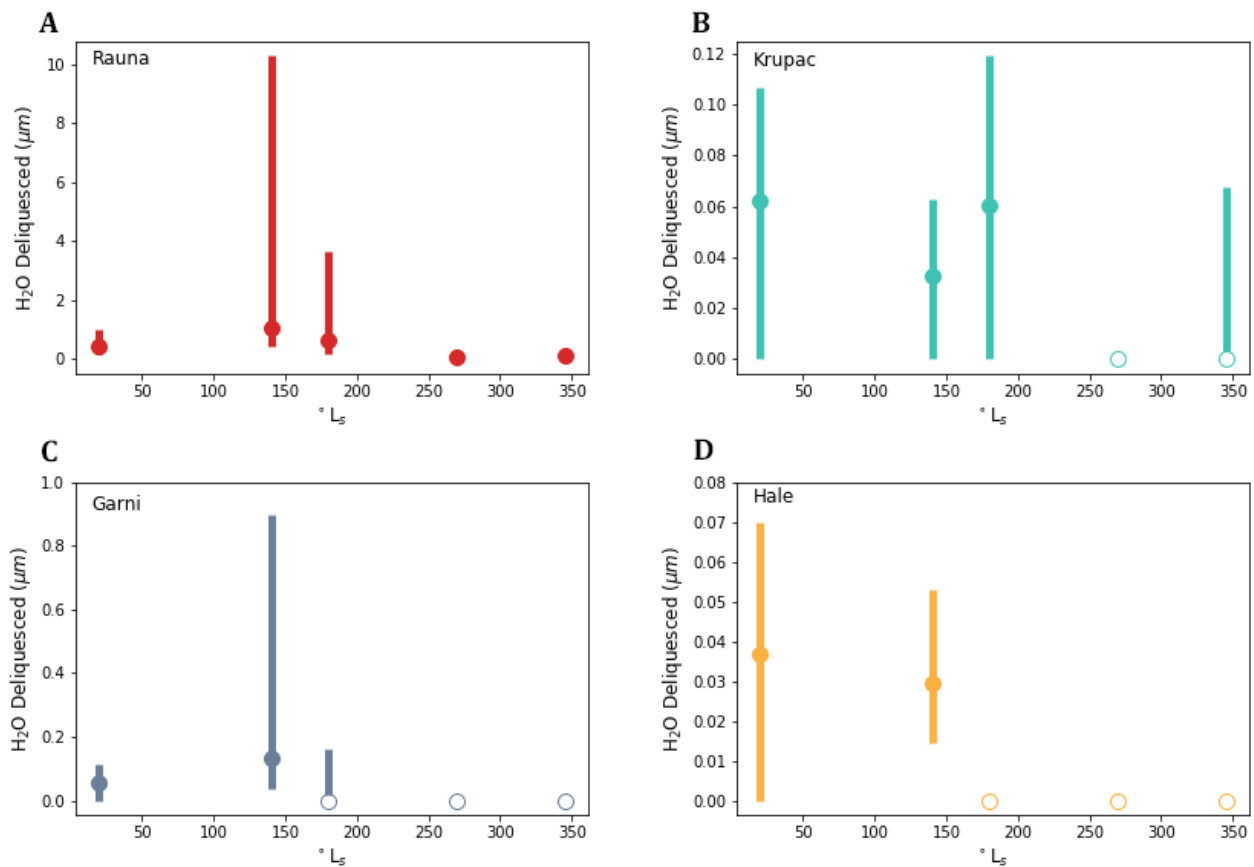


Figure 4.13 Simulated range of water extracted from the atmosphere for the 5 simulated seasons at the Krupac, Rauna, Garni, and Hale Crater RSL sites. Circle indicate the results of the baseline simulation. Solid circles indicate the average amount of water deliquescenced per day, while open circle indicate that no deliquescent is predicted during those seasons. Bars represent the range of possible solutions from the sensitivity analysis.

Site	Ls (°)	Start (LT)	Stop (LT)	Mins	Avg H <sub>2</sub> O flux [kgm <sup>-2</sup> s <sup>-1</sup> ]	H <sub>2</sub> O deliq [μm]
<b>Rauna</b>	<b>20</b>	<i>08:21:18</i>	<i>09:36:00</i>	<i>74.7</i>	<i>-9.98e<sup>-8</sup></i>	<i>0.4471</i>
	<b>140</b>	<i>06:53:24</i>	<i>08:18:36</i>	<i>85.2</i>	<i>-2.03e<sup>-7</sup></i>	<i>1.0311</i>
	<b>180</b>	<i>07:36:18</i>	<i>08:54:36</i>	<i>78.3</i>	<i>-1.30e<sup>-7</sup></i>	<i>0.6089</i>
	<b>270</b>	<i>15:09:54</i>	<i>15:40:30</i>	<i>30.6</i>	<i>-3.96e<sup>-8</sup></i>	<i>0.0728</i>
	<b>345</b>	<i>09:36:00</i>	<i>10:38:06</i>	<i>62.1</i>	<i>-3.63e<sup>-8</sup></i>	<i>0.1351</i>
<b>Krupac</b>	<b>20</b>	<i>08:14:06</i>	<i>09:02:42</i>	<i>48.6</i>	<i>-2.13e<sup>-8</sup></i>	<i>0.0620</i>
	<b>140</b>	<i>06:58:30</i>	<i>07:39:54</i>	<i>41.4</i>	<i>-1.34e<sup>-8</sup></i>	<i>0.0405</i>
	<b>180</b>	<i>06:13:30</i>	<i>06:58:30</i>	<i>45.0</i>	<i>-2.24e<sup>-8</sup></i>	<i>0.0605</i>
	<b>270</b>	-	-	-	-	<i>0</i>
	<b>345</b>	-	-	-	-	<i>0</i>
<b>Garni</b>	<b>20</b>	<i>07:57:54</i>	<i>09:03:36</i>	<i>65.7</i>	<i>-1.37e<sup>-8</sup></i>	<i>0.0539</i>
	<b>140</b>	<i>07:44:20</i>	<i>09:02:42</i>	<i>78.4</i>	<i>-2.81e<sup>-8</sup></i>	<i>0.0390</i>
	<b>180</b>	-	-	-	-	<i>0</i>
	<b>270</b>	-	-	-	-	<i>0</i>
	<b>345</b>	-	-	-	-	<i>0</i>
<b>Hale</b>	<b>20</b>	<i>09:04:30</i>	<i>10:14:42</i>	<i>70.2</i>	<i>-8.71e<sup>-9</sup></i>	<i>0.0367</i>
	<b>140</b>	<i>09:56:42</i>	<i>11:13:12</i>	<i>76.5</i>	<i>-6.32e<sup>-9</sup></i>	<i>0.0297</i>
	<b>180</b>	-	-	-	-	<i>0</i>
	<b>270</b>	-	-	-	-	<i>0</i>
	<b>345</b>	-	-	-	-	<i>0</i>

Table 4.2 Baseline volumes of water vapor deliquesced at the 4 RSL study sites during each of the 5 seasons investigated.

## **4.4 Discussion**

This discussion covers a comparison between the quantity of water that might be extracted from the atmosphere with observed RSL seasonality, the effects of dust on deliquescence, the kinematics of deliquescence, and concludes with a discussion of any correlations between proposed RSL formation mechanism and the potential of atmospheric water vapor being the source of volatiles for RSL activity.

### **4.4.1 Comparison of Expected Deliquescence with Observed RSL Activity**

HiRISE observations have monitored all four study sites since Mars Year 31, accumulating over four Mars years of orbital observations. A summary of observed RSL seasonality is compared with the likelihood of deliquescence modeled by MRAMS (Figure 4.14). Periods of RSL lengthening, inactivity, termination, and fading are plotted over an annual cycle. Simulated likelihood of deliquescence is shown for the five seasons, where solid black circles indicate that deliquescence is possible under modeled baseline conditions, open circles correspond to modeled cases where no deliquescence is expected, and half-filled circles suggest that while conditions for deliquescence is not indicated for baseline conditions, it may be possible for upper limits in the sensitivity analysis. Circle sizes are scaled in proportion to the maximum amount of deliquescence at each specific site.



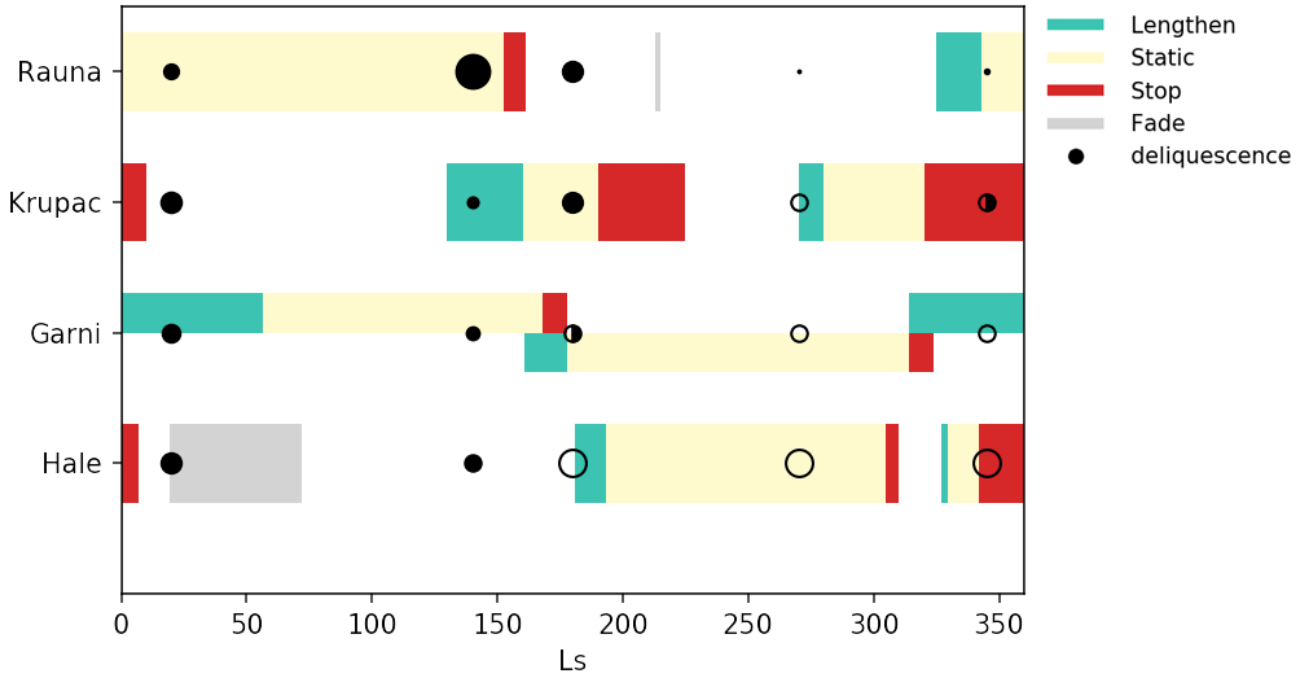


Figure 4.14 Likelihood of deliquescence vs observed RSL seasonality  
 For each site, the initiation of RSL lengthening is in green, followed by period of inactivity shown in yellow, and red indicating seasons when RSL stop lengthening. Additionally, for Rauna and Hale Craters, grey indicate when RSL fade. Observed seasonality at Garni Crater is split into generally north-facing (top) vs. south-facing (bottom) RSL. Black circles represent the model results at the five simulated seasons. Solid black circles indicate deliquescence is possible under modeled baseline conditions, open circles correspond to modeled cases where no deliquescence is expected. Half-filled circles mean that while conditions for deliquescence is not indicated for the baseline conditions, it may be possible for upper limits in the sensitivity analysis. Circle sizes are scaled in proportion to the maximum amount of deliquescence at that specific site.

RSL at the northern mid-latitude Rauna Crater site are observed to begin appearing between  $L_s = 325.1^\circ$  and  $343.2^\circ$ . They stop lengthening between  $L_s = 152.7^\circ$  and  $161.4^\circ$ , and completely fade by  $L_s = 215^\circ$ . The MRAMS model results show conditions favorable for deliquescence year-round, though the highest amount of water extracted from the

atmosphere occurs during the  $L_s=140^\circ$  and  $L_s=180^\circ$  simulations, compared to peak RSL activity in the late northern winter during  $L_s=330-350^\circ$ .

Observed seasonality for RSL at Krupac Crater shows that peak activity occurs near  $L_s=200^\circ$  and  $10^\circ$ , stop lengthening and appear to be less active at aphelion when it is coldest, and fade near perihelion around  $L_s\sim 232^\circ$  to  $264^\circ$  (McEwen, 2018). From the model, favorable conditions for deliquescence were found for  $L_s = 140^\circ$  and  $180^\circ$ , consistent with when RSL are active. But it also predicts deliquescence during  $L_s=20^\circ$  when no widespread activity is observed. HiRISE observations show a second pulse of activity that initiates shortly after the southern summer solstice ( $L_s = 270^\circ$ ) and stops in late southern summer between  $L_s = 320^\circ$  and  $L_s = 10^\circ$ . Modelled results do not predict that deliquescence is possible during  $L_s = 270^\circ$ , and only the most optimistic scenario allows for deliquescence during  $L_s = 345^\circ$ .

Observations of RSL activity at Garni Crater are separated into north-facing slopes and south-facing slopes. North-facing RSL activity begins between  $L_s = 314.1^\circ$  and  $56.5^\circ$ , and stop between  $L_s = 168^\circ$  and  $177.7^\circ$ . South-facing RSL start between  $L_s = 160.7^\circ$  and  $177.7^\circ$ , and stop between  $L_s = 314.1^\circ$  and  $323.7^\circ$ , although interannual variability in RSL start times have been observed. Modeled baseline conditions at Garni Crater allow for deliquescence during  $L_s = 20^\circ$  and  $140^\circ$ , which coincides with the seasons when north-facing RSL at Garni Crater begin.

The first pulse of RSL activity at Hale Crater starts lengthening between  $L_s = 180.7^\circ$  and  $193.5^\circ$ , and stops lengthening between  $L_s = 304.7^\circ$  and  $309.8^\circ$ . A resurgence of RSL activity appears later in the year when a second pulse start lengthening at  $L_s = 326.9^\circ$  to

329.7° until lengthening stops between  $L_s = 341.9^\circ$  to  $L_s = 7^\circ$ , and finally completely fade between  $L_s = 19.2^\circ$  and  $72.2^\circ$  (Stillman & Grimm, 2018). In comparison, deliquescence in the model only occurs at  $L_s = 20^\circ$  and  $L_s = 140^\circ$ , when the temperature and water vapor mixing ratios are low in the southern mid-latitude. These seasons when deliquescence is expected occurs nearly opposite to when RSL are actually observed with HiRISE.

Overall, a comparison between modelling results and HiRISE observations does not reveal a clear correlation between seasons when surface conditions are conducive to deliquescence and seasons when RSL activity are observed. The comparison at Garni Crater suggests that periods when deliquescence is expected does coincide with seasons when RSL are most active whereas the trend at Hale Crater appears to be anti-correlated. Other locations such as Krupac Crater and Rauna Crater appears to be less conclusive, as periods when water extraction rates are the highest does not necessary correlate to times when RSL are the most active. There are also instances where RSL appear in HiRISE observations even though no deliquescence is expected at all in the model.

#### **4.4.2 Effects of Dust**

Significant increases in observed RSL activity have been associated with periods following dust events. Garni Crater in particular is located along a prominent dust corridor. Regional dust storms travelling along the Acidalia storm track from the northern hemisphere to the south can extend longitudinally into eastern Valles Marineris and Coprates Chasma where Garni Crater is located (Cantor et al., 2001; Wang & Richardson, 2015). The relative dust opacities during these local storms can range from 0.54 for diffuse haze to 2.13 in

concentrated regions (Cantor et al., 2001). RSL at Garni Crater following regional dust events in MY31 showed significantly higher density compared to years without substantial dust activity (Stillman et al., 2017). RSL activity are also observed to be enhanced planet-wide following the MY 28 and MY 34 global dust storms. During major dust events, RSL are active for longer periods, lengthen much farther downhill, and many more RSL are observed to emanate from bedrock with some even originating from regolith (McEwen et al., 2014; Ojha et al., 2014; Stillman et al., 2014).

Regional and planet-encircling dust storms have the effects of modifying the appearance of the surface, the local temperature structure, as well as the vertical distribution of water vapor. RSL typically occur on low-albedo and dust-poor slopes. As such, the brightening of the surface following dust deposition increases their contrast which aids in RSL detection by making RSL more visible (McEwen, 2018; Stillman, 2017). Periods of enhanced atmospheric dust have the overall effect of cooling daytime temperatures and raising nighttime temperatures in the near-surface. Dust lofted into the atmosphere reduces the solar insolation at the surface, lowering the daytime surface temperature (Smith et al., 2002; Smith, 2004). During the MY 34 global dust storm, Curiosity's meteorological sensors recorded a warming in overnight low temperatures due to increased downwelling infrared radiation (Martínez et al., 2017). The resultant nighttime minimum air temperature occurring near 05:00 local true solar time increased by  $\sim 10\text{K}$  while the ground temperatures increased by  $\sim 20\text{K}$  warmer compared to pre-storm values (Guzewich et al., 2019). The typical diurnal amplitude in maximum-minimum ground temperature declined from a pre-storm value of  $\sim 90\text{K}$  to  $\sim 35\text{K}$  during the storm (Prats et al., 2018, Guzewich et al., 2019),

which is consistent with observations by the Submillimeter Wave Astronomy Satellite (SWAS) which found that the diurnal variation in surface temperature was reduced by a factor of two during the peak of the 2011 dust storm (Gurwell et al., 2005). In addition to the changes in temperature distribution during periods of high dust loading, the changes in solar insolation due to high dust opacity also significantly alter the vertical distribution of water vapor in the lower atmosphere. The atmospheric vapor content and profile is largely controlled by the atmospheric temperature. Orbital observations of previous global storms have hinted that the atmosphere exhibits a lower water content during and after global dust storms as atmospheric temperatures warm (Fedorova et al., 2018; Smith et al., 2002, 2018). The Rover Environmental Monitoring Station (REMS) onboard Curiosity provided the first in situ measurement of relative humidity performed during a global dust storm, showed that daily maximum relative humidity dropped from seasonally typical values of ~10% to ~5% as the storm encompassed Gale Crater, largely due to warmer overnight minimum temperatures (Guzewich et al., 2019). The significant modifications in surface temperature and relative humidity as a result of high atmospheric dust opacity have a direct effect on the vapor diffusion rate between the surface and the atmosphere. While the decrease in relative humidity during global dust storms may contribute to less optimal conditions for deliquescence, it is significantly offset by the increase in near surface temperatures especially during the evening which serves to provide a more favorable environment for water vapor adsorption and deliquescence at the surface.

### 4.4.3 Kinetics of Deliquescence

Our model simulations along with other theoretical studies have shown that conditions suitable for deliquescence on Mars are short-lived, lasting only a few hours per sol primarily in the morning and occasionally in the evening. Our calculations assume that deliquescence occur immediately upon reaching the appropriate temperature and relative humidity conditions for the aqueous state in the calcium perchlorate phase diagram, and terminate immediately after the necessary environmental conditions are no longer met. However, a lag may exist from the time when deliquescence begins to the time when darkening on the surface is observed. The water vapor fluxes used in our modeling assume a zero percent relative humidity right on the surface layer, which would not be the case as soon as deliquescence begins. A number of laboratory studies have revealed the thermodynamic conditions under which deliquescence may occur, but the kinetics of deliquescence and efflorescence is less well understood. Experiments by Gough et al. (2019) investigated the behavior of water uptake by calcium perchlorate salts over two Martian diurnal cycles to closely simulate the temperature and relative humidity at Valles Marineris during  $L_s = 120^\circ$ . Calcium perchlorate particles were visually observed to grow and darken as relative humidity increased, whereas particle sizes decreased as relative humidity was reduced as the salts undergo cycles of deliquescence and efflorescence (Gough et al., 2019). However, the timing of the observed size transformations and surface darkening with respect to the timing of when temperature and relative humidity enters and exits the aqueous phase space for  $\text{Ca}(\text{ClO}_4)_2$  have not yet been reported, nor has the estimated diurnal

volumes of water vapor uptake and release by the calcium perchlorate salts. If a hysteresis effect enables calcium perchlorate grains to remain darkened beyond when the environmental conditions remains in the aqueous phase space, it may allow for surface changes to be detected by orbital observation beyond the short window of when deliquescence may be actively taking place.

#### **4.4.4 Implications for RSL Formation Mechanisms**

Based on our results of the quantity of water vapor that can be extracted from the atmosphere through deliquescence, we consider the implications of an atmospheric source of volatile for several proposed RSL formation mechanisms. Atmospheric water vapor is an appealing candidate for the source of the volatile in the wet-dominated and wet-triggered RSL formation mechanisms since it is ubiquitously available regardless of latitudinal or elevation constraints. However, our results showed that water volumes on the order of only a few hundredths to a few tenths of  $\mu\text{m}$  is available through deliquescence. Given that the proposed water budgets of  $7 \text{ mls}^{-1}$  is required for wet-dominated RSL formation mechanisms as previously discussed by Raack et al. (2017), it is extremely unlikely for atmospheric vapor to be the primary source of volatile for wet-dominated RSL formation mechanisms. The quantity required for wet-dominated flow is orders of magnitude greater than the amount of water that was found even at the highest water yielding site surveyed in this study (Rauna Crater at  $L_s = 140^\circ$ ). For a wet-triggered mechanism of RSL formation, an instantaneous catchment area of at least  $100 \text{ km}^2$  would be required to supply the 70 grams of water necessary to initiate dry-debris mass wasting as in the case for Massé et al. (2016)'s

experiments. However, even if RSL are formed by completely dry granular flows, deliquescence may still play an important role. The volumetric changes in perchlorate salts as individual particles undergo phase transitions may impact the stability of grain cohesion and contribute to dry mass wasting as suggested by Dundas et al. (2017).

#### **4.5 Conclusions**

Using mesoscale simulations, we determined that the quantity of water vapor that can be extracted from the atmosphere through the deliquescence of calcium perchlorate yields an upper limit on the order of 1  $\mu\text{m}$  per sol. This quantity is found assuming the greatest range of favorable conditions when deliquescence may be possible given the range of environmental conditions found on present-day Mars. Experiments simulating the surface temperature and relative humidity at Rauna, Krupac, Garni, and Hale Crater at  $L_s = 20^\circ, 140^\circ, 180^\circ, 270^\circ, 345^\circ$  found that the times of year most conducive to deliquescence lacked a clear correlation to observed seasons when RSL are most active. We conclude that the quantities of water supplied by atmospheric origin are too low to be a viable source of volatile for any of the wet-dominated mechanisms of RSL formation. This quantity of water is still likely to be too low to induce wet-triggered mechanisms at the surface. However, deliquescence of calcium perchlorate could still play a significant role for dry granular flow models of RSL formation through the volumetric changes of the salts during diurnal cycles of hydration and dehydration.



## **CHAPTER 5**

### **CONCLUSIONS**

#### **5.1 Conclusions**

Water on Mars continues to be a quintessential target in planetary exploration as it has been emphasized as the critical link for understanding Mars' past and present climate, geology, its potential for habitability, and for assessing in situ resources for future human exploration. Regional atmospheric circulation, in particular, facilitate the transport of water across the planet as well as exchange processes in the planetary boundary layer.

Our investigation of the behavior of water on regional scales began with an understanding of the distribution of water in the Tharsis-Valles Marineris system within the context of the global circulation. The global water cycle simulated with the NASA Ames Mars General Circulation Model reproduces large-scale features such as the cross equatorial overturning circulation, the seasonal variations in column vapor abundances, and the aphelion cloud belt in good agreement with orbital observations. The output from this global scale simulation is then used to provide boundary conditions for mesoscale model simulations to specifically resolve the local scale circulation and atmospheric phenomenon that are of particular interest to our research objectives. Superimposed on the global circulation, the regional scale water cycle is highly influenced by the thermal and dynamical forcing of local topographic gradients as well as the underlying surface properties such as thermal inertia and albedo. Terrain-following air parcels forced along the slopes of the

Tharsis volcanoes and the steep canyon walls of neighboring Valles Marineris significantly impact the local water vapor concentration and the associated conditions for cloud formation in these regions. Over the Tharsis Plateau, water vapor forced up the flanks of the major volcanoes form asymmetrically water ice clouds on their leeward side and governs the structure of the aphelion cloud belt. Water ice clouds are important contributors to the climatic forcing on Mars, and their radiative feedbacks on the mesoscale circulations in the Tharsis and Valles Marineris regions significantly contribute to the regional perturbations to the large-scale global atmospheric circulation.

One of the major findings in this dissertation is the non-homogeneous regional distribution of water in the planetary boundary layer. Mesoscale simulations reveal distinct phase differences in the diurnal cycle of water vapor and water ice inside Valles Marineris compared to the adjacent plateau. During the day, moist air converges into the Valles Marineris region via easterly flows, while a dry air mass in the late morning sweeps northwards passing over the rims of the canyon by low-level winds at the plateau level. As such, the diurnal amplitude in total water on the plateau is much greater than the diurnal variability of water inside the canyon. Vertical transport of water along the canyon walls further contribute to the substantial asymmetry in the day-night concentrations of water vapor inside versus outside the canyon. While daytime upslope winds mechanically force the evacuation of water along the slopes of the canyon walls, subsidence motion induced in accordance with mass continuity drives water vapor back into the canyon. As a result, this regional vapor transport regime strongly modulates the concentration of water available for water ice cloud formation in Valles Marineris.

Analysis of water ice fogs inside the Valles Marineris canyon system revealed that it is possible to form thin layers of water ice clouds in Valles Marineris that are confined entirely within the lower reaches of the canyon in the early morning when the atmosphere inside the canyon becomes saturated. However, the nature of the low-lying clouds inside Valles Marineris is completely unlike fogs observed in terrestrial canyons such as those in the Grand Canyon on Earth. Fogs in Valles Marineris typically form in conjunction with much higher opacity dust layers, as well as wide-spread water ice cloud formation over the plateaus adjacent to the canyon. Overall, the formation of water ice clouds in Valles Marineris is highly influenced by radiative feedbacks forced by the thermal properties of the underlying surface.

The investigation of the influences of atmosphere water on the activity of recurring slope lineae (RSL) showed that the maximum quantity of water the atmosphere can supply via deliquescence onto calcium perchlorate salts under the most optimal conditions is on the order of one precipitable micron per sol. This water budget estimate is based on modeled surface and near-surface conditions at four key RSL sites during five different seasons. Conditions conducive to deliquescence are extremely sensitive to surface temperatures and relative humidity, and the seasonally varying atmospheric state at each location can significantly affect the timing for formation of RSL. Our results show that under the most favorable conditions, deliquesce maybe possible in the early morning, and again briefly in the evening at certain sites. No clear correlation was found between times of year when conditions are most favorable for deliquescence and observed seasons when RSL are most active. We conclude that while one micron per sol of water could potentially support a

formation scenario where small amounts of water disrupt the cohesion of regolith triggering dry flow, but an atmospheric source of water is unlikely to be the source of volatile for wet-dominated mechanisms of RSL formation.

## **5.2 Future Investigations**

A number of key science questions regarding the regional water cycle beyond the scope of this dissertation are still outstanding and must be answered in order to further improve our understanding of the Martian atmosphere. These include: (1) To what extent does subsurface-atmospheric exchange modify the water budget in the planetary boundary layer? (2) How does the coupling of water and dust modify the vertical distribution of water in the Martian atmosphere? (3) And how do the effects of the regional water cycle affect the overall global climate?

Future investigations targeting these outstanding questions can be made using existing data, as well as observations from instruments on several upcoming missions. One highly beneficial future study is the retrieval of water vapor using TES observations to generate a multi-annual climatology of the water vapor column abundances in the Martian atmosphere, a global multi-annual climatology of the vertical distribution of water vapor abundances on Mars. The spatial and temporal evolution of water in the Martian atmosphere remains an open question, and the vertical distribution of water vapor is an important diagnostic for determining the physical processes that drive the Martian water cycle. TES is uniquely suitable for building a multi-annual climatology of water vapor because of Mars

Global Surveyor's sun-synchronous, near-circular mapping orbit which provided nearly continuous observations of the Martian atmosphere over three consecutive Mars years. These long-term global observations of the Martian water vapor are widely applicable to a number of investigations including opportunities to further investigate and constrain processes such as atmospheric dynamics, cloud radiative feedbacks, chemistry, escape processes, as well as surface-atmospheric interactions. These observations will also be useful for validating existing climate models. The TES vertical water vapor profiles are expected to extend up to 40km in altitude, and will complement The Mars Express SPICAM spectrometers' vertical measurements of water vapor which were obtained at higher altitudes (Maltagliati et al., 2013). TES climatology will also be invaluable for establishing a baseline for comparisons with upcoming water vapor observations from the Trace Gas Orbiter (TGO).

The quality of TES spectra can be improved by spatial and temporal averaging. We will bin the entire set of TES limb scanning observations into  $10^\circ$  Ls x  $30^\circ$  longitude x  $10^\circ$  latitude x 5km altitude grids, similar to the averaging done by Guzewich et al. (2013) for the retrieval of vertical dust profiles using TES limb scan observations. Atmospheric temperatures are retrieved at each model level following the method outlined in Smith et al. (2001). To retrieve water vapor abundances from TES observed radiances, we will probe the water vapor absorption bands in the spectral region between  $240\text{--}360\text{ cm}^{-1}$  ( $28\text{--}42\text{ }\mu\text{m}$ ), where five prominent water vapor bands can be identified (Smith, 2002). This spectral window is favorable for performing retrievals because of the high signal-to-noise ratio ( $\sim 500$ ) at these wavelengths, and relatively low opacity from dust and water-ice aerosols

(Smith et al., 2000). We will derive a water vapor retrieval algorithm using a discrete ordinates radiative transfer model with a correlated-k approximation to compute water vapor absorption. Correlated-k coefficients can be obtained from the GEISA database (Jacquinet-Husson et al., 2011) and corrected for CO<sub>2</sub> broadening in the Martian atmosphere. Our radiative transfer model will account for surface emissivity, dust aerosol, water ice extinction, multiple scattering, as well as gaseous absorption. TES nadir observations are matched to modeled radiances computed using a plane-parallel atmosphere, while limb-scanning radiances are integrated along the curved path traced by the TES pointing vectors in the plane-parallel coordinate system to account for the inherently spherical geometry of the limb observations. For the limb-scanning observations, we expect to retrieve 4 distinct measurements with a vertical resolution of ~10 km extending up to 40 km altitude. The Levenberg-Marquardt optimization method can be used to minimize chi-squared residuals, and the retrieval is iterated until the algorithm converges on a self-consistent solution. An example of a retrieved spectrum of the water vapor absorption bands from TES nadir observations (Smith, 2002) is shown in Figure 5.1b. Water vapor gas absorption can be retrieved from the limb-scanning observations as well as nadir observations. We will run the retrieval algorithm over the entire TES dataset. The retrievals will generate three-dimensional (latitude-longitude-height) water vapor mixing ratios cubes that evolve with time over 3 Martian years. They will represent the first global climatological record of the vertical distribution of water vapor on Mars.

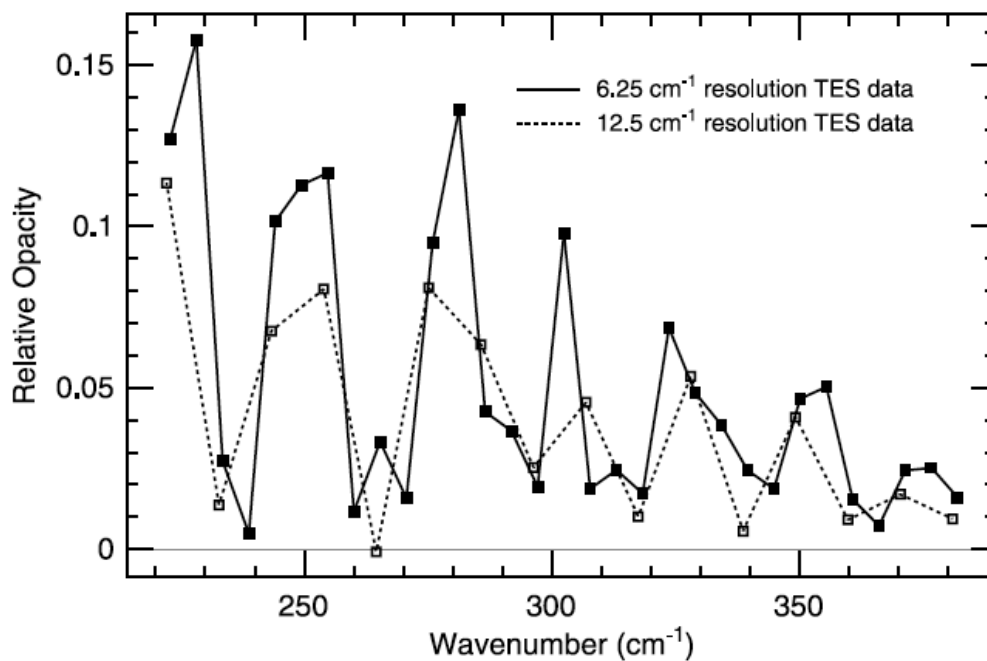
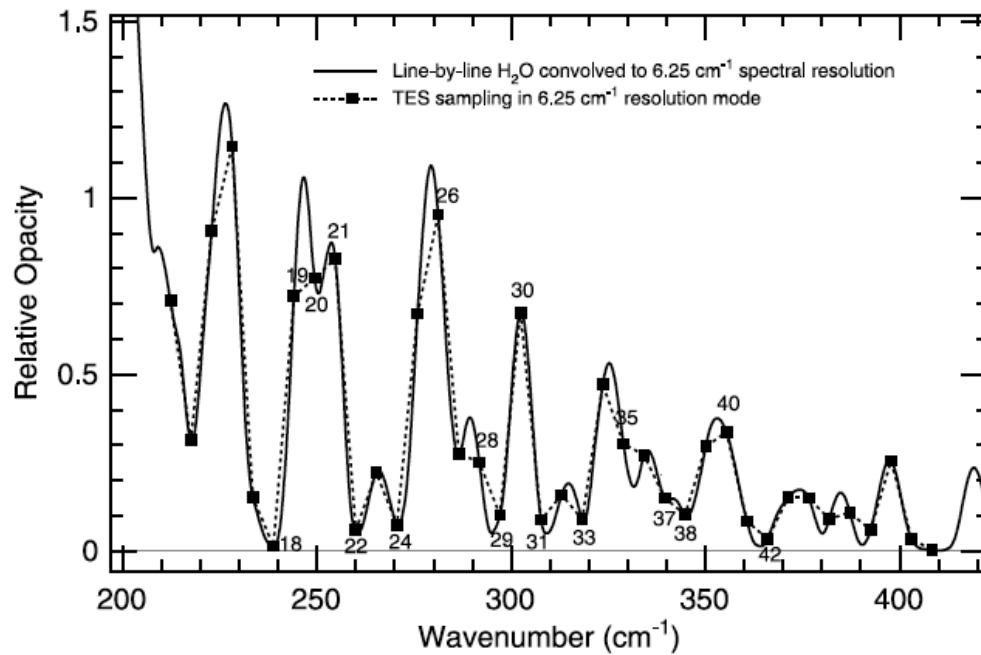


Figure 5.1 Fit between an observed TES spectrum versus the best-fit synthetic spectrum for one modeled bin. A column abundance of 25 pr- $\mu\text{m}$  is indicated. (M. D. Smith, 2002)

By modifying the retrieval algorithm used by Smith (2004) for the retrieval of column water vapor with TES nadir observations, as well as the algorithm used by Guzewich et al. (2013) for the retrieve of vertical dust profiles with TES limb observations, new algorithms can be generated for the retrieval of vertical water vapor profiles using the combined TES nadir and limb-scanning datasets. The new retrievals can solve for water vapor mixing ratios up to 40 km above the areoid. A preliminary demonstration of this retrieval shows significant improvement in the resolution at the bottom most scale height of the atmosphere when TES limb-scanning spectra are fitted simultaneously with the average of overlapping nadir-pointed spectra. This boundary layer is especially important for examining any observable signatures of water vapor fluxes resulting from surface-atmospheric exchanges.

To reduce the number of free parameters in our retrieval algorithm, TES-retrieved dust and water ice aerosol profiles determined by Guzewich et al. (2013) can be used as weighting functions for initial input into the new water vapor retrievals (Fig. 5.2). A sample result of a modeled vertical water vapor profile from a pilot study is shown in Figure 5.3. The performance of this preliminary method appears promising, but many details remain to be worked out. Enhancements planned for this proposed research include modifying the underlying radiative transfer code to improve aerosol size and shape parameterizations, incorporating the delta approximation (Goody & Yung, 1989) to allow for more efficient modeling of highly-forward scattering particle phase functions, as well as removing a continuum opacity from the water vapor absorption bands to reduce the propagation of aerosol uncertainties. Reconstructing the 3-dimensional variability of water for the first time



will directly address a fundamental knowledge gap in our understanding of the Martian water cycle.

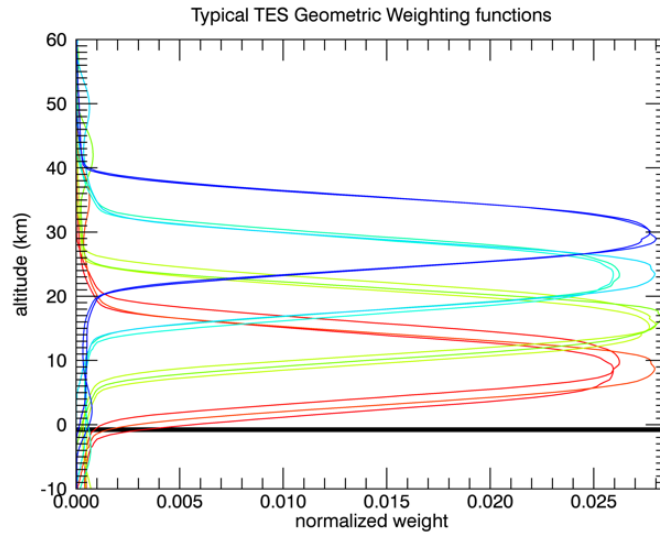


Figure 5.2 TES Geometric Weighting functions for the radiative transfer code (McConnochie et al., 2018)

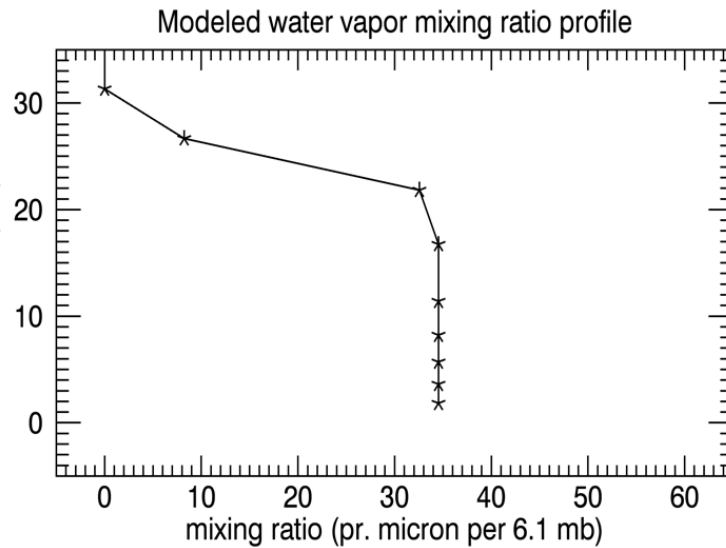


Figure 5.3 Sample modeled water vapor vertical profile from the pilot study (McConnochie et al., 2018)

Coordinated observations from orbiter spacecraft paired with surface measurements from landed instruments provide another opportunity to study the regional water cycle on Mars and answer key knowledge gaps about the Martian planetary boundary layer. The vertical distribution of water abundances from the surface up to 80 km connect processes occurring in the boundary layer to those active aloft. Coordinated observations presents a unique opportunity to study the full vertical atmospheric column at the same time, allowing measurements to be cross-calibrated between instruments. Using simultaneous atmospheric observations from the Mars Reconnaissance Orbiter (MRO) and the Phoenix Mars Lander (PHX), as well as ongoing commensurate measurements from MRO and the Mars Science Laboratory (MSL), the regional water cycle can be investigated from the surface up to the middle stratosphere over the Phoenix landing site and Gale Crater in the context of the local surface and atmospheric environment.

Furthermore, coordinate measurements help to better understand the coupling between the dust & water cycles by determining the extent to which the regional distribution of water is modified by the presence of detached dust layers, as well as during global and regional dust events. Several prominent dust features were present during the 3 years of TES mapping: the persistent but seasonally dependent detached dust layers centered ~20-30 km, several large regional flushing dust storms during MY26, and most notably the 2001 (MY25) global encircling dust storm. A comprehensive database of Mars daily global maps (MDGMs) produced from MOC images (Wang & Ingersoll, 2002) is contemporaneous with nearly the entire TES limb data set and is useful for comparison with retrieved water vapor profiles to determine any correlations between the dust and water vapor distributions. For example,

the 2001 global dust storm observed by TES in limb-scanning mode lofted dust to heights above 60 km (Clancy et al., 2010), and a natural place to start is to examine the behavior of the water vapor distribution during that time period. Heavens et al. (2018) suggest that dust storms, such as the one currently brewing on Mars, can transport water vapor to the middle atmosphere by deep convection. If this testable hypothesis is true, TES retrievals should see signs of water vapor increase in the 30-40 km altitude region where water vapor typically drops off.

Within the numerical atmospheric models, the feedbacks on water vapor must be consistent with the behavior of modeled dust and water ice. Cloud formation is thought to be a key process coupling the dust and water cycles. GCM and regional scale simulations can inform TES retrieved water vapor profiles regarding the altitudes where detached dust layers occur, how they might relate to water ice clouds formation, as well as where the bulk of water vapor transport occurs. Major discrepancies between GCM with TES vertical structure for a similar dust scenario could inform us about missing physical processes that the climate models are unable to capture. This type of study would examine how dust couple with the water cycle to modify the vertical distribution of water in the Martian atmosphere.

Ultimately, understanding the characteristics of the water cycle is key to our investigation of the geologic history, past and present climate, and the potential for habitability, as well as in preparation for future robotic and human exploration of Mars. The results from this dissertation as well as future investigations of the regional atmospheric dynamics of water on Mars will improve our understanding of the Martian meteorological

system, feedbacks on the coupling of the dust and water cycles, and the relative significance of various local H<sub>2</sub>O reservoirs to the overall long-term Martian water budget.

## REFERENCES

- Atwood-Stone, C., & McEwen, A. S. (2013). Avalanche slope angles in low-gravity environments from active Martian sand dunes. *Geophysical Research Letters*, *40*(12), 2929–2934. <https://doi.org/10.1002/grl.50586>
- Barnes, J. R. (1981). Midlatitude Disturbances in the Martian Atmosphere: A Second Mars Year. *Journal of the Atmospheric Sciences*, *38*(2).
- Bass, D. S., Herkenhoff, K. E., & Paige, D. A. (2000). Variability of Mars' North Polar Water Ice Cap: I. Analysis of Mariner 9 and Viking Orbiter Imaging Data. *Icarus*, *144*(2), 382–396. <https://doi.org/10.1006/icar.1999.6300>
- Bass, D. S., & Paige, D. A. (2000). Variability of Mars' North Polar Water Ice Cap: II. Analysis of Viking IRTM and MAWD Data. *Icarus*, *144*(2), 397–409. <https://doi.org/10.1006/icar.1999.6301>
- Benson, J. L., Kass, D. M., & Kleinböhl, A. (2011). Mars' north polar hood as observed by the Mars Climate Sounder. *Journal of Geophysical Research E: Planets*, *116*(3), 1–13. <https://doi.org/10.1029/2010JE003693>
- Bibring, J. P., Langevin, Y., Gendrin, A., Gondet, B., Poulet, F., Berthé, M., ... Forget, F. (2005). Mars surface diversity as revealed by the OMEGA/Mars express observations. *Science*, *307*(5715), 1576–1581. <https://doi.org/10.1126/science.1108806>
- Brass, G. W. (1980). Stability of brines on Mars. *Icarus*, *42*(1), 20–28. [https://doi.org/10.1016/0019-1035\(80\)90237-7](https://doi.org/10.1016/0019-1035(80)90237-7)
- Cantor, B. A., James, P. B., Caplinger, M., & Wolff, M. J. (2001). Martian dust storms: 1999 Mars Orbiter Camera observations. *Journal of Geophysical Research E: Planets*, *106*(E10), 23653–23687. <https://doi.org/10.1029/2000JE001310>
- Chevrier, V. F., & Rivera-Valentin, E. G. (2012). Formation of recurring slope lineae by liquid brines on present-day Mars. *Geophysical Research Letters*, *39*(21), 1–6. <https://doi.org/10.1029/2012GL054119>
- Chojnacki, M., McEwen, A., Dundas, C., Ojha, L., Urso, A., & Sutton, S. (2016). *Journal of Geophysical Research : Planets Geologic context of recurring slope lineae in Melas*. (May), 1204–1231. <https://doi.org/10.1002/2015JE004991>. Received
- Clancy, R. T., Grossman, A. W., Wolff, M. J., James, P. B., Rudy, D. J., Billawala, Y. N., ... Muhleman, D. O. (1996). Water vapor saturation at low altitudes around Mars aphelion: A key to Mars climate? *Icarus*, *122*(1), 36–62. <https://doi.org/10.1006/icar.1996.0108>
- Clancy, R. Todd, Wolff, M. J., Whitney, B. A., Cantor, B. A., Smith, M. D., & McConnochie, T. H. (2010). Extension of atmospheric dust loading to high altitudes during the 2001 Mars dust storm: MGS TES limb observations. *Icarus*, *207*(1), 98–109. <https://doi.org/10.1016/j.icarus.2009.10.011>
- Clark, B. C. (1978). Implications of abundant hygroscopic minerals in the Martian regolith. *Icarus*, *34*(3), 645–665. [https://doi.org/10.1016/0019-1035\(78\)90052-0](https://doi.org/10.1016/0019-1035(78)90052-0)
- Colaprete, A., & Toon, O. B. (1999). Cloud Formation Under Mars Pathfinder Conditions. *Journal of Geophysical Research*, *104*(E4), 9043–9053.
- Davies, D. W. (1979). The vertical distribution of water vapor. *Journal of Geophysical*

- Research*, 84(B6), 2875–2879.
- Deardorff, J. W. (1972). Numerical Investigation of Neutral and Unstable Planetary Boundary Layers. *Journal of the Atmospheric Sciences*, Vol. 29, pp. 91–115. [https://doi.org/10.1175/1520-0469\(1972\)029<0091:nionau>2.0.co;2](https://doi.org/10.1175/1520-0469(1972)029<0091:nionau>2.0.co;2)
- Dickson, J. L., Head, J. W., Levy, J. S., & Marchant, D. R. (2013). Don Juan Pond, Antarctica: Near-surface CaCl<sub>2</sub>-brine feeding Earth's most saline lake and implications for Mars. *Scientific Reports*, 3(4), 1–8. <https://doi.org/10.1038/srep01166>
- Dundas, C. M., McEwen, A. S., Chojnacki, M., Milazzo, M. P., Byrne, S., McElwaine, J. N., & Urso, A. (2017). Granular flows at recurring slope lineae on Mars indicate a limited role for liquid water. *Nature Geoscience*, 10(12), 903–907. <https://doi.org/10.1038/s41561-017-0012-5>
- Farmer, C. B., Davies, D. W., Holland, A. L., Laporte, D. D., & Doms, P. E. (1977). Mars: Water vapor observations from the Viking orbiters. *Journal of Geophysical Research*, 82(28), 4225–4248. <https://doi.org/10.1029/js082i028p04225>
- Farmer, Crofton B. (1976). Liquid Water on Mars. *Icarus*, 9, 279–289.
- Fedorova, A. A., Korablev, O. I., Bertaux, J. L., Rodin, A. V., Montmessin, F., Belyaev, D. A., & Reberac, A. (2009). Solar infrared occultation observations by SPICAM experiment on Mars-Express: Simultaneous measurements of the vertical distributions of H<sub>2</sub>O, CO<sub>2</sub> and aerosol. *Icarus*, 200(1), 96–117. <https://doi.org/10.1016/j.icarus.2008.11.006>
- Fischer, E., Martínez, G. M., & Renn, N. O. (2016). Formation and persistence of brine on mars: Experimental simulations throughout the diurnal cycle at the phoenix landing site. *Astrobiology*, 16(12), 937–948. <https://doi.org/10.1089/ast.2016.1525>
- Forget, F., Hourdin, F., Fournier, R., Hourdin, C., Talagrand, O., Collins, M., ... Huot, J. P. (1999). Improved general circulation models of the Martian atmosphere from the surface to above 80 km. *Journal of Geophysical Research E: Planets*, 104(E10), 24155–24175. <https://doi.org/10.1029/1999JE001025>
- French, R. G., Gierasch, P. J., Popp, B. D., & Yerdon, R. J. (1981). Global patterns in cloud forms on Mars. *Icarus*, 45(2), 468–493. [https://doi.org/10.1016/0019-1035\(81\)90047-6](https://doi.org/10.1016/0019-1035(81)90047-6)
- Goff, J. A., & Gratch S. (1946). Low-pressure properties of water from –160 to 212 F. *52nd Annual Meeting, Am. Soc. of Heating and Ventilating Eng.* New York.
- Gómez-Elvira, J., Armiens, C., Castañer, L., Domínguez, M., Genzer, M., Gómez, F., ... Martín-Torres, J. (2012). REMS: The environmental sensor suite for the Mars Science Laboratory rover. *Space Science Reviews*, 170(1–4), 583–640. <https://doi.org/10.1007/s11214-012-9921-1>
- Goody, R. M., & Yung, Y. L. (1989). *Atmospheric Radiation: Theoretical Basis*. New York: Oxford University Press.
- Gough, R. V., Chevrier, V. F., Baustian, K. J., Wise, M. E., & Tolbert, M. A. (2011). Laboratory studies of perchlorate phase transitions: Support for metastable aqueous perchlorate solutions on Mars. *Earth and Planetary Science Letters*, 312(3–4), 371–377. <https://doi.org/10.1016/j.epsl.2011.10.026>
- Gough, R. V., Chevrier, V. F., & Tolbert, M. A. (2014). Formation of aqueous solutions on Mars via deliquescence of chloride-perchlorate binary mixtures. *Earth and Planetary*

- Science Letters*, 393, 73–82. <https://doi.org/10.1016/j.epsl.2014.02.002>
- Gough, R. V., Chevrier, V. F., & Tolbert, M. A. (2016). Formation of liquid water at low temperatures via the deliquescence of calcium chloride: Implications for Antarctica and Mars. *Planetary and Space Science*, 131, 79–87. <https://doi.org/10.1016/j.pss.2016.07.006>
- Grimm, R. E., Harrison, K. P., & Stillman, D. E. (2014). Water budgets of martian recurring slope lineae. *Icarus*, 233, 316–327. <https://doi.org/10.1016/j.icarus.2013.11.013>
- Gurwell, M. A., Bergin, E. A., Melnick, G. J., & Tolls, V. (2005). Mars surface and atmospheric temperature during the 2001 global dust storm. *Icarus*, 175(1), 23–31. <https://doi.org/10.1016/j.icarus.2004.10.009>
- Guzewich, S. D., Lemmon, M., Smith, C. L., Martínez, G., de Vicente-Retortillo, Newman, C. E., ... Zorzano Mier, M. P. (2019). Mars Science Laboratory Observations of the 2018/Mars Year 34 Global Dust Storm. *Geophysical Research Letters*, 46(1), 71–79. <https://doi.org/10.1029/2018GL080839>
- Guzewich, S. D., Newman, C. E., Smith, M. D., Moores, J. E., Smith, C. L., Moore, C., ... Battalio, M. (2017). The Vertical Dust Profile Over Gale Crater, Mars. *Journal of Geophysical Research: Planets*, 122(12), 2779–2792. <https://doi.org/10.1002/2017JE005420>
- Guzewich, S. D., Toigo, A. D., Richardson, M. I., Newman, C. E., Talaat, E. R., Waugh, D. W., & McConnochie, T. H. (2013). The impact of a realistic vertical dust distribution on the simulation of the Martian General Circulation. *Journal of Geophysical Research E: Planets*, 118(5), 980–993. <https://doi.org/10.1002/jgre.20084>
- Haberle, R. M., Clancy, R. T., Forget, F., Smith, M. D., & Zurek, R. W. (2017). *The atmosphere and climate of Mars*. <https://doi.org/10.1017/9781139060172>
- Haberle, Robert M., & Jakosky, B. M. (1990). Sublimation and transport of water from the north residual polar cap on Mars. *Journal of Geophysical Research*, 95(B2), 1423. <https://doi.org/10.1029/jb095ib02p01423>
- Haberle, Robert M., Kahre, M. A., Hollingsworth, J. L., Montmessin, F., Wilson, R. J., Urata, R. A., ... Schaeffer, J. R. (2019). Documentation of the NASA/Ames Legacy Mars Global Climate Model: Simulations of the present seasonal water cycle. *Icarus*, 333(April), 130–164. <https://doi.org/10.1016/j.icarus.2019.03.026>
- Haberle, Robert M., Leovy, C. B., & Pollack, J. B. (1982). Some effects of global dust storms on the atmospheric circulation of Mars. *Icarus*, 50(2–3), 322–367. [https://doi.org/10.1016/0019-1035\(82\)90129-4](https://doi.org/10.1016/0019-1035(82)90129-4)
- Haberle, Robert M., Joshi, M. M., Murphy, J. R., Barnes, J. R., Schofield, J. T., Wilson, G., ... Schaeffer, J. (1999). *Pathfinder atmospheric structure investigation / meteorology data*. 104, 8957–8974.
- Haberle, Robert M., Pollack, J. B., Barnes, J. R., Zurek, R. W., Leovy, C. B., Murphy, J. R., ... Schaeffer, J. (1993). of Atmospheric Science , Oregon Observer , for example ) , but for now our knowledge is incomplete . we must 3Jet Propulsion California However , in doing so we must recognize that the models from Mars of Atmospheric Science , Palo Alto , general Californi. *Circulation*, 98, 3093–3123.
- Hanley, J., Chevrier, V. F., Barrows, R. S., Swaffler, C., & Altheide, T. S. (2015). *Journal of Geophysical Research : Planets oxychlorine salts with implications for Mars*. (May), 1–12.

- <https://doi.org/10.1002/2013JE004575>.Received
- Harri, a.-M., Genzer, M., Kemprien, O., Gomez-Elvira, J., Haberle, R. M., Polkko, J., & Al., E. (2014). Mars Science Laboratory relative humidity observations: Initial results. *Journal of Geophysical Research: Planets*, 2132–2147.  
<https://doi.org/10.1002/2013JE004514>.Received
- Heavens, N. G., Kleinböhl, A., Chaffin, M. S., Halekas, J. S., Kass, D. M., Hayne, P. O., ... Schofield, J. T. (2018). Hydrogen escape from Mars enhanced by deep convection in dust storms. *Nature Astronomy*, 2(2), 126–132. <https://doi.org/10.1038/s41550-017-0353-4>
- Hecht, M. H., Kounaves, S. P., Quinn, R. C., West, S. J., Young, S. M. M., Ming, D. W., ... Smith, P. H. (2009). Detection of perchlorate and the soluble chemistry of martian soil at the phoenix lander site. *Science*, 325(5936), 64–67.  
<https://doi.org/10.1126/science.1172466>
- Heinz, J., Schulze-Makuch, D., & Kounaves, S. P. (2016). Deliquescence-induced wetting and RSL-like darkening of a Mars analogue soil containing various perchlorate and chloride salts. *Geophysical Research Letters*, 43(10), 4880–4884.  
<https://doi.org/10.1002/2016GL068919>
- Hess, S. L., Henry, R. M., Leovy, C. B., Ryan, J. A., Tillman, J. E., Chamberlain, T. E., ... Mitchell, J. L. (1976). Preliminary meteorological results on Mars from the Viking 1 lander. *Science*, 193(4255), 788–791. <https://doi.org/10.1126/science.193.4255.788>
- Houben, H., Haberle, R. M., Young, R. E., & Zent, A. P. (1997). Modeling the Martian seasonal water cycle. *Journal of Geophysical Research E: Planets*, 102(E4), 9069–9083.  
<https://doi.org/10.1029/97JE00046>
- Inada, A., Garcia-Comas, M., Altieri, F., Gwinner, K., Poulet, F., Belluci, G., ... Bibring, J. P. (2008). Dust haze in Valles Marineris observed by HRSC and OMEGA on board Mars Express. *Journal of Geophysical Research E: Planets*, 113(2), 1–18.  
<https://doi.org/10.1029/2007JE002893>
- Ingersoll, A. P. (1970). Mars: occurrence of liquid water. *Science*, 168(3934), 972–973.  
<https://doi.org/10.4045/tidsskr.09.0631>
- Iraci, L. T., Phebus, B. D., Stone, B. M., & Colaprete, A. (2010). Water ice cloud formation on Mars is more difficult than presumed: Laboratory studies of ice nucleation on surrogate materials. *Icarus*, 210(2), 985–991.  
<https://doi.org/10.1016/j.icarus.2010.07.020>
- Jakosky, B. M. ., & Haberle, R. M. (1992). The seasonal behavior of water on Mars. In *Mars* (pp. 969–1016).
- Jakosky, B.M. (1985). The seasonal cycle of water on Mars. *Space Sci. Rev.*, 41 (June), 131–200.
- Jakosky, Bruce M. (1983a). The role of seasonal reservoirs in the Mars water cycle. I. Seasonal exchange of water with the regolith. *Icarus*, 55(1), 1–18.  
[https://doi.org/10.1016/0019-1035\(83\)90046-5](https://doi.org/10.1016/0019-1035(83)90046-5)
- Jakosky, Bruce M. (1983b). The role of seasonal reservoirs in the Mars water cycle. II. Coupled models of the regolith, the polar caps, and atmospheric transport. *Icarus*, 55(1), 19–39. [https://doi.org/10.1016/0019-1035\(83\)90047-7](https://doi.org/10.1016/0019-1035(83)90047-7)



- Jakosky, Bruce M., & Farmer, C. B. (1982). The seasonal and global behavior of water vapor in the Mars atmosphere: Complete global results of the Viking Atmospheric Water Detector Experiment. *Journal of Geophysical Research*, *87*(B4), 2999. <https://doi.org/10.1029/jb087ib04p02999>
- Kahn, R. (1984). Spatial and Seasonal Distribution of Martian Clouds and Some Meteorological Implications. *Journal of Geophysical Research*, *89*(A8), 6671–6688. <https://doi.org/10.1029/JA089iA08p06671>
- Kahre, M. A., Hollingsworth, J. L., Haberle, R. M., & Wilson, R. J. (2015). Coupling the Mars dust and water cycles: The importance of radiative-dynamic feedbacks during northern hemisphere summer. *Icarus*, *260*, 477–480. <https://doi.org/10.1016/j.icarus.2014.07.017>
- Kahre, Melinda A., Murphy, J. R., & Haberle, R. M. (2006). Modelling the Martian dust cycle and surface dust reservoirs with the NASA Ames general circulation model. *Journal of Geophysical Research E: Planets*, *111*(6), 1–25. <https://doi.org/10.1029/2005JE002588>
- Kass, D. M., Schofield, J. T., Michaels, T. I., Rafkin, S. C. R., Richardson, M. I., & Toigo, A. D. (2003). Analysis of atmospheric mesoscale models for entry, descent, and landing. *Journal of Geophysical Research E: Planets*, *108*(12), 1–12. <https://doi.org/10.1029/2003je002065>
- KIEFFER, H. H., CHASE, S. C., MARTIN, T. Z., MINER, E. D., & PALLUCONI, F. D. (1976). Martian North Pole Summer Temperatures: Dirty Water Ice. *Science*, *194*(4271), 1341–1344. <https://doi.org/10.1126/science.194.4271.1341>
- Kleinböhl, A., Schofield, J. T., Kass, D. M., Abdou, W. A., Backus, C. R., Sen, B., ... McCleese, D. J. (2009). Mars Climate Sounder limb profile retrieval of atmospheric temperature, pressure, and dust and water ice opacity. *Journal of Geophysical Research E: Planets*, *114*(10), 1–30. <https://doi.org/10.1029/2009JE003358>
- Leask, E. K., Ehlmann, B. L., Dundar, M. M., Murchie, S. L., & Seelos, F. P. (2018). Challenges in the Search for Perchlorate and Other Hydrated Minerals With 2.1- $\mu\text{m}$  Absorptions on Mars. *Geophysical Research Letters*, *45*(22), 12,180–12,189. <https://doi.org/10.1029/2018GL080077>
- Leshin, L. A., Mahaffy, P. R., Webster, C. R., Cabane, M., Coll, P., Conrad, P. G., ... Grotzinger, J. P. (2013). Volatile, isotope, and organic analysis of martian fines with the Mars curiosity rover. *Science*, *341*(6153), 1–10. <https://doi.org/10.1126/science.1238937>
- Levy, J. (2012). Hydrological characteristics of recurrent slope lineae on Mars: Evidence for liquid flow through regolith and comparisons with Antarctic terrestrial analogs. *Icarus*, *219*(1), 1–4. <https://doi.org/10.1016/j.icarus.2012.02.016>
- Levy, J. S., Fountain, A. G., Gooseff, M. N., Welch, K. A., & Lyons, W. B. (2011). Water tracks and permafrost in Taylor Valley, Antarctica: Extensive and shallow groundwater connectivity in a cold desert ecosystem. *Bulletin of the Geological Society of America*, *123*(11–12), 2295–2311. <https://doi.org/10.1130/B30436.1>
- Määttänen, A., Vehkamäki, H., Lauri, A., Merikallio, S., Kauhanen, J., Savijärvi, H., & Kulmala, M. (2005). Nucleation studies in the Martian atmosphere. *Journal of Geophysical Research E: Planets*, *110*(2), 1–12. <https://doi.org/10.1029/2004JE002308>

- Maltagliati, L., Montmessin, F., Fedorova, A., Korablev, O., Forget, F., & Bertaux, J. L. (2011). Evidence of water vapor in excess of saturation in the atmosphere of Mars. *Science*, 333(6051), 1868–1871. <https://doi.org/10.1126/science.1207957>
- Maltagliati, L., Montmessin, F., Korablev, O., Fedorova, A., Forget, F., Määttänen, A., ... Bertaux, J. L. (2013). Annual survey of water vapor vertical distribution and water–aerosol coupling in the martian atmosphere observed by SPICAM/MEx solar occultations. *Icarus*, 223(2), 942–962. <https://doi.org/10.1016/j.icarus.2012.12.012>
- Maltagliati, Luca, Titov, D. V., Encrenaz, T., Melchiorri, R., Forget, F., Keller, H. U., & Bibring, J. P. (2011). Annual survey of water vapor behavior from the OMEGA mapping spectrometer onboard Mars Express. *Icarus*, 213(2), 480–495. <https://doi.org/10.1016/j.icarus.2011.03.030>
- Martínez, G. M., Newman, C. N., De Vicente-Retortillo, A., Fischer, E., Renno, N. O., Richardson, M. I., ... Vasavada, A. R. (2017). The Modern Near-Surface Martian Climate: A Review of In-situ Meteorological Data from Viking to Curiosity. *Space Science Reviews*, 212(1–2), 295–338. <https://doi.org/10.1007/s11214-017-0360-x>
- Massé, M., Conway, S. J., Gargani, J., Patel, M. R., Pasquon, K., McEwen, A., ... Jouannic, G. (2016). Transport processes induced by metastable boiling water under Martian surface conditions. *Nature Geoscience*, 9(6), 425–428. <https://doi.org/10.1038/ngeo2706>
- McCleese, D. J., Heavens, N. G., Schofield, J. T., Abdou, W. A., Bandfield, J. L., Calcutt, S. B., ... Zurek, R. W. (2010). Structure and dynamics of the Martian lower and middle atmosphere as observed by the Mars Climate Sounder: Seasonal variations in zonal mean temperature, dust, and water ice aerosols. *Journal of Geophysical Research E: Planets*, 115(12), 1–16. <https://doi.org/10.1029/2010JE003677>
- McCleese, Daniel J., Schofield, J. T., Taylor, F. W., Calcutt, S. B., Foote, M. C., Kass, D. M., ... Zurek, R. W. (2007). Mars Climate Sounder: An investigation of thermal and water vapor structure, dust and condensate distributions in the atmosphere, and energy balance of the polar regions. *Journal of Geophysical Research E: Planets*, 112(5), 1–16. <https://doi.org/10.1029/2006JE002790>
- McConnochie, T. H., Smith, M. D., Wolff, M. J., Bender, S., Lemmon, M., Wiens, R. C., ... Bell, J. F. (2018). Retrieval of water vapor column abundance and aerosol properties from ChemCam passive sky spectroscopy. *Icarus*, 307, 294–326. <https://doi.org/10.1016/j.icarus.2017.10.043>
- McEwen, A. S. (2018). Are Recurring Slope Lineae Habitable? In *From Habitability to Life on Mars*. <https://doi.org/10.1016/b978-0-12-809935-3.00008-6>
- McEwen, A. S., Dundas, C. M., Mattson, S. S., Toigo, A. D., Ojha, L., Wray, J. J., ... Thomas, N. (2014). Recurring slope lineae in equatorial regions of Mars. *Nature Geoscience*, 7(1), 53–58. <https://doi.org/10.1038/ngeo2014>
- McEwen, A. S., Eliason, E. M., Bergstrom, J. W., Bridges, N. T., Hansen, C. J., Delamere, W. A., ... Weitz, C. M. (2007). Mars Reconnaissance Orbiter's High Resolution Imaging Science Experiment (HiRISE). *Journal of Geophysical Research*, 112(E5), E05S02. <https://doi.org/10.1029/2005JE002605>
- McEwen, A. S., Ojha, L., Dundas, C. M., Mattson, S. S., Byrne, S., Wray, J. J., ... Gulick, V. C.

- (2011). Seasonal flows on warm Martian slopes. *Science*, 333(6043), 740–743. <https://doi.org/10.1126/science.1204816>
- Melchiorri, R., Encrenaz, T., Fouchet, T., Drossart, P., Lellouch, E., Gondet, B., ... Ignatiev, N. (2007). Water vapor mapping on Mars using OMEGA/Mars Express. *Planetary and Space Science*, 55(3), 333–342. <https://doi.org/10.1016/j.pss.2006.05.040>
- Mellor, G. L., & Yamada, T. (1982). OUi OUj. *Reviews of Geophysics*, 20(4), 851–875. <https://doi.org/10.1029/RG020i004p00851>
- Michaels, T. I. (2006). Numerical modeling of Mars dust devils: Albedo track generation. *Geophysical Research Letters*, 33(19), 6–9. <https://doi.org/10.1029/2006gl026268>
- Michaels, T. I., & Rafkin, S. C. R. (2009). Meteorological predictions for candidate 2007 Phoenix Mars Lander sites using the Mars Regional Atmospheric Modeling System (MRAMS). *Journal of Geophysical Research E: Planets*, 114(3), 1–11. <https://doi.org/10.1029/2007JE003013>
- Michelangelo, D. V., Toon, O. B., Haberle, R. M., & Pollack, J. B. (1993). Numerical Simulations of the Formation and Evolution of Water Ice Clouds in the Martian Atmosphere. *Icarus*, Vol. 102, pp. 261–285. <https://doi.org/10.1006/icar.1993.1048>
- Ming, D. W., Archer, P. D., Glavin, D. P., Eigenbrode, J. L., Franz, H. B., Sutter, B., ... Yingst, R. A. (2014). Volatile and organic compositions of sedimentary rocks in Yellowknife Bay, Gale Crater, Mars. *Science*, 343(6169), 1–10. <https://doi.org/10.1126/science.1245267>
- Mitchell, J. L., & Christensen, P. R. (2016). Recurring slope lineae and chlorides on the surface of Mars. *Geophys. Res. Planets*, 121, 1411–1428. <https://doi.org/10.1038/175238c0>
- Möhlmann, D. T. F., Niemand, M., Formisano, V., Savijärvi, H., & Wolkenberg, P. (2009). Fog phenomena on Mars. *Planetary and Space Science*, 57(14–15), 1987–1992. <https://doi.org/10.1016/j.pss.2009.08.003>
- Montmessin, F., Forget, F., Rannou, P., Cabane, M., & Haberle, R. M. (2004). Origin and role of water ice clouds in the Martian water cycle as inferred from a general circulation model. *Journal of Geophysical Research E: Planets*, 109(10), 1–26. <https://doi.org/10.1029/2004JE002284>
- Montmessin, F., Korablev, O., Lefèvre, F., Bertaux, J. L., Fedorova, A., Trokhimovskiy, A., ... Chapron, N. (2017). SPICAM on Mars Express: A 10 year in-depth survey of the Martian atmosphere. *Icarus*, 297, 195–216. <https://doi.org/10.1016/j.icarus.2017.06.022>
- Montmessin, F., Smith, M. D., Langevin, Y., Mellon, M. T., & Fedorova, A. (2017). The Water Cycle. In *The Atmosphere and Climate of Mars* (pp. 338–373). Cambridge University Press.
- Montmessin, Franck, Rannou, P., & Cabane, M. (2002). New insights into Martian dust distribution and water-ice cloud microphysics. *Journal of Geophysical Research E: Planets*, 107(6), 4–1. <https://doi.org/10.1029/2001je001520>
- Moores, J. E., Komguem, L., Whiteway, J. A., Lemmon, M. T., Dickinson, C., & Daerden, F. (2011). Observations of near-surface fog at the Phoenix Mars landing site. *Geophysical Research Letters*, 38(4), 1–6. <https://doi.org/10.1029/2010GL046315>

- Mouginot, J., Pommerol, A., Kofman, W., Beck, P., Schmitt, B., Herique, A., ... Plaut, J. J. (2010). The 3-5MHz global reflectivity map of Mars by MARSIS/Mars Express: Implications for the current inventory of subsurface H<sub>2</sub>O. *Icarus*, *210*(2), 612–625. <https://doi.org/10.1016/j.icarus.2010.07.003>
- Murphy, J. R., Pollack, J. B., Haberle, R. M., Leovy, C. B., Toon, O. B., & Schaeffer, J. (1995). Three-dimensional numerical simulation of Martian global dust storms. *Journal of Geophysical Research*, *100*(E12). <https://doi.org/10.1029/95je02984>
- Navarro-González, R., Vargas, E., De La Rosa, J., Raga, A. C., & McKay, C. P. (2010). Reanalysis of the Viking results suggests perchlorate and organics at midlatitudes on Mars. *Journal of Geophysical Research E: Planets*, *115*(12), 1–11. <https://doi.org/10.1029/2010JE003599>
- Navarro, T., Madeleine, J. B., Forget, F., Spiga, A., Millour, E., Montmessin, F., & Määttänen, A. (2014). Global climate modeling of the Martian water cycle with improved microphysics and radiatively active water ice clouds. *Journal of Geophysical Research: Planets*, *119*(7), 1479–1495. <https://doi.org/10.1002/2013JE004550>
- Nelli, S. M., Murphy, J. R., Feldman, W. C., & Schaeffer, J. R. (2009). Characterization of the nighttime low-latitude water ice deposits in the NASA Ames Mars General Circulation Model 2.1 under present-day atmospheric conditions. *Journal of Geophysical Research E: Planets*, *114*(11), 1–12. <https://doi.org/10.1029/2008JE003289>
- Nelli, S. M., Renno, N. O., Murphy, J. R., Feldman, W. C., & Bougher, S. W. (2010). Simulations of atmospheric phenomena at the Phoenix landing site with the Ames General Circulation Model. *Journal of Geophysical Research E: Planets*, *115*(6), 1–13. <https://doi.org/10.1029/2010JE003568>
- Neumann, G. A., Smith, D. E., & Zuber, M. T. (2003). Two Mars years of clouds detected by the Mars Orbiter Laser Altimeter. *Journal of Geophysical Research E: Planets*, *108*(4), 4–1. <https://doi.org/10.1029/2002je001849>
- Nicholls, M. E., & Pielke, S. (2000). Thermally induced compression waves and gravity waves generated by convective storms. *Journal of the Atmospheric Sciences*, *57*(19), 3251–3271. [https://doi.org/10.1175/1520-0469\(2000\)057<3251:TICWAG>2.0.CO;2](https://doi.org/10.1175/1520-0469(2000)057<3251:TICWAG>2.0.CO;2)
- Nicholls, M. V. E., & Pielke, R. A. (1994). Thermal compression waves. II: Mass adjustment and vertical transfer of total energy. *Quarterly Journal of the Royal Meteorological Society*, *120*(516), 333–359. <https://doi.org/10.1002/qj.49712051606>
- Nikolakakos, G., & Whiteway, J. A. (2018). Laboratory study of adsorption and deliquescence on the surface of Mars. *Icarus*, *308*, 221–229. <https://doi.org/10.1016/j.icarus.2017.05.006>
- Nuding, D. L., Rivera-Valentin, E. G., Davis, R. D., Gough, R. V., Chevrier, V. F., & Tolbert, M. A. (2014). Deliquescence and efflorescence of calcium perchlorate: An investigation of stable aqueous solutions relevant to Mars. *Icarus*, *243*, 420–428. <https://doi.org/10.1016/j.icarus.2014.08.036>
- Ojha, L., McEwen, A., Dundas, C., Byrne, S., Mattson, S., Wray, J., ... Schaefer, E. (2014). HiRISE observations of Recurring Slope Lineae (RSL) during southern summer on Mars. *Icarus*, *231*, 365–376. <https://doi.org/10.1016/j.icarus.2013.12.021>
- Ojha, L., Wilhelm, M. B., Murchie, S. L., McEwen, A. S., Wray, J. J., Hanley, J., ... Chojnacki, M.

- (2015). Spectral evidence for hydrated salts in recurring slope lineae on Mars. *Nature Geoscience*, 8(11), 829–832. <https://doi.org/10.1038/ngeo2546>
- Paige, D. A., Herkenhoff, K. E., & Murray, B. C. (1990). Mariner 9 observations of the South polar cap of Mars: evidence for residual CO<sub>2</sub> frost. *Journal of Geophysical Research*, 95(B2), 1319–1335. <https://doi.org/10.1029/JB095iB02p01319>
- Pankine, A. A., & Tamppari, L. K. (2015). Constraints on water vapor vertical distribution at the Phoenix landing site during summer from MGS TES day and night observations. *Icarus*, 252, 107–120. <https://doi.org/10.1016/j.icarus.2015.01.008>
- Pankine, A. A., Tamppari, L. K., & Smith, M. D. (2010). MGS TES observations of the water vapor above the seasonal and perennial ice caps during northern spring and summer. *Icarus*, 210(1), 58–71. <https://doi.org/10.1016/j.icarus.2010.06.043>
- Pathak, J., Michelangeli, D. V., Komguem, L., Whiteway, J., & Tamppari, L. K. (2009). Simulating Martian boundary layer water ice clouds and the lidar measurements for the Phoenix mission. *Journal of Geophysical Research E: Planets*, 114(3), 1–20. <https://doi.org/10.1029/2007JE002967>
- Pestova, O. N., Myund, L. A., Khripun, M. K., & Prigaro, A. V. (2005). Polythermal study of the systems M(ClO<sub>4</sub>)<sub>2</sub>-H<sub>2</sub>O (M<sup>2+</sup> = Mg<sup>2+</sup>, Ca<sup>2+</sup>, Sr<sup>2+</sup>, Ba<sup>2+</sup>). *Russian Journal of Applied Chemistry*, 78(3), 409–413. <https://doi.org/10.1007/s11167-005-0306-z>
- Pielke, R. A., Cotton, W. R., Walko, R. L., Tremback, C. J., Lyons, W. A., Grasso, L. D., ... Copeland, J. H. (1992). A Comprehensive Meteorological Modeling System RAMS. *Meteorology and Atmospheric Physics*, 49, 69–91.
- Pla-Garcia, J., Rafkin, S. C. R., Kahre, M., Gomez-Elvira, J., Hamilton, V. E., Navarro, S., ... R. Vasavada, A. (2016). The meteorology of Gale crater as determined from rover environmental monitoring station observations and numerical modeling. Part I: Comparison of model simulations with observations. *Icarus*, 280, 103–113. <https://doi.org/10.1016/j.icarus.2016.03.013>
- Pommerol, A., Thomas, N., Jost, B., Beck, P., Okubo, C., & McEwen, A. S. (2013). Photometric properties of Mars soils analogs. *Journal of Geophysical Research E: Planets*, 118(10), 2045–2072. <https://doi.org/10.1002/jgre.20158>
- Primm, K. M., Gough, R. V., Chevrier, V. F., & Tolbert, M. A. (2017). Freezing of perchlorate and chloride brines under Mars-relevant conditions. *Geochimica et Cosmochimica Acta*, 212, 211–220. <https://doi.org/10.1016/j.gca.2017.06.012>
- Primm, K. M., Gough, R. V., Wong, J., Rivera-Valentin, E. G., Martinez, G. M., Hogancamp, J. V., ... Tolbert, M. A. (2018). The Effect of Mars-Relevant Soil Analogs on the Water Uptake of Magnesium Perchlorate and Implications for the Near-Surface of Mars. *Journal of Geophysical Research: Planets*, 123(8), 2076–2088. <https://doi.org/10.1029/2018JE005540>
- Putzig, N. E., & Mellon, M. T. (2007). Apparent thermal inertia and the surface heterogeneity of Mars. *Icarus*, 191(1), 68–94. <https://doi.org/10.1016/j.icarus.2007.05.013>
- Raack, J., Conway, S. J., Herny, C., Balme, M. R., Carpy, S., & Patel, M. R. (2017). Water induced sediment levitation enhances downslope transport on Mars. *Nature Communications*, 8(1). <https://doi.org/10.1038/s41467-017-01213-z>
- Rafkin, S., & Michaels, T. (2019). The Mars Regional Atmospheric Modeling System

- (MRAMS): Current Status and Future Directions. *Atmosphere*, 1–19.  
<https://doi.org/10.3390/atmos10120747>
- Rafkin, S.C.R., & Michaels, T. I. (2003). Meteorological predictions for 2003 Mars Exploration Rover high-priority landing sites. *Journal of Geophysical Research E: Planets*, 108(12), 1–23. <https://doi.org/10.1029/2002je002027>
- Rafkin, S C R, & Rothchild, A. (2011). Surface Meteorology at the Proposed MSL Landing Sites. *The Fourth International Workshop on the Mars Atmosphere: Modelling and Observation*, 279–281. Paris.
- Rafkin, Scot C.R., Haberle, R. M., & Michaels, T. I. (2001). The Mars Regional Atmospheric Modeling System: Model Description and Selected Simulations. *Icarus*, 151(2), 228–256. <https://doi.org/10.1006/icar.2001.6605>
- Rafkin, Scot C.R., Magdalena, M. R. V., & Michaels, T. I. (2002). Simulation of the atmospheric thermal circulation of a martian volcano using a mesoscale numerical model. *Nature*, 419(6908), 697–699. <https://doi.org/10.1038/nature01114>
- Rafkin, Scot C.R., Pla-Garcia, J., Kahre, M., Gomez-Elvira, J., Hamilton, V. E., Marín, M., ... Vasavada, A. (2016). The meteorology of Gale Crater as determined from Rover Environmental Monitoring Station observations and numerical modeling. Part II: Interpretation. *Icarus*, 280, 114–138. <https://doi.org/10.1016/j.icarus.2016.01.031>
- Rafkin, Scot C.Randell, Michaels, T. I., & Haberle, R. M. (2004). Meteorological predictions for the Beagle 2 mission to Mars. *Geophysical Research Letters*, 31(1), 2–6.  
<https://doi.org/10.1029/2003GL018966>
- Rafkin, Scot C Randell, Rothchild, A., Michaels, T. I., & Pielke, R. A. (2011). *Wind-Enhanced Interaction of Radiation and Dust (WEIRD) and the Growth and Maintenance of Local Dust Storms on Mars*.
- Read, P. L., & Lewis, S. R. (2004). *The Martian Climate Revisited - Atmosphere and Environment of a Desert Planet*. Springer.
- Richardson, M. I., & Wilson, R. J. (2002). A topographically forced asymmetry in the martian circulation and climate. *Nature*, 416(6878), 298–301.  
<https://doi.org/10.1038/416298a>
- Richardson, M. I., Wilson, R. J., & Rodin, A. V. (2002). Water ice clouds in the Martian atmosphere: General circulation model experiments with a simple cloud scheme. *Journal of Geophysical Research E: Planets*, 107(9), 2–1.  
<https://doi.org/10.1029/2001je001804>
- Rivera-Valentín, E. G., Gough, R. V., Chevrier, V. F., Primm, K. M., Martínez, G. M., & Tolbert, M. (2018). Constraining the Potential Liquid Water Environment at Gale Crater, Mars. *Journal of Geophysical Research: Planets*, 123(5), 1156–1167.  
<https://doi.org/10.1002/2018JE005558>
- Rodin, A. V., Korablev, O. I., & Moroz, V. I. (1997). Vertical distribution of water in the near-equatorial troposphere of Mars: Water vapor and clouds. *Icarus*, 125(1), 212–229.  
<https://doi.org/10.1006/icar.1996.5602>
- Savijärvi, H. (1995). Mars boundary layer modeling: Diurnal moisture cycle and soil properties at the Viking Lander 1 site. *Icarus*, Vol. 117, pp. 120–127.  
<https://doi.org/10.1006/icar.1995.1146>

- Savijärvi, H., Harri, A. M., & Kemppinen, O. (2016). The diurnal water cycle at Curiosity: Role of exchange with the regolith. *Icarus*, 265, 63–69. <https://doi.org/10.1016/j.icarus.2015.10.008>
- Schaefer, E. I., McEwen, A. S., & Sutton, S. S. (2019). A case study of recurring slope lineae (RSL) at Tivat crater: Implications for RSL origins. *Icarus*, 317(July 2018), 621–648. <https://doi.org/10.1016/j.icarus.2018.07.014>
- Schmidt, F., Andrieu, F., Costard, F., Kocifaj, M., & Meresescu, A. G. (2017). Formation of recurring slope lineae on Mars by rarefied gas-triggered granular flows. *Nature Geoscience*, 10(4), 270–273. <https://doi.org/10.1038/ngeo2917>
- Schorghofer, N., Levy, J. S., & Goudge, T. A. (2019). High-Resolution Thermal Environment of Recurring Slope Lineae in Palikir Crater, Mars, and Its Implications for Volatiles. *Journal of Geophysical Research: Planets*, 2852–2862. <https://doi.org/10.1029/2019JE006083>
- Seu, R., Phillips, R. J., Biccari, D., Orosei, R., Masdea, A., Picardi, G., ... Nunes, D. C. (2007). SHARAD sounding radar on the Mars Reconnaissance Orbiter. *Journal of Geophysical Research E: Planets*, 112(5), 1–18. <https://doi.org/10.1029/2006JE002745>
- Smagorinsky, J. (1963). General Circulation Experiments With the Primitive Equations. *Monthly Weather Review*, 91(3), 99–164. [https://doi.org/10.1175/1520-0493\(1963\)091<0099:gcewtp>2.3.co;2](https://doi.org/10.1175/1520-0493(1963)091<0099:gcewtp>2.3.co;2)
- Smith, D. E., Zuber, M. T., Solomon, S. C., Phillips, R. J., Head, J. W., Garvin, J. B., ... Duxbury, T. C. (1999). The global topography of Mars and implications for surface evolution. *Science*, 284(5419), 1495–1503. <https://doi.org/10.1126/science.284.5419.1495>
- Smith, M. D. (2002). The annual cycle of water vapor on Mars as observed by the Thermal Emission Spectrometer. *Journal of Geophysical Research E: Planets*, 107(11), 25–1. <https://doi.org/10.1029/2001je001522>
- Smith, M. D. (2004). Interannual variability in TES atmospheric observations of Mars during 1999-2003. *Icarus*, 167(1), 148–165. <https://doi.org/10.1016/j.icarus.2003.09.010>
- Smith, M. D. (2009). THEMIS observations of Mars aerosol optical depth from 2002-2008. *Icarus*, 202(2), 444–452. <https://doi.org/10.1016/j.icarus.2009.03.027>
- Smith, M. D., Wolff, M. J., Clancy, R. T., & Murchie, S. L. (2009). Compact Reconnaissance Imaging Spectrometer observations of water vapor and carbon monoxide. *Journal of Geophysical Research*, 114(June), 1–13. <https://doi.org/10.1029/2008je003288>
- Smith, P. H., Tamppari, L. K., Arvidson, R. E., Bass, D., Blaney, D., Boynton, W. V., ... Zent, A. P. (2009). H<sub>2</sub>O at the phoenix landing site. *Science*, 325(5936), 58–61. <https://doi.org/10.1126/science.1172339>
- Spinrad, H., & Richardson, E. H. (1963). High dispersion spectra of the outer planets. II. A new upper limit for the water vapor content of the Martian atmosphere. *Icarus*, 2(C), 49–53. [https://doi.org/10.1016/0019-1035\(63\)90007-1](https://doi.org/10.1016/0019-1035(63)90007-1)
- Stillman, D. E. (2017). Unraveling the mysteries of Recurring Slope Lineae (RSL). In *Dynamic Mars*.
- Stillman, D. E., Bue, B. D., Wagstaff, K. L., Primm, K. M., Michaels, T. I., & Grimm, R. E. (2020). Evaluation of wet and dry Recurring Slope Lineae (RSL) formation mechanisms based

- on quantitative mapping of RSL in Garni Crater, Valles Marineris, Mars. *Icarus*, 335(May 2019), 113420. <https://doi.org/10.1016/j.icarus.2019.113420>
- Stillman, D. E., & Grimm, R. E. (2018). Two pulses of seasonal activity in martian southern mid-latitude recurring slope lineae (RSL). *Icarus*, 302, 126–133. <https://doi.org/10.1016/j.icarus.2017.10.026>
- Stillman, D. E., Michaels, T. I., & Grimm, R. E. (2017). Characteristics of the numerous and widespread recurring slope lineae (RSL) in Valles Marineris, Mars. *Icarus*. <https://doi.org/10.1016/j.icarus.2016.10.025>
- Stillman, D. E., Michaels, T. I., Grimm, R. E., & Hanley, J. (2016). Observations and modeling of northern mid-latitude recurring slope lineae (RSL) suggest recharge by a present-day martian briny aquifer. *Icarus*, 265, 125–138. <https://doi.org/10.1016/j.icarus.2015.10.007>
- Stillman, D. E., Michaels, T. I., Grimm, R. E., & Harrison, K. P. (2014). New observations of martian southern mid-latitude recurring slope lineae (RSL) imply formation by freshwater subsurface flows. *Icarus*, 233, 328–341. <https://doi.org/10.1016/j.icarus.2014.01.017>
- Stull, R. B. (1988). *An Introduction to Boundary Layer Meteorology*. Kluwer Academic Publishers,.
- Suarez, M. J., & Takacs, L. L. (1995). *Technical Global Report Series on Modeling of the Dynamical Core : Documentation ARIES / GEOS Version 2* (Vol. 5).
- Tamppari, L. K., Bass, D., Cantor, B., Daubar, I., Dickinson, C., Fisher, D., ... Wolff, M. (2010). Phoenix and MRO coordinated atmospheric measurements. *Journal of Geophysical Research E: Planets*, 115(5), 1–25. <https://doi.org/10.1029/2009JE003415>
- Tillman, J. E., Henry, R. M., & Hess, S. L. (1979). Frontal systems during passage of the Martian north polar hood over the Viking Lander 2 site prior to the first 1977 dust storm. *Journal of Geophysical Research*, 84(B6), 2947. <https://doi.org/10.1029/jb084ib06p02947>
- Titov, D. V., Markiewicz, W. J., Thomas, N., Keller, H. U., Sablotny, R. M., Tomasko, M. G., ... Smith, P. H. (1999). Measurements of the atmospheric water vapor on Mars by the Imager for Mars Pathfinder. *Journal of Geophysical Research E: Planets*, 104(E4), 9019–9026. <https://doi.org/10.1029/1998JE900046>
- Toon, O. B., McKay, C. P., Ackerman, T. P., & Santhanam, K. (1989). Rapid calculation of radiative heating rates and photodissociation rates in inhomogeneous multiple scattering atmospheres. *Journal of Geophysical Research*, 94(D13), 287–301. <https://doi.org/10.1029/jd094id13p16287>
- Toon, O. B., Turco, R. P., Westphal, D., Malone, R., & Liu, M. S. (1988). A multidimensional model for aerosols: description of computational analogs. *Journal of the Atmospheric Sciences*, Vol. 45, pp. 2123–2143. [https://doi.org/10.1175/1520-0469\(1988\)045<2123:ammfad>2.0.co;2](https://doi.org/10.1175/1520-0469(1988)045<2123:ammfad>2.0.co;2)
- Tripoli, G. J., & Cotton, W. R. (1980). A numerical investigation of several factors contributing to the observed variable intensity of deep convection over South Florida. *Journal of Applied Meteorology*, Vol. 19, pp. 1037–1063. [https://doi.org/10.1175/1520-0450\(1980\)019<1037:ANIOSF>2.0.CO;2](https://doi.org/10.1175/1520-0450(1980)019<1037:ANIOSF>2.0.CO;2)



- Tschimmel, M., Ignatiev, N. I., Titov, D. V., Lellouch, E., Fouchet, T., Giuranna, M., & Formisano, V. (2008). Investigation of water vapor on Mars with PFS/SW of Mars Express. *Icarus*, *195*(2), 557–575. <https://doi.org/10.1016/j.icarus.2008.01.018>
- Tyler, D., & Barnes, J. R. (2005). A mesoscale model study of summertime atmospheric circulations in the north polar region of Mars. *Journal of Geophysical Research E: Planets*, *110*(6), 1–26. <https://doi.org/10.1029/2004JE002356>
- Wang, A., Ling, Z., Yan, Y., McEwen, A. S., Mellon, M. T., Smith, M. D., ... Head, J. (2019). Subsurface Cl-bearing salts as potential contributors to recurring slope lineae (RSL) on Mars. *Icarus*, *333*(June), 464–480. <https://doi.org/10.1016/j.icarus.2019.06.024>
- Wang, H., & Ingersoll, A. P. (2002). Martian clouds observed by Mars Global Surveyor Mars Orbiter Camera. *Journal of Geophysical Research E: Planets*, *107*(10), 8–1. <https://doi.org/10.1029/2001je001815>
- Wang, H., & Richardson, M. I. (2015). The origin, evolution, and trajectory of large dust storms on Mars during Mars years 24–30 (1999–2011). *Icarus*, *251*, 112–127. <https://doi.org/10.1016/j.icarus.2013.10.033>
- Watkins, J., Ojha, L., Chojnacki, M., Reith, R., Angeles, L., Sciences, S., & Angeles, L. (2014). Structurally Controlled Subsurface Fluid Flow as a Mechanism for the Formation of Recurring Slope Lineae. *45th Lunar and Planetary Science Conference*, 3–4.
- Whiteway, J. A., Komguem, L., Dickinson, C., Cook, C., Illnicki, M., Seabrook, J., ... Smith, P. H. (2009). Mars water-ice clouds and precipitation. *Science*, *325*(5936), 68–70. <https://doi.org/10.1126/science.1172344>
- Wilson, R. J., Neumann, G. A., & Smith, M. D. (2007). Diurnal variation and radiative influence of Martian water ice clouds. *Geophysical Research Letters*, *34*(2), 2–5. <https://doi.org/10.1029/2006GL027976>
- Wolff, M. J., Smith, M. D., Clancy, R. T., Spanovich, N., Whitney, B. A., Lemmon, M. T., ... Squyres, S. W. (2006). Constraints on dust aerosols from the Mars Exploration Rovers using MGS overflights and Mini-TES. *Journal of Geophysical Research E: Planets*, *111*(12), 1–23. <https://doi.org/10.1029/2006JE002786>
- Ye, Z. J., Segal, M., & Pielke, R. A. (1990). A Comparative Study. *Journal of the Atmospheric Sciences*, *47*(5), 612–628.
- Zent, A. P., Haberle, R. M., Houben, H. C., & Jakosky, B. M. (1993). A coupled subsurface-boundary layer model of water on Mars. *Journal of Geophysical Research*, *98*(E2), 3319–3337. <https://doi.org/10.1029/92JE02805>
- Zorzano, M. P., Mateo-Martí, E., Prieto-Ballesteros, O., Osuna, S., & Renno, N. (2009). Stability of liquid saline water on present day Mars. *Geophysical Research Letters*, *36*(20), 2–5. <https://doi.org/10.1029/2009GL040315>
- Zurek, R. W., Barnes, J. R., Haberle, R. M., Pollack, J. B., Tillman, J. E., & Leovy, C. B. (1992). Dynamics of the Atmosphere of Mars. In *Mars* (pp. 835–933). Tucson: Univ. of Ariz. Press.